Photophysics and OLED properties of novel blue MR-TADF molecules

ウィーラシンヘ ランガニー ワスサラー

2024

Doctoral Dissertation

Photophysical and OLED properties of novel blue MR-TADF molecules

Rangani Wathsala Weerasinghe

Department of Applied Chemistry
Graduate School of Engineering
Kyushu University

2024.07.02

Table of Contents

Chapter 3: A boron, nitrogen, and oxygen incorporated π-extended helical pure blue MR-TADF emitter having fast k_{RISC}

Chapter 4: Summary and future prospective

Chapter 1

General Introduction

1.1. Spin statistics

After a molecule in the electronically ground state (S_0) is excited, the kind of excited state formed is determined by the total spin quantum number, S ($S = \sum s_i$, where $s_i = +1/2$ or $-1/2$), which in turn determines the spin multiplicity that defined as the number of possible orientations of the spin angular momentum relative to a given S.[1,2]

$$S = \sum s_i$$

$$Spin\ multiplicity = 2S + 1$$

where s_i is the spin quantum number with two possible values, +1/2 or −1/2.

If the spin of the electron remaining at the highest occupied molecular orbital (HOMO) is anti-parallel to the spin of the electron excited to the lowest unoccupied molecular orbital (LUMO), a singlet excited state with a spin multiplicity of one is formed (**Figure 1-1**).[1] When electron spins align parallel, a triplet state with a multiplicity of three is formed (**Figure 1-1**). According to Hund's rule, when two unpaired electrons occupy separate orbitals with parallel spins, they experience minimal energy repulsion, resulting in the triplet excited typically having lower energy than its corresponding singlet.[1] When the emitter is excited optically or electrically, 25% of the resulting excited states will be S_1, while the remaining 75% being T_1.[3,4] According to the spin rules, the transitions between different spin multiplicities are forbidden. [1]

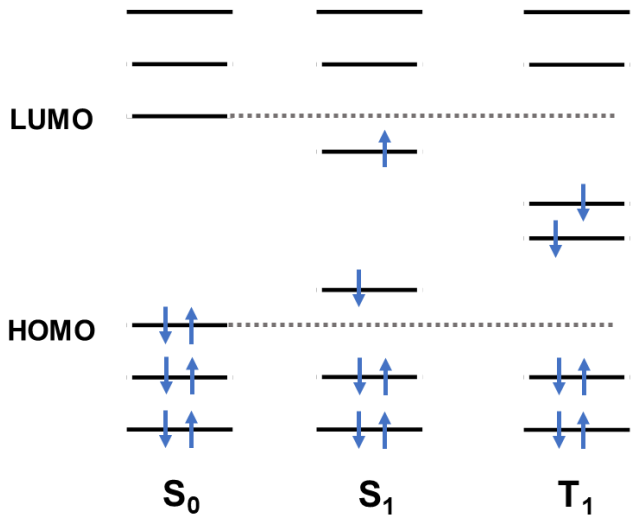

Figure 1-1. Schematic demonstration of singlet and triplet excited-states.

1.2. An introduction to Organic Light Emitting Diodes (OLEDs)

With the introduction of the first practical OLED in 1987, OLEDs have had a significant impact on various industries, particularly in display industry due to their unique properties like mechanically flexibility, eco-friendliness, high efficiency, lightweight, and low cost.[5]

1.2.1. OLED structure and operation principle

Generally, OLEDs are thin multilayer devices comprised of organic semiconductor layers. The first OLED was a simplest structure with an emitting layer and a hole-transporting layer sandwiched between an anode and a cathode (**Figure 1-2a**).[5] From this simple structure, the structure of OLEDs has grown more complex over the past few decades to achieve improved optical and electrical performances through the adoption of sophisticated device architectures (**Figure 1-2b**).[6–8] Apart from the light emitting layer, the anode and the cathode, a typical structure of a modern OLED device consists of the following components: a hole injection layer (HIL), and an electron injection layer (EIL) to support the charge injection by lowering the energy barriers for the hole and electron injection respectively, a hole transport layer (HTL) and an electron transport layer (ETL) for the effective charge injection and charge carrier transport towards the EML, by gradually lowering the energy barriers. Further, a hole-blocking layer (HBL) and an electron-blocking layer (EBL) help to recombine the electrons and holes within the EML by inhibiting them from migrating to the neighboring carrier transport layers.[7,8]

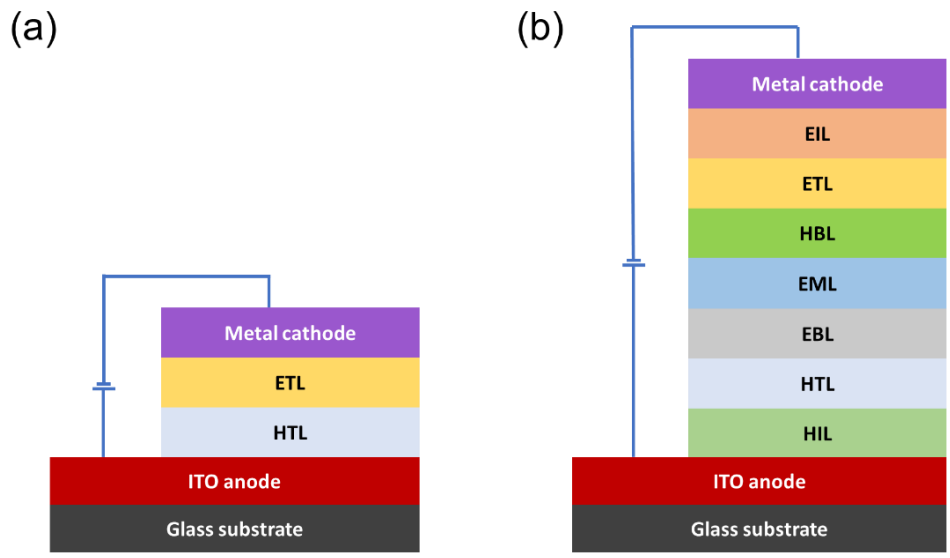

Figure 1-2. Structures of typical multilayer OLED. (a) two-layer and (b) multi-layer structures.

A schematic of the basic operation mechanism of an OLED is illustrated in **Figure 1-3**. Under an applied voltage, charge-carrying layers allow holes and electrons to be injected from the anode and cathode into the emissive layer. In the emissive layer, holes and electrons recombine to form excitons.[7,8] Light emission occurs as a result of the radiative decay of these excitons as they relax back to the ground state. The efficiency of an OLED depends on several factors, which will be discussed later in **Section 1.6**.

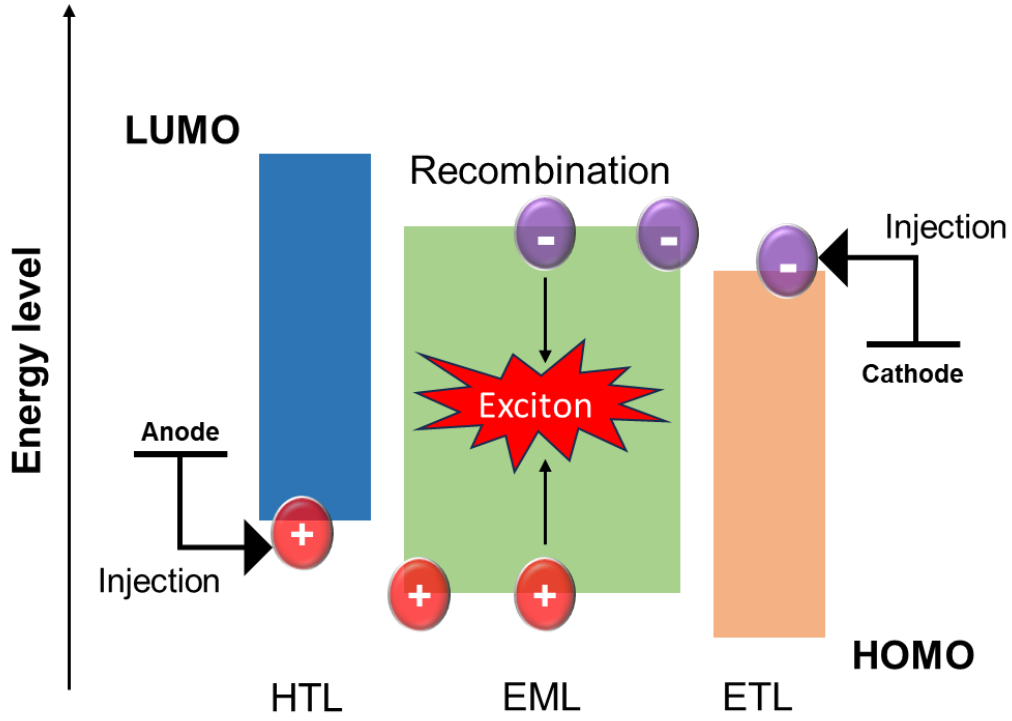

Figure 2-3. A schematic of the basic operation mechanism of an OLED.

1.2.2. Progression of OLEDs

The progression of OLED technology has been categorized into several generations, each defined by the specific emission mechanism employed to produce light by the emitter. The first-generation (1st Gen.) of OLEDs is referred to as fluorescence OLEDs (FOLEDs), followed by phosphorescence OLEDs (POLEDs) in the second-generation (2nd Gen.) and TADF OLEDs in the third-generation (3rd Gen.).

As mentioned in **Section 1.1**, the ratio between electrically generated S_1 and T_1 excitons is 1:3. In FOLEDs, which utilize fluorescence emitters, only singlet excitons can be harvested, while triplet excitons are typically non-emissive as the transitions between different spin multiplicities are forbidden.[9] Therefore, the internal quantum efficiency (η_{int}) of FOLEDs are limited to 25%.[5,9] To utilize both singlets and triplets, 2nd Gen. POLEDs are equipped with

heavy metal complexes such as platinum and iridium.[10,11] These heavy metals induce strong spin-orbit coupling (SOC) between S_1 and T_1, thereby boosting the intersystem crossing (ISC) from S_1 to T_1 and enhancing radiative phosphorescence from T_1.[12,13] Therefore, POLEDs utilizing heavy metals can reach up to 100% η_{int} through phosphorescence emission.[13] Although POLEDs are promising in the commercial OLED industry, their major drawbacks, such as high cost and environmental toxicity due to the use of rare heavy metals, limit their applications.[14–16] Consequently, research has focused on developing alternative strategies to achieve 100% η_{int} without relying on POLEDs. In this context, thermally activated delayed fluorescence (TADF) emitters have been introduced as 3rd Gen. OLED emitters, offering a viable approach for triplet harvesting without the use of heavy atoms. Triplet harvesting in TADF emitters is achieved through reverse intersystem crossing, facilitated by thermal energy.

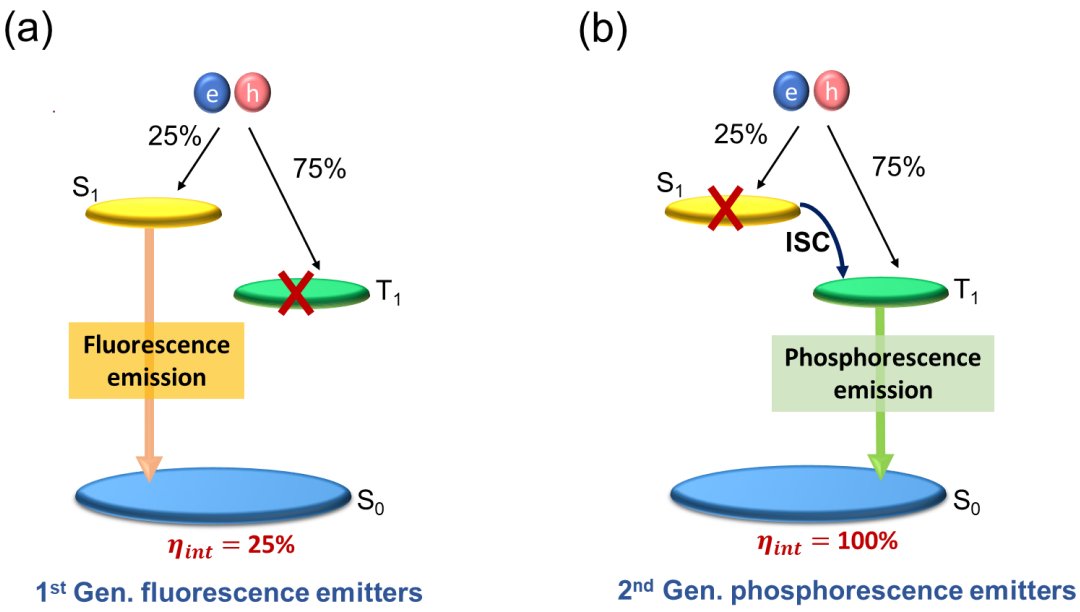

Figure 1-4. Light emission mechanism of (a) 1st Gen. fluorescence and (b) 2nd Gen. phosphorescence emitters.

1.3. Thermally Activated Delayed Fluorescence (TADF)

The concept of TADF was first recognized by F. Perin in 1929.[17] Late in 1941, Magel and his group conducted further studies on delayed fluorescence in fluorescein solutions.[18] Then, the observation of delayed fluorescence in eosin was reported by Parker and Hatchard in 1961.[19] At that stage, this phenomenon was known as e-type delayed fluorescence. In 1968, Wilkinson and Horsocks firstly used the term "thermally activated delayed fluorescence" to

describe this phenomenon.[20] Since the first discovery, several types of delayed fluorescence materials, including eosins and fullerenes, have been studied for several decades.[19,21–23] However, TADF materials were not given much attention at that stage due to their low efficiency and lack of practical applications. In 2009, C. Adachi and his group at Kyushu University firstly applied the TADF mechanism to OLED using the tin porphyrin complex, **SnF_2-OEP**, as a TADF emitter (**Figure 1-5a**).[24] However, this application showed low efficiency and a minimal contribution of TADF to the light emission. In 2011, the same group introduced the first OLED based on a purely organic TADF emitter, **PIC-TRZ** with an EQE_{max} of 5.3%, reaching the theoretical EQE_{max} limit of fluorescence emitters (**Figure 1-5b**).[25] A major breakthrough was achieved in 2012 by the same group with the report of a highly efficient OLED using an organic TADF emitter, **4CzIPN**, with an EQE_{max} of 19.3%, surpassing the theoretical maximum limit of fluorescence OLEDs (**Figure 1-5b**).[4] Since then, the 3rd Gen. TADF has emerged as a promising OLED technology due to its ability to achieve 100% of electrically generated excitons using purely organic emitters, enabling light emission without the need for rare heavy metals.

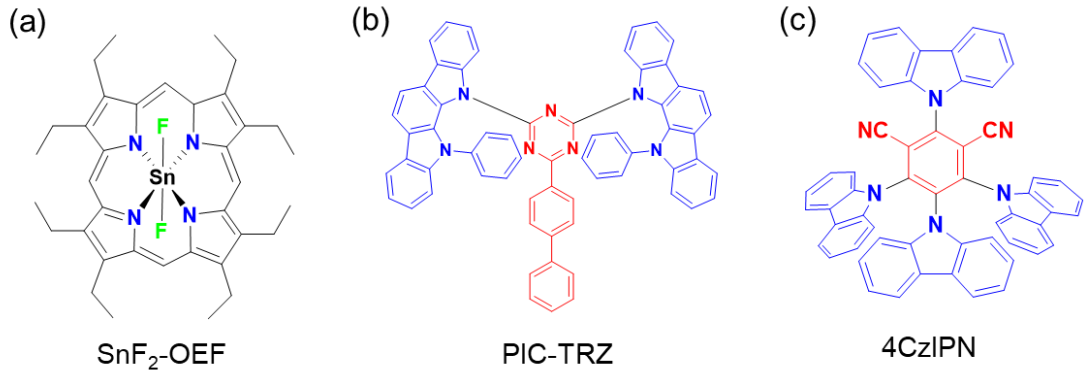

Figure 1-5. Chemical structures of (a) **SnF_2-OEF**, (b) **PIC-TRZ**, and (c) **4CzIPN**.

1.3.1. TADF mechanism

TADF is achieved through spin up-conversion from the triplet excited state to the singlet excited state via reverse intersystem crossing (RISC), which is initiated by thermal energy (**Figure 1-6**).[4,26–28] Consequently, to achieve high-performance TADF-based devices, the emitter must possess high photoluminescence quantum yield (Φ_{PL}) and fast reverse intersystem crossing rate (k_{RISC}).

The total exciton utilization from prompt and delayed emission via radiative decay from S_1 to the ground state is expressed by Φ_{PL}. The oscillator strength (f) for the radiative decay to the ground state is directly proportional to the overlap between HOMO and LUMO wave

functions. Thus, the overlap between HOMO and LUMO should be sufficient enough to achieve a high Φ_{PL}.[29]

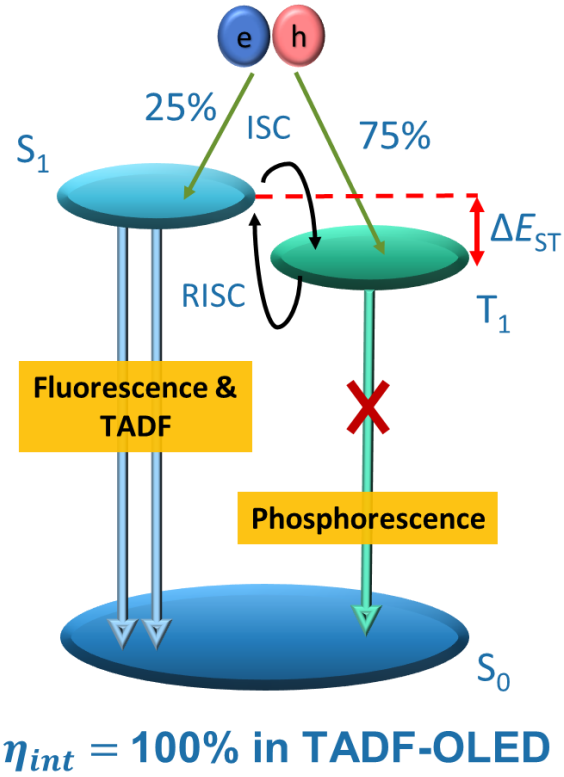

Figure 3-6. Schematic of light-emitting mechanism of 3rd Gen. TADF.

According to **Eq. 1**, k_{RISC} is strongly dependent on the singlet-triplet energy gap (ΔE_{ST}) and substantial SOC between singlet and triplet excited states.[30]

$$k_{RISC} \propto |\langle \psi_s | \hat{H}_{SOC} | \psi_T \rangle|^2 \exp\left(\frac{-\Delta E_{ST}}{k_B T}\right) \qquad \textbf{Eq. 1}$$

where k_B is the Boltzmann constant and T is the temperature.

1.3.1.1. Spin-orbit coupling

For TADF to occur, the excitons from a triplet state should be efficiently upconverted into the singlet state. However, as mentioned in **Section 1.1**, transitions between different spin multiplicities are forbidden. Nonetheless, sufficient mixing of spin and orbital angular momentum between T_n and S_n states, i.e., SOC, can allow these spin forbidden transitions, facilitating ISC and RISC processes.[30,31] According to the **Eq. 1**, it is clear that even a small increment in the SOC can highly affect the k_{RISC} in two orders of magnitude. A pronounced way to increase SOC is the use of heavy atoms such as platinum, iridium, bromine, and selenium in the emitter design. However, when designing efficient and stable TADF emitters for practical applications, the use of heavy atoms should be avoided. Carbon-heteroatom bonds, such as C-S, C-Se, and C-Br, are relatively weak and thus prone to photochemical decomposition.[32] This is because when the atomic size of the heteroatom increases (a heavy atom is large in size), the bond length becomes longer, reflected in lower bond dissociation energies (BDE).[32] The decrease in BDE results in a weaker bond that will be more easily ruptured. Therefore, emitters with these types of weak bonds always have less chemical stabilities.

1.3.1.2. Energy gap between singlet and triplet states

Generally, the ΔE_{ST} of an emitter should be less than 0.2 eV for efficient TADF to occur. However, some materials exhibit TADF even with a larger energy gap. The ΔE_{ST} relies on exchange interaction integral, J (**Eq. 2, 3, and 4**), which is directly proportional to the excited state and ground state wavefunction overlap, i.e., the overlap between HOMO and LUMO (**Eq. 5**).[31,33]

$$E_{S1} = E_{orb} + K + J \qquad \textbf{Eq. 2}$$

$$E_{T1} = E_{orb} + K - J \qquad \textbf{Eq. 3}$$

$$E_S - E_T = 2J \qquad \textbf{Eq. 4}$$

$$J = \iint \Phi_{(\boldsymbol{r1})}\Psi_{(\boldsymbol{r2})}\left(\frac{e^2}{\boldsymbol{r_1 - r_2}}\right)\Phi_{(\boldsymbol{r2})}\Psi_{(\boldsymbol{r1})}d\boldsymbol{r_1}d\boldsymbol{r_2} \qquad \textbf{Eq. 5}$$

where E_{orb} represents the orbital energy, K is the electron repulsion energy, and Φ and Ψ are the HOMO and LUMO wavefunctions, respectively, and e is the electronic charge.

Hence, the prevailing strategy in designing TADF emitters to achieve a sufficiently small ΔE_{ST} involves minimizing the electron exchange energy by spatially separating the HOMO and LUMO.[30] However, as mentioned, the overlap between HOMO and LUMO should be kept to some extent to achieve sufficient Φ_{PL}.

1.3.2. Conventional TADF emitter

Conventional TADF emitters typically comprise donor (D) and acceptor (A) moieties arranged in a twisted molecular conformation, effectively segregating the HOMO and LUMO (**Figure 1-7a**).[34,35] Within the D-A system, the HOMO is localized on the donor and the LUMO on the acceptor and thereby minimizing the ΔE_{ST}. This structural arrangement facilitates a high k_{RISC}, potentially reaching up to 1×10^{-8} s^{-1}. However, the long-range charge transfer character (LRCT) inherent in such designs induces significant reorganization in molecular geometry between the ground state and excited state, consequently leading to the generation of a broadband emission spectrum and large stokes shift.[36] Broad emission spectra are unfavorable to color purity, which is crucial for high-quality OLEDs. Several examples of D-A type TADF emitters are illustrated in **Figure 1-7b**.[33]

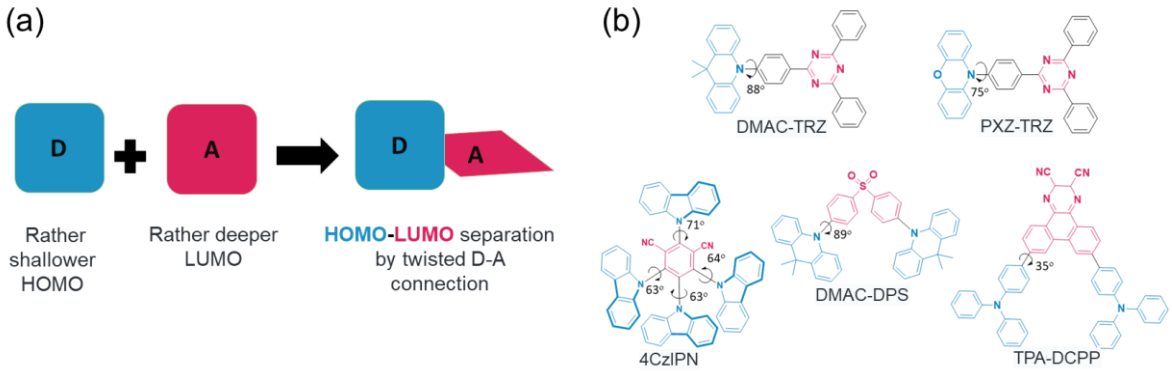

Figure 1-7. (a) Schematic of HOMO-LUMO separation by D-A connection and (b) examples for D-A type TADF emitters.

1.4. Commission Internationale de l'Éclairage (CIE) chromaticity diagram and color standards

For commercial applications, the high color purity of the red, green, and blue OLED emitters is vital. Spectral color at a specific wavelength is determined by the combination of three parameters (tristimulus values), X, Y, and Z. These X, Y, and Z are imaginary color primaries, which account for the weighing of red, green, and blue color, respectively.[37] The spectral color at a specific wavelength, λ, is determined by the CIE color matching functions, $\bar{x}$, $\bar{y}$, and $\bar{z}$, which express the extent of X, Y, and Z required for the produce the spectral color at that specific wavelength.

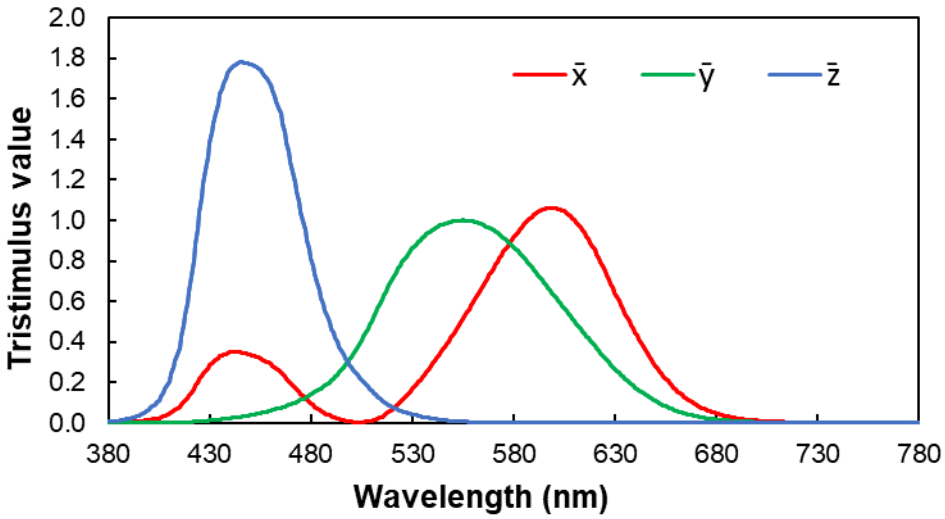

Figure 1-8. Tristimulus curves.

When considering a specific wavelength of an emission spectrum (λ_i), the contribution of X, Y, and Z components to the expression of color at λ_i can be expressed by,

$$X_{\lambda_i} = I_i \times \bar{x}_{\lambda_i} \qquad \textbf{Eq. 6}$$

$$Y_{\lambda_i} = I_i \times \bar{y}_{\lambda_i} \qquad \textbf{Eq. 7}$$

$$Z_{\lambda_i} = I_i \times \bar{z}_{\lambda_i} \qquad \textbf{Eq. 8}$$

where, $\bar{x}_{\lambda_i}$, $\bar{y}_{\lambda_i}$, and $\bar{z}_{\lambda_i}$ are the corresponding tristimulus values at λ_i, and I_i is the intensity of the emission spectrum at λ_i (in arb. unit).

Therefore, CIE X, Y, and Z for a given spectrum can be given as, $X = \sum_i^n X_{\lambda_i}$, $Y = \sum_i^n Y_{\lambda_i}$, and $Z = \sum_i^n Z_{\lambda_i}$, respectively. The CIE chromaticity coordinates, x, y, and z, can be determined by normalizing the X, Y, and Z values as follows,

$$x = \frac{X}{X + Y + Z} \qquad \textbf{Eq. 9}$$

$$y = \frac{Y}{X + Y + Z} \qquad \textbf{Eq. 10}$$

$$z = \frac{Z}{X + Y + Z} \qquad \textbf{Eq. 11}$$

However, since z = 1−x−y, we can express the color in a two-dimensional CIE chromaticity diagram by using CIE coordinates x and y. Therefore, the color gamut of OLED displays is typically an enclosed area determined by the CIE (x, y) coordinates where colors are represented as points on the CIE diagram corresponding to human color vision. (**Figure 1-9**). It illustrates the entire spectrum of colors that is acquired by combining primary colors by modulating the emission intensity and wavelength.[37]

At present, industry color requirements for ultra-high-definition (UHD) displays are becoming more and more stringent. To satisfy the growing demand for UHD displays, the International Telecommunication Union (ITU) released the next-generation color gamut standard in 2012, known as ITU-R Recommendation BT.2020.[38] Compared to the previous color standards, the most recent BT.2020 color gamut became wider with CIE coordinates of (0.708, 0.292), (0.170, 0.797), and (0.131, 0.046) for the red, green, and blue color pixels, respectively.[38] To obtain sharp color contrast and high image quality, the color gamut on the CIE coordinate should be expanded, aiming at BT.2020. The CIE coordinates of emitters are dependent on their emission maximum and the FWHM.[39] Hence, narrowband emission is crucial for satisfying the BT.2020 color standard.

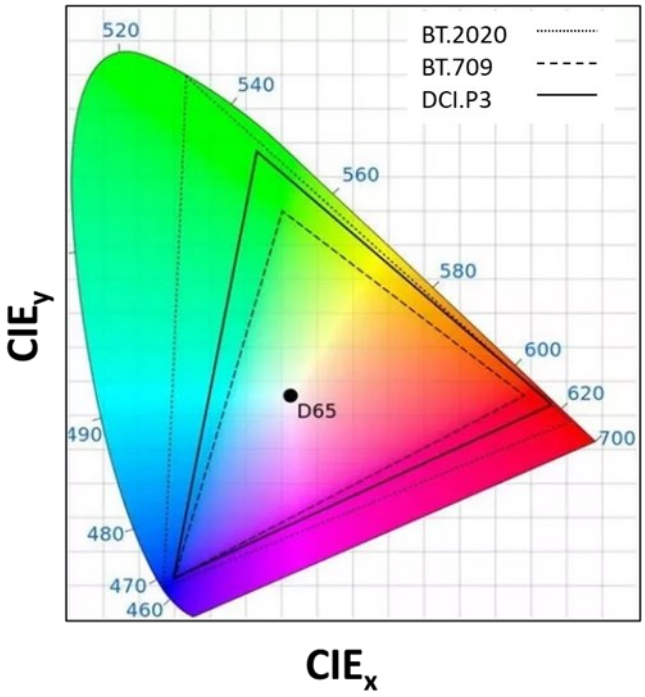

Figure 1-9. CIE 1931 color space chromaticity diagram with boundary requirements for different color standards based on literature.[38,39]

Although the CIE coordinates for the red, green, and blue colors of the BT.2020 standard correspond to wavelengths at 630, 532, and 467 nm, respectively, in the visible spectrum, the broad electroluminescence spectra of conventional TADF emitters result in emission spectra covering a range of wavelengths rather than sharp lines at specific wavelengths affecting the color purity (**Figure 1.10**).[37] For conventional blue emitters, their broad spectra extend into the adjacent green region, impacting the CIE_y value. Therefore, satisfying CIE_y = 0.046 is a significant challenge.

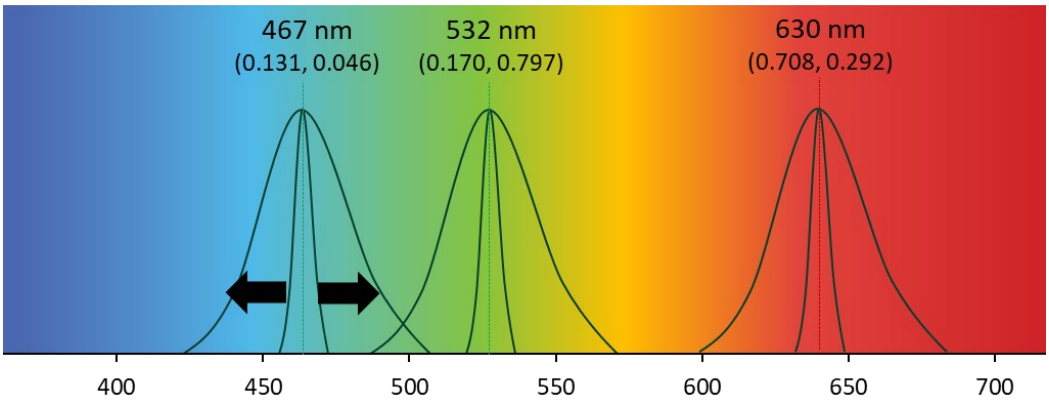

Figure 1-10. Change of color purity due to the broad emission.[39]

1.5. Multiple resonance (MR) TADF emitters

Although commercial OLEDs with conventional TADF emitters commonly use color filters or microcavity effects to satisfy the color standards, these methods cause significant energy loss. As a solution for achieving narrowband emission, in 2016, Prof. Hatakeyama's group introduced MR-TADF emitters, in which the HOMO and LUMO are localized on neighboring atoms in an alternate manner by multiple resonance effect, ensuring a sufficiently small ΔE_{ST} to turn on TADF (**Figure 1-11**).[27] Due to their rigid structure, MR-TADF emitters have minimal geometry reorganization from the ground to the excited state, leading to narrowband emission with small FWHM and small Stoke-shift.

These first reported MR-TADF emitters, **DABNA 1**, and **DABNA 2** demonstrated excellent color purity with an FWHM of only 28 nm.[27] Since then, many research groups have developed MR-TADF emitters with certain modifications in the molecular structure based on different design concepts.[26,40]

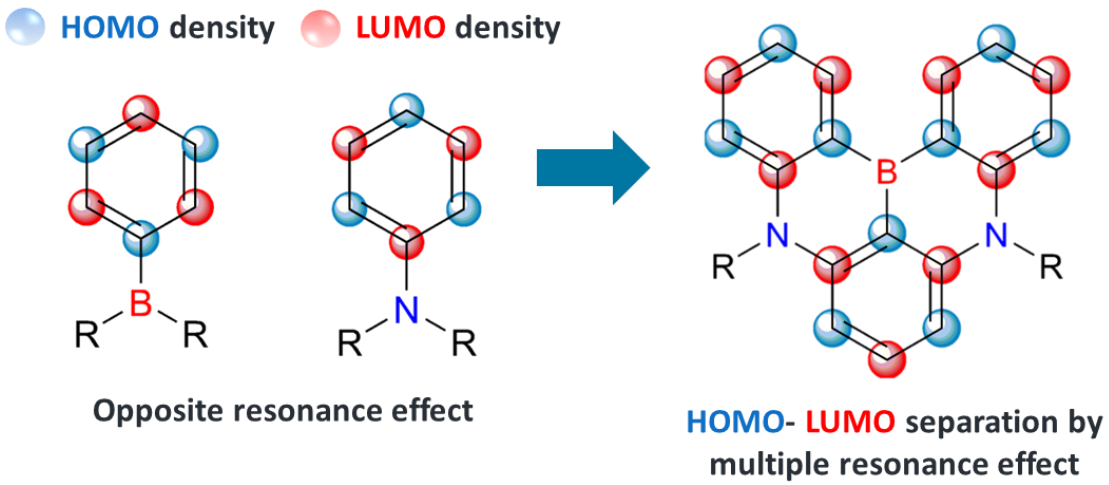

Figure 1-11. Schematic of HOMO-LUMO separation by MR effect.

However, a major drawback associated with MR-TADF emitters is the relatively inefficient up-conversion of triplet excitons into singlet excitons due to their moderately large ΔE_{ST}, and the small degree of SOC. The k_{RISC} of MR-TADF emitters without incorporating heavy atoms typically lies below 10^5 s^{-1}. This low k_{RISC} leads to long delay lifetimes (τ_d), and limits device performances, resulting in low external quantum efficiencies (EQE) and severe efficiency roll-off.[28,41] This study was mainly focused on the novel deep-blue MR-TADF emitters aiming for high efficiency and high color purity.

1.5.1. Deep-blue MR-TADF with high color purity

When considering the blue pixels, OLEDs based on narrowband MR-TADF emitter satisfying BT.2020 of CIE_y = 0.046 have seldom been reported in the literature. Park *et al.* reported deep-blue MR-TADF emitter, **BOBO-Z** (**Figure 1-12a**) which shows an EQE_{max} of 13.6% with deep blue narrowband emission (λ_{EL}= 445 nm, FWHM = 24 nm) with CIEy of 0.04 in resulting devices due to its relatively small ΔE_{ST} of 102 meV and a k_{RISC} of 7.0 × 10^4 s^{-1} in doped film.[42] Chan *et al.* also reported deep-blue MR-TADF emitter, **2B-DTACrs**, which shows EQE_{max} of 14.8% at a wavelength of 447 nm, with CIE coordinates of (0.150, 0.044) (**Figure 1-12b**).[43] This was attributed to its moderate ΔE_{ST} of 160 meV and short τ_d of 13.1 μs in the doped film, leading to a relatively fast k_{RISC} (1.3 × 10^5 s^{-1}).

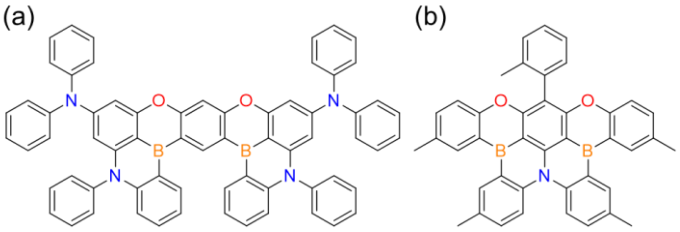

Figure 1-12. Chemical structures of (a) **BOBO-Z** and (b) **2B-DTACrs**.

However, up to the date, blue MR-TADF OLEDs satisfying BT.2020 and exhibiting EQE_{max} greater than 20% have rarely been reported due to their inherent drawbacks as mentioned in **Section 1.5**. Furthermore, In TADF compounds, deep blue emission is challenging to attain as it necessitates maintaining a small ΔE_{ST} while maintaining a sufficiently high HOMO-LUMO gap to emit deep blue. Hence, the pursuit of highly efficient, pure blue narrowband emitters that effectively harvest triplets remains a pressing concern for the OLED industry.

1.6. OLED efficiency

Not only the color purity, but the high-efficiency devices are also crucial for the commercialization of OLEDs. The efficiency of an OLED is mainly characterized by its external quantum efficiency, which can be defined as the ratio of the number of photons emitted from the OLED to the number of injected charge carriers. Device EQE can be influenced by several factors, including the emitter's intrinsic characteristics as well as external factors. Theoretically, the maximum EQE of an OLED can be expressed by **Eq. 12**.[44]

$$EQE = \eta_\gamma \times \gamma \times \eta_{OC} \times \Phi_{PL} \qquad \textbf{Eq. 12}$$

η_γ denotes the efficiency of radiative exciton production and it is highly dependent on the k_{RISC}. While the fluorescent emitters can only reach η_γ = 0.25 due to their inability to harvest triplets, TADF emitters can theoretically achieve η_γ = 1.[44] γ represents the charge balance factor. A balanced hole and electron transportation within OLEDs is crucial for charge carrier recombination to occur in the emitting layer. An imbalance in charge carriers can shift the recombination zone to the carrier-blocking layers, reducing the recombination zone and leading to emission broadening and device degradation. Charge balance can be achieved by properly managing the device architecture, such as selecting appropriate carrier transporting materials based on their HOMO/LUMO levels and charge transporting properties, adjusting layer thicknesses.[44] The γ of an OLED with balanced charge carrier flow is equal to unity. η_{OC} denotes the light out-coupling efficiency and it is governed by several factors, such as the dipole orientation of the emitter in the host material as well as the refractive indices of the device layers.[45] The improved η_{OC} is achieved with horizontally oriented emitters in the host matrix.[29,45] As described in the **Section 1.3.1**, emitters with high Φ_{PL} will grant high EQEs.

1.7. Motivation for this study

As mentioned in **Section 1.5**, developing efficient deep-blue MR-TADF (molecularly engineered, thermally activated delayed fluorescence) emitters presents a significant challenge. Particularly, deep-blue MR-TADF emitters satisfying the BT.2020 color standard with simultaneously achieving high EQE and narrowband emission have seldom been reported. **Figures 1-13** and **14** represent the summary of a blue/deep blue TADF and MR-TADF emitters (selected considering their EQEs and CIE_y values) that had been reported when I started this study.[42,46–56] from the illustration, it is clear that the demand for the novel deep-blue emitters aiming high color purity and high efficiency.

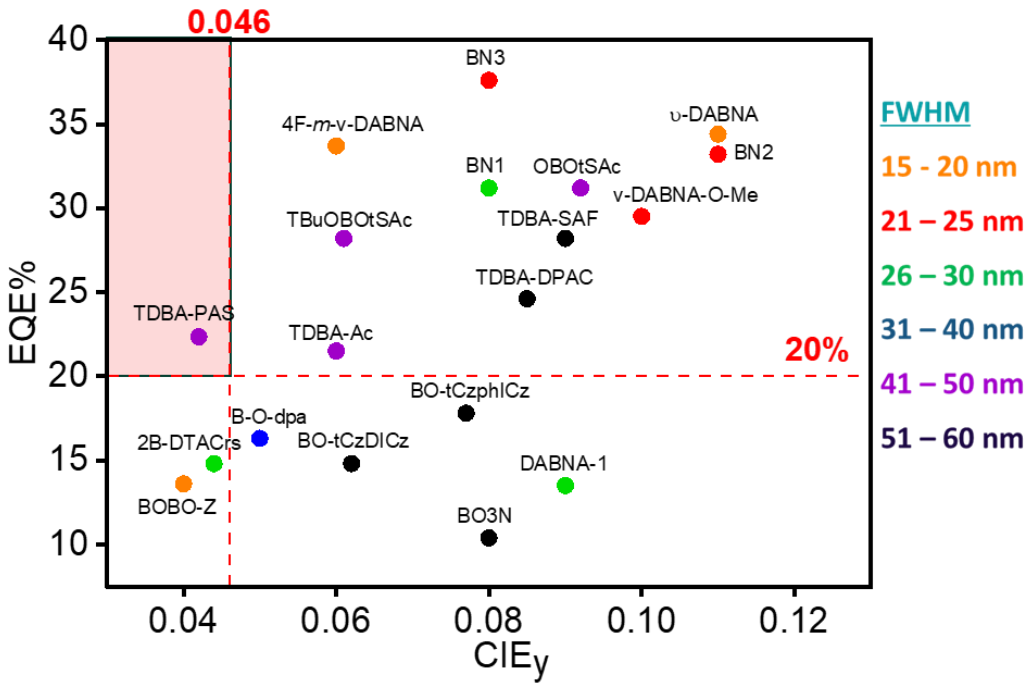

Figure 1-13. EQE vs CIE_y values of reported TADF/MR-TADF molecules with corresponding FWHMs.

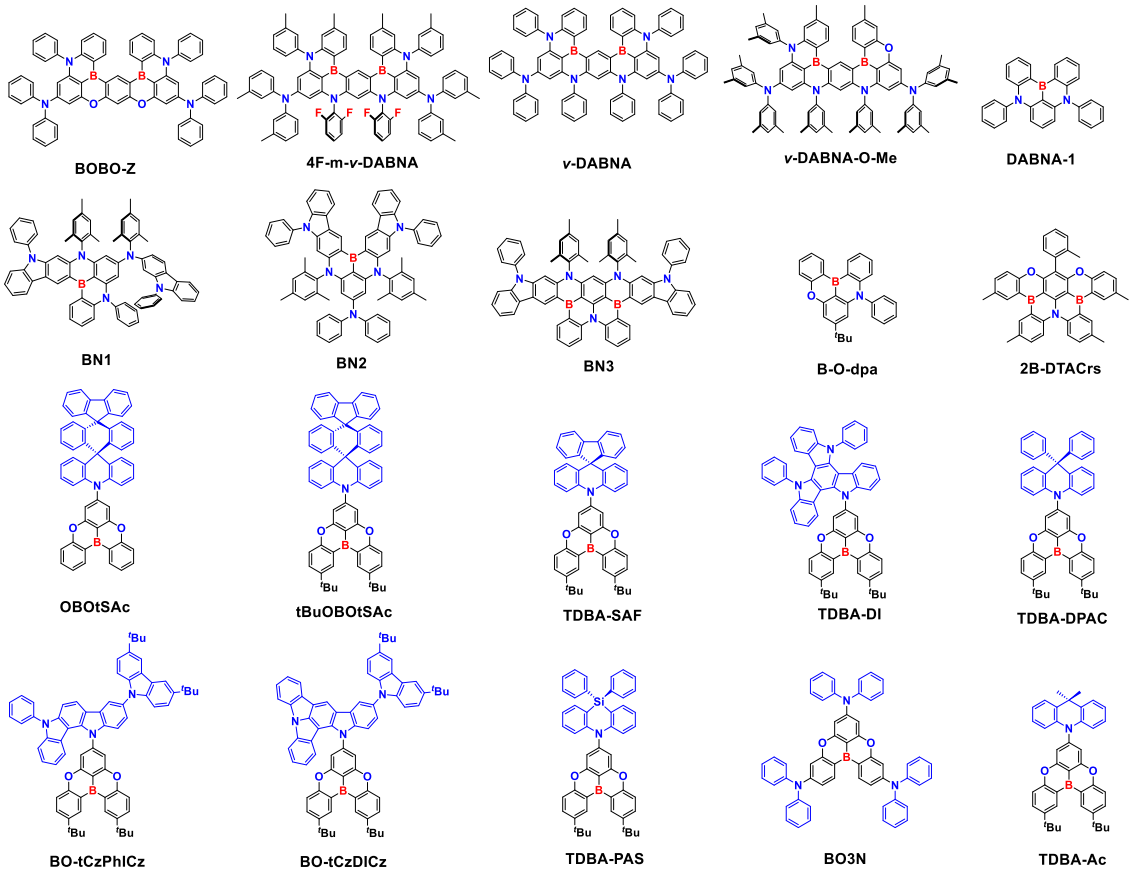

Figure 1-14. Chemical structures of reported TADF/MR-TADF emitters are shown in **Figure 1-13**.

This study aims to develop deep-blue MR-TADF emitters to mitigate common issues associated with MR-TADF emitters (slow k_{RISC}, moderate $\Delta E_{ST,}$ etc.), and device application for archiving high EQE with high color purity aiming BT.2020. In this thesis, I report the synthesis, photophysical, and device characterization of novel deep-blue MR-TADF emitters aimed at high efficiency and high color purity.

In **Chapter 2**, I introduced two deep-blue MR emitters, **1B-CzCrs** (asymmetric) and **2B-CzCrs** (symmetric), synthesized by incorporating a carbazole moiety into the MR core of previously reported emitters, **1B-** and **2B-DTACrs**. The carbazole addition induced the appearance of TADF properties in the asymmetric **1B-CzCrs** but resulted in reduced k_{RISC} in the symmetric structure. The best performance was obtained from the OLED with **1B-CzCrs** in the ***m*CP** host, achieving a CIE of (0.146, 0.06) and an EQE of 12.8%. Although I could not achieve the desired performances, based on this study, I suggested that molecular asymmetry and MR core planarization can enhance TADF properties, guiding future MR-TADF emitter designs.

In **Chapter 3**, I employed a novel molecular design approach to achieve my target. In this regard, **Chapter 3** introduces a narrowband deep-blue helical MR-TADF emitter, ***f*-DOABNA**, incorporating B, N, and O heteroatoms. ***f*-DOABNA** exhibited high PLQY (93%) and an exceptionally fast k_{RISC} rate of 1.02×10^{-6} s^{-1} in toluene, addressing common drawbacks of MR-TADF emitters without compromising color purity. With the **DOBNA-Tol** host, ***f*-DOABNA** showed further enhanced k_{RISC} and an exceptionally short delayed lifetime of 0.5 μs. The device with the ***m*CP** host met the BT.2020 standard for blue pixels, achieving a high EQE_{max} of nearly 20%. Despite the severe efficiency roll-off observed in the devices, this study demonstrated a promising molecular design strategy for deep-blue MR-TADF emitters to achieve highly efficient OLEDs with high color purity.

Finally, in **Chapter 4**, I summarized and concluded both studies and proposed future directions based on this study.

Chapter 2

Molecular asymmetry and rigidification as strategies to activate and enhance thermally activated delayed fluorescence in deep-blue MR-TADF emitters

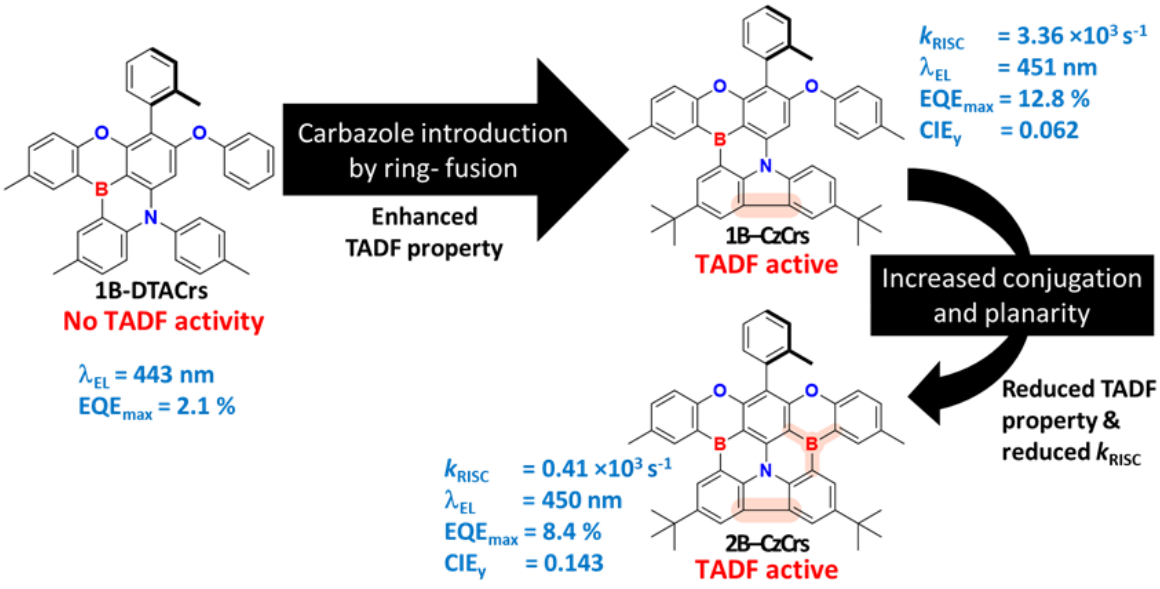

2.1. Introduction

As mentioned in **Section 1.4**, developing efficient deep-blue MR-TADF emitters with high color purity presents a significant challenge. Aromatic tertiary amine (ATA) which is often ring-fused by boron atoms has been widely used for the construction of deep-blue MR-TADF emitters as an electron donating group. The ATA moiety having an unfused phenyl group such as diphenylamine (DPA) shows less photochemical stability than that of fused structures (ex, carbazole). The rigidity of the carbazole unit can effectively suppress non-radiative decay. Therefore, carbazole-derived TADF materials usually show superior properties, including enhanced oscillator strength and decreased non radiative decays.[57,58] Bae *et al.,* recently reported that the ring-fusion forming a carbazole moiety is an important factor in providing the TADF property at the minimum component of MR-emitter (**Figure 2-1**).[59]According to the study, the original BN 1 core was TADF inactive yet upon planarization of the B- and N-phenyl groups via ring-fusion, induced TADF, particularly by the carbazole formation through planarization of the N-phenyl moiety significantly the enhancing SOC. Among these, BN 4 exhibited superior TADF characteristics with the highest k_{RISC} among them owing to its high planarity.

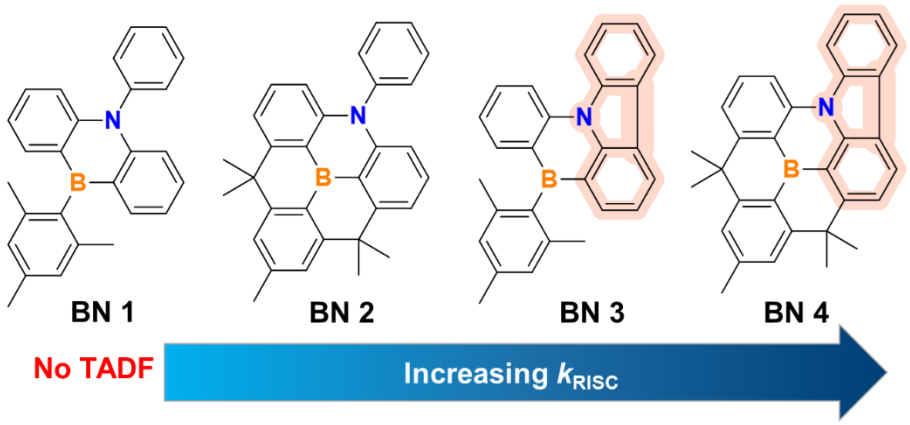

Figure 2-1. Planarization of the B- and N-phenyl groups via ring-fusion.

B, N embedded MR-TADF with ATA units often modified by replacing the nitrogen atoms with other heteroatoms for the color and emissivity control.[26,40] In a previous report, Chan *et al.* reported DPA-based deep-blue MR emitters, **1B-** and **2B-DTACrs** achieving $CIE_y \leq 0.05$.[43] **1B-DTACrs** showed Φ_{PL} of 99% without the TADF property, and **2B-DTACrs** showed the TADF property with the fast reverse intersystem crossing rate ($k_{RISC} \sim 10^5$), while the Φ_{PL} was 64%.

In this study, two novel deep-blue MR TADF emitters, **1B-** and **2B-CzCrs**, were synthesized by incorporating a carbazole unit into the MR core to reveal the effect of carbazole units on the TADF properties of MR emitters. Compared to the previously reported DPA-based **1B-DTACrs**, the carbazole-containing **1B-CzCrs** showed TADF activity, as well as **2B-CzCrs**. Despite having bulky substituents, these emitters were associated with ***m*CP** hosts even at low doping concentrations and showed a tendency for vertical alignment despite their high planarity. Both emitters exhibited deep blue emission in toluene with CIE_y < 0.046, with high Φ_{PL}. Moreover, the asymmetrical **1B-CzCrs** showed better TADF properties compared to that of **2B-CzCrs**.

2.2. Results and Discussion

2.2.1. Molecular design

In this study, **1B-** and **2B-CzCrs**, were synthesized using **1B-** and **2B-DTACrs** as the parent molecules. DPA units of the parent molecules were replaced by introducing carbazole moieties for their core structures via ring-fusing to the MR core. Thereby achieving increased conjugation and planarization of the MR cores in **1B-** and **2B-CzCrs** compared to their respective parent emitters (**Figure 2-2**). However, the highly planarized structure can facilitate the aggregation of MR emitters. To minimize this, turt-butyl groups had been introduced to the carbazole moieties in **1B-** and **2B-CzCrs** as peripheral steric hindrance groups.

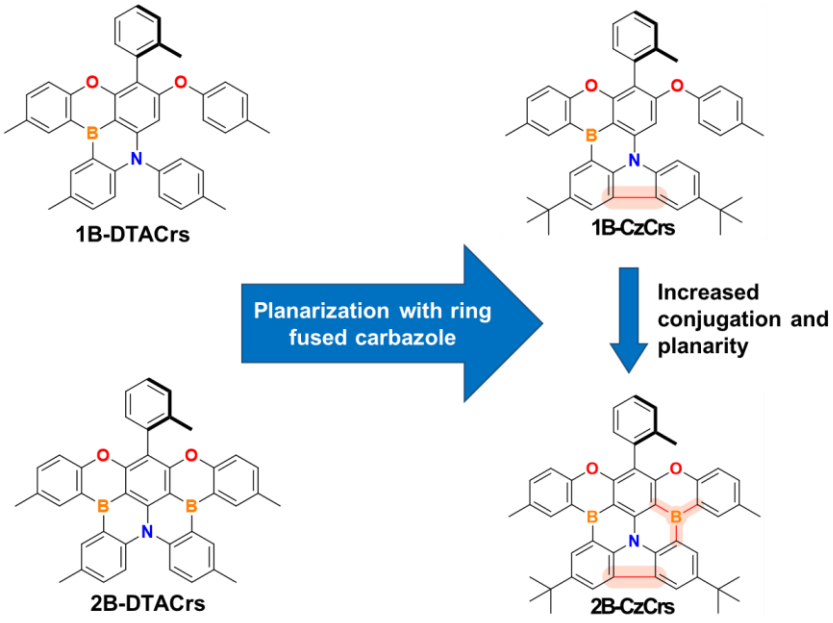

Figure 2-2. Molecular design strategy of the **1B-** and **2B-CzCrs**.

2.2.1. Theoretical calculations

The ground state optimizations were carried out using the DFT with the PBE0 functional and the 6-31G(d,p) basis set in the gas, whereas the excited state optimizations were carried out using the time-dependent within the Tamm-Dancoff approximation (TDA)-DFT with the same functional and the basis in the gas phase (**Figure 2-3**). Above calculations were performed by Zyzman-Colman group at St Andrews University, UK. Based on the ground state geometry, the HOMO-LUMO band gaps were determined to be 3.88 eV for **1B-CzCrs** and 3.77 eV for **2B-CzCrs**. Comparison with the previously reported **1B-** and **2B-DTACrs** (with a band gap of 4.03 eV) revealed that the band gaps in both **1B-** and **2B-CzCrs** were reduced due to the incorporation of the fused-ring carbazole moiety, which enhances the conjugation length (**Figure 2-3** and **Table 2-1**). This trend was also confirmed by the cyclic voltammetry measurements.

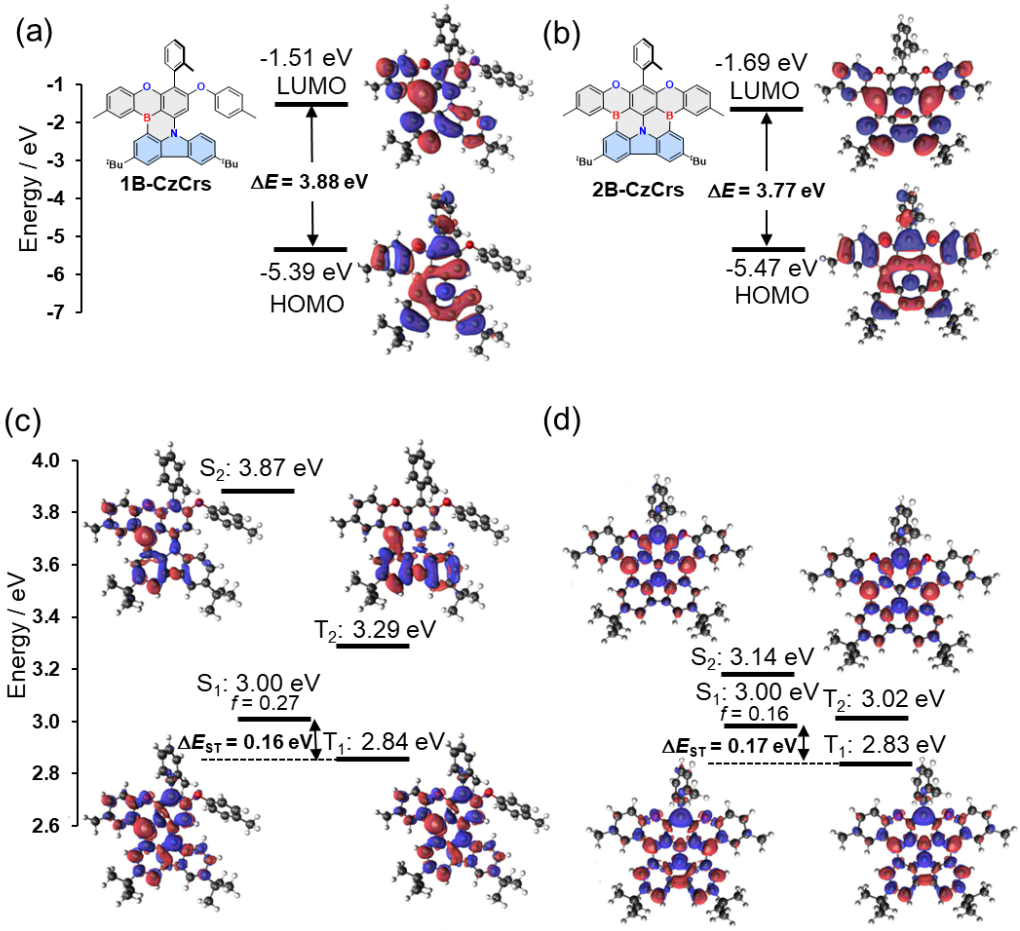

Figure 2-3. (a) Theoretical calculations of HOMO and LUMO electron density distributions of **1B-CzCrs** (left) and **2B-CzCrs** (right), (b) Excited-state energies and difference density plots of S_1, S_2, T_1, and T_2 calculated at SCS-CC2/cc-pVDZ (gas phase) based on the respective S_1 and T_1 optimized excited-state geometries of **1B-** and **2B-CzCrs**.

Table 2-1. HOMO, LUMO, and E_g values of **1B-CzCrs**, **2B-CzCrs**, **1B-DTACrs**, and **2B-DTACrs**.

Compound	By DFT calculations			By electrochemistry		
	HOMO (eV)	LUMO (eV)	E_g (eV)	HOMO (eV)	LUMO (eV)	E_g (eV)
1B-CzCrs	−5.39	−1.51	3.77	−5.60	−2.47	3.13
2B-CzCrs	−5.47	−1.69	3.88	−5.62	−2.52	3.10
1B-DTACrs[a]	−5.27	−1.24	4.03	−5.42	−2.24	3.17
2B-DTACrs[a]	−5.38	−1.47	3.91	−5.51	−2.46	3.05

[a] Reported values in literature[43]

According to the excited state geometry, the S_1-T_1 energy gaps estimated for both emitters were almost similar, giving 0.16 and 0.17 eV, for **1B-** and **2B-CzCrs**, respectively (**Figure 2-3** and **Table 2-2**). However, **1B-CzCrs** showed a larger oscillator strength (0.27) than that of **2B-CzCrs** (0.16). This discrepancy can be attributed to the significant orbital overlap between the HOMO and LUMO due to the asymmetric structure of **1B-CzCrs** yet maintaining the SRCT configuration in S_1 and T_1 states by the alternative electron density distribution.

Table 2-2. Excited state energy levels and *f* values for **1B-** and **2B-CzCrs** (at SCS-CC2/cc-pVDZ: gas phase).

Compound	S_1 (eV)	S_2 (eV)	T_1 (eV)	T_2 (eV)	$\Delta E_{S1\text{-}T2}$ (eV)	*f*
1B-CzCrs	3.00	3.87	3.84	3.29	0.16	0.27
2B-CzCrs	3.00	3.14	2.83	3.02	0.17	0.16

2.2.3. Photophysical study

The solution state steady-state photophysical properties of **1B-** and **2B-CzCrs** were studied in toluene (1.00×10^{-5} mol dm^{-3}) and the results are depicted in **Table 2-3** and **Figure 2-4**. Both emitters give absorption bands below 350 nm that arise from the locally excited (LE) π-π* transitions, whereas the absorption bands around 400 nm arise from SRCT transitions. Due to the closely lying S_2 and S_1, the split absorption bands that appear in **2B-CzCrs** at 405 and 431 nm are attributed to the S_0-S_2 and S_0-S_1 transition, respectively

(**Figure 2-3d**). As predicted in the computational study, **1B-CzCrs** with higher *f* showed stronger S_0-S_1 absorption than **2B-CzCrs**. **1B-** and **2B-CzCrs** showed narrowband emission in the blue region (446 nm and 441 nm, respectively) with FWHM values of 24 nm and 19 nm, for **1B-** and **2B-CzCrs**, respectively (**Table 2-3**). The estimated CIE_y values for both emitters in toluene were $CIE_y < 0.04$, indicating their potential for deep-blue OLED with high color purity.

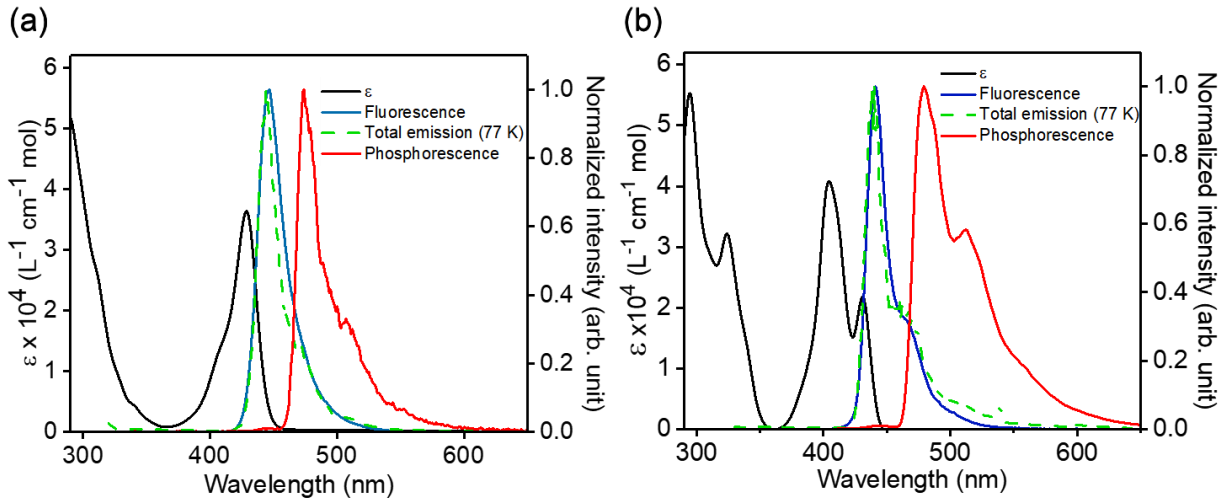

Figure 2-4. Absorption (black lines), steady-state PL at RT (blue lines, λ_{exc} = 310 nm), total emission at 77 K (green dashed lines), and phosphorescence spectra at 77 K (red lines, delay 115 ms, gate 150 ms) of (a) **1B-CzCrs** and (b) **2B-CzCrs** in toluene.

Table 2-3. Photophysical data of **1B-** and **2B-CzCrs** in toluene.

Emitter	Φ_{PL} [a] (O_2/N_2) (%)	λ_{PL} (nm)	FWHM (nm)	S_1 [b] (eV)	T_1 [c] (eV)	ΔE_{ST} (eV)	τ_p [d] (aerated/N_2) (ns)
1B-CzCrs	63/96	446	24	2.89	2.68	0.21	5.37/6.57
2B-CzCrs	55/94	441	19	2.91	2.67	0.24	6.52/8.70

[a] Measured using an integrating sphere at λ_{exc} = 310 nm. [b] Estimated from the onset wavelength of the steady-state PL spectrum at 77 K. [c] Estimated from the onset wavelength of the delayed emission spectrum (115–150 ms) at 77 K (λ_{exc} = 310 nm). [d] Measured with a streak camera at λ_{exc} = 355 nm.

1B- and **2B-CzCrs** provided narrower FWHM than that of their respective parent molecules, **1B-DTACrs** (27 nm) and **2B-DTACrs** (21 nm).[16] This can be ascribed to the

rigidification of MR core in **1B-** and **2B-CzCrs** compared to their parent molecules, by introducing the carbazole moiety (**Figure 2-5**). These rigid aromatic structures with seven fused rings effectively limit the molecular structural distortion, thereby suppressing the vibration losses, which enables narrowband emission in **1B-** and **2B-CzCrs**.

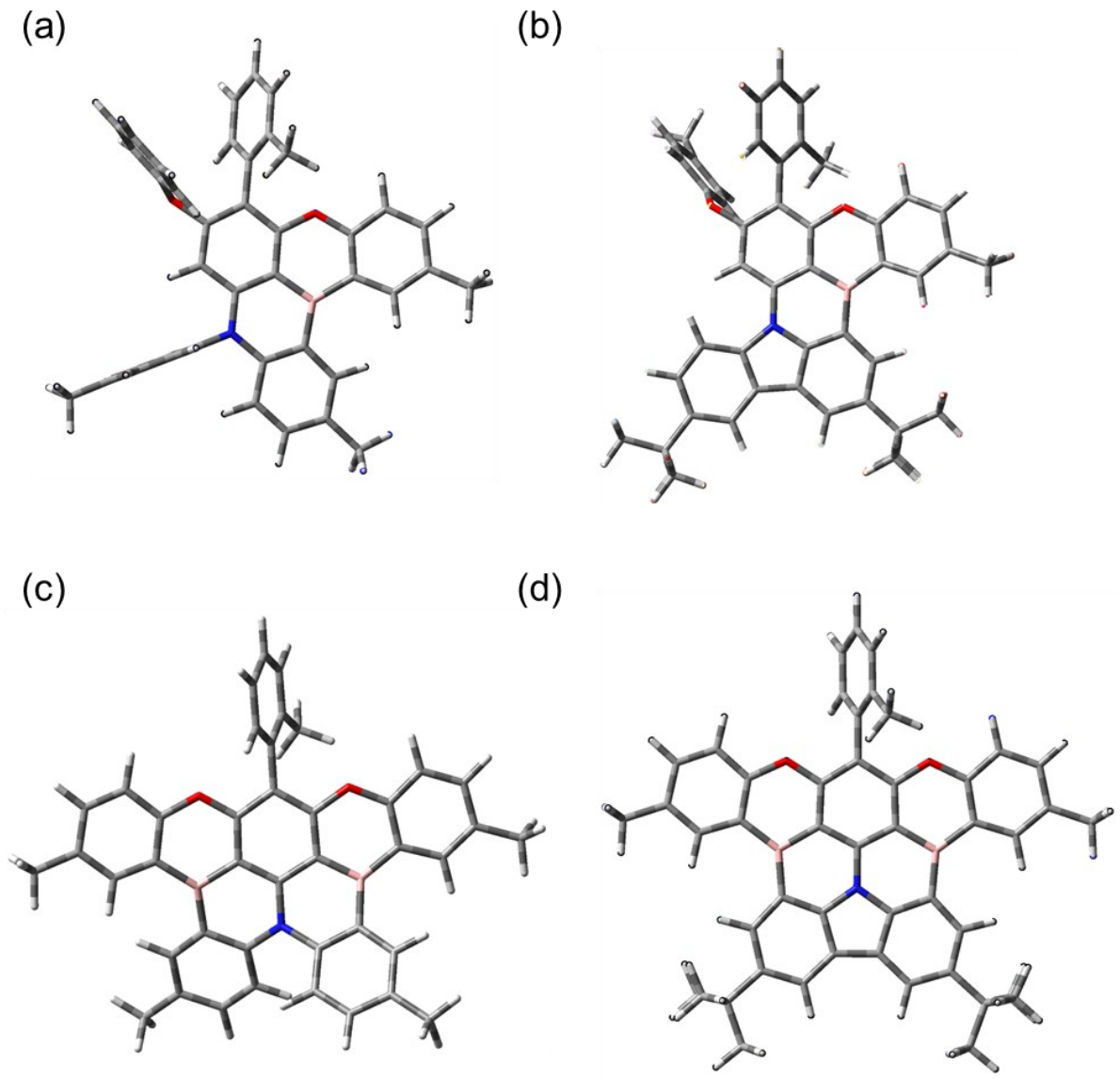

Figure 2-5. Ground state optimized structures of the (a) **1B-DTACrs**, (b) **1B-CzCrs**, (c) **2B-DTACrs**, and (d) **2B-CzCrs** (calculated by DFT with PBE0/6-31G(d,p) level of theory).

The ΔE_{ST} values for **1B-** and **2B-CzCrs** were calculated using the onset of fluorescence and phosphorescence spectra at 77 K, after applying the Jacobian conversion,[60] resulting in values of 0.20 and 0.24 eV, respectively. These values were in agreement with the theoretical ΔE_{ST} values calculated at SCS-CC2/cc-pVDZ level of theory. In aerated solutions, **1B-** and **2B-**

CzCrs showed Φ_{PL} of 63 and 55%, respectively, and they were significantly increased to 96 and 94 % under N_2 saturated condition, indicating the significant contribution of a triplet excited state in the light emitting process. The high Φ_{PL} values can be attributed to their rigid structure with several fused rings, which minimizes nonradiative decay. However, the transient decay profiles of **1B-** and **2B-CzCrs** only exhibited a short single-component decay lifetime in toluene within the maximum time range of the Streak camera system (**Figure 2-4**). This can be attributed to the non-radiative decay which competes with RISC, regardless of the high Φ_{PL}. Under N_2 saturated conditions, a slight increment in the lifetimes can be seen, suggesting that oxygen might affect the singlet radiative decay rates.[61]

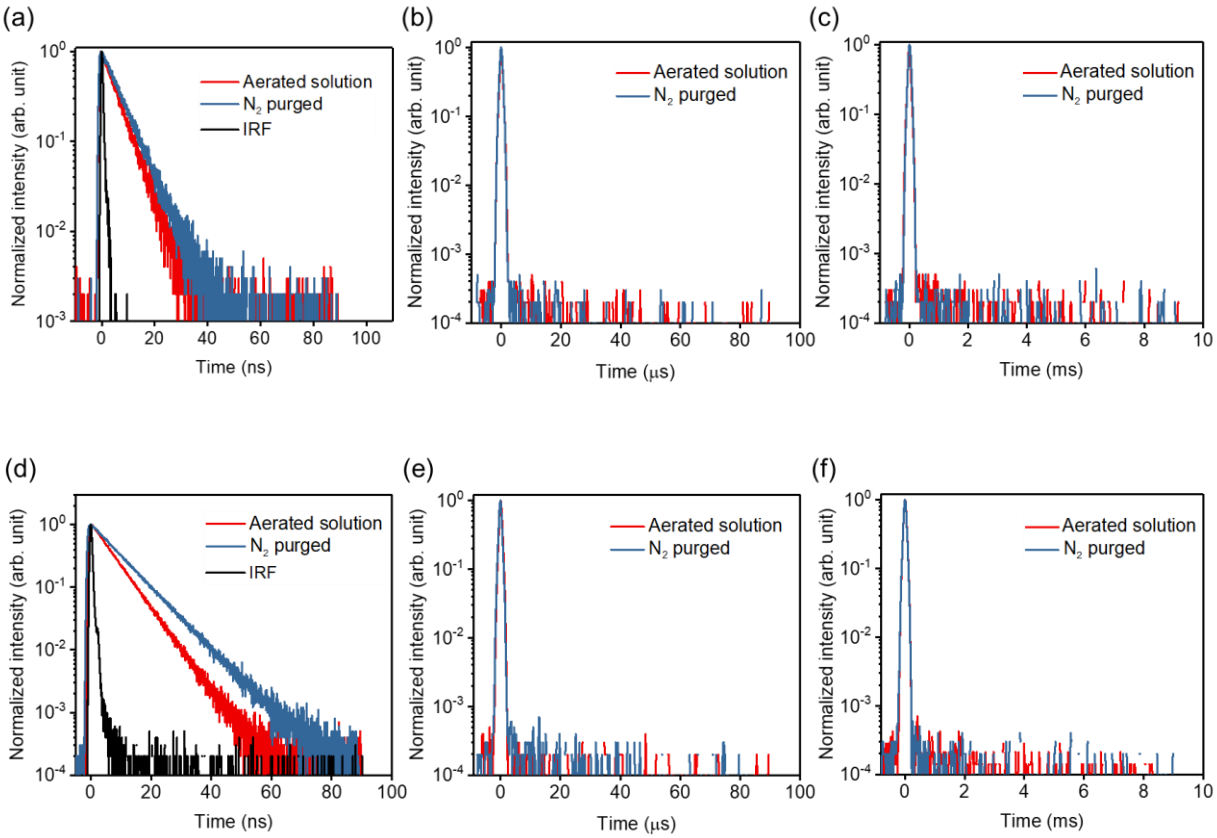

Figure 2-6. Transient decays of **1B-CzCrs** (a, b, c) and **2B-CzCrs** (d, e, f) in toluene at 100 ns (a, d), 100 μs (b, e), and 10 ms (c, f) time ranges under aerated (red) and N_2-purged (blue) conditions. (Prompt time range measurements (100 ns) were taken with Quanturus-Tau at λ_{exc} = 340 nm, while 100 μs and 10 ms range measurements were taken using the Streak camera measurement system at λ_{exc} = 355 nm).

Next, the film state photophysics of both emitters was investigated by fabricating doped films with 5 wt% MR-emitters in 3,3′-di(9*H*-carbazol-9-yl)-1,1′-biphenyl (***m*CBP**) host matrix (**Figure 2-7** and **Table 2-4**). 5 wt% **1B-** and **2B-CzCrs** doped in ***m*CBP** exhibited deep blue emission at 451 nm and 449 nm, respectively, and slightly broadened emission with FWHMs of 28 nm. The observed Φ_{PL} values for 5 wt% doped **1B-** and **2B-CzCrs** under Ar-saturated conditions were 67 and 59%, respectively.

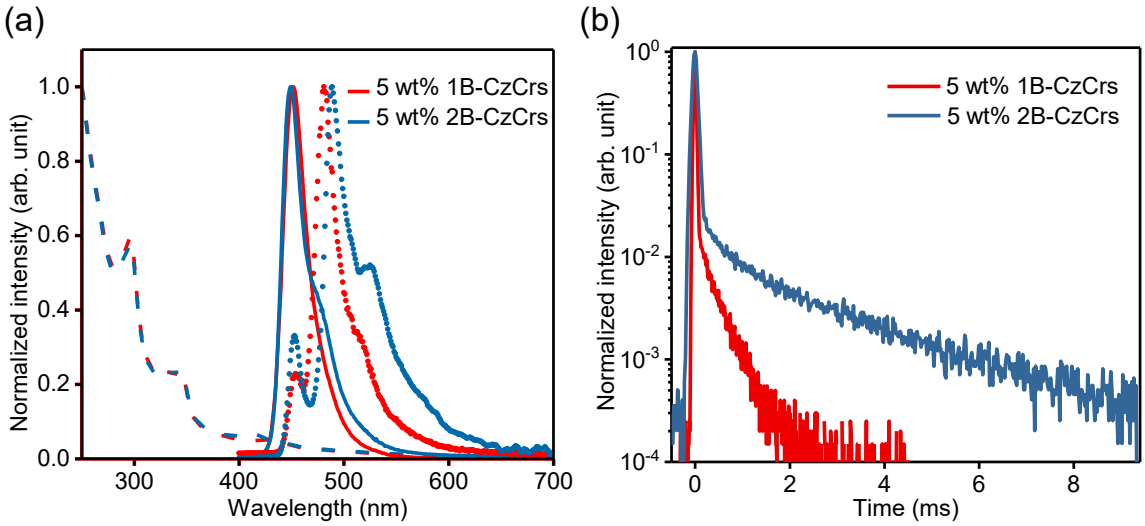

Figure 2-7. Photophysical properties of 5 wt% of **1B-** and **2B-CzCrs** doped in ***m*CBP** host material; (a) normalized absorption (dashed lines), PL at RT (solid lines, λ_{exc} = 310 nm), and phosphorescence at 77K (dotted lines, λ_{exc} = 310 nm), and (b) transient PL decay curves (λ_{exc} = 355 nm) at RT.

Table 2-4. Photophysical data of 5 wt% doped **1B-CzCrs**, **2B-CzCrs**, **1B-DTACrs**, and **2B-DTACrs** in ***m*CBP**.

Emitter	Φ_{PL} [a] (%)	λ_{PL} [b] (nm)	FWHM (nm)	ΔE_{ST} (eV)	τ_p [c] (ns)	τ_d [c] (ms)	k_r (10^8 s^{-1})	k_{nr} (10^7 s^{-1})	k_{ISC} (10^7 s^{-1})	k_{RISC} (10^3 s^{-1})
1B-CzCrs	67	451	28	0.20	5.08	0.33	1.19	5.86	1.88	3.36
2B-CzCrs	59	449	28	0.24	8.63	2.98	0.58	4.03	1.75	0.41
1B-DTACrs[d]	83	443	28	0.21	10	-	-	-	-	-
2B-DTACrs[d]	74	448	24	0.16	2	0.013	1.7	6.1	33.0	130.0

[a] Absolute Φ_{PL} of thin films was measured using an integrating sphere under Ar saturated conditions. [b] Fluorescence maximum at RT (λ_{exc} = 310 nm). [c] Observed at emission peak wavelength. [d] Reported values from the literature.[43]

Although both emitters showed deep blue emission in ***m*CBP**, the emission was slightly broadened compared to the emission of the emitters in the solution state. This broadened emission and the reduced Φ_{PL} in the film state can be attributed to the molecular aggregations due to the planner structures of these molecules (**Figure 2-5**). This behavior was also evident in **1B-** and **2B-DTACrs**.[43] However, a more pronounced degree of spectral broadening and a reduction in Φ_{PL} values were observed in **1B-** and **2B-CzCrs** compared to their parent molecules. These findings strongly indicate that the planar carbazole-containing emitters are inclined to form aggregates in their film state. This propensity persists despite the incorporation of tert-butyl groups in the molecular structure of these compounds as well as the presence of a bulky o-tolyl group. Moreover, the narrowing of the emission spectra and the increased Φ_{PL} at lower doping concentrations in **1B-** and **2B-CzCrs** validate this assertion (**Figure 2-8** and **Table 2-5**). The aggregations were more prominent in the more planner **2B-CzCrs**.

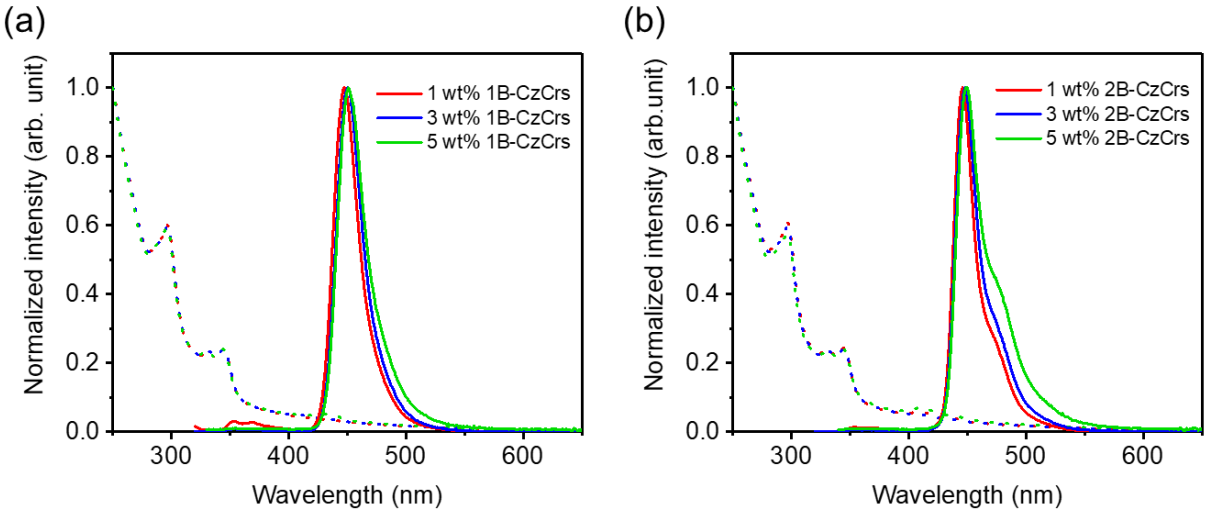

Figure 2-8. Absorption (dotted lines) and fluorescence (solid lines) spectra of (a) **1B-CzCrs** and (b) **2B-CzCrs** doped ***m*CBP** films at the various concentrations (λ_{exc} = 310 nm).

Table 2-5. Photophysical data of 1, 3, and 5 wt% doped **1B-** and **2B-CzCrs** in ***m*CBP** and corresponding CIE values.

Emitter	wt%	$\Phi_{PL(Ar)}$[a] (%)	λ_{PL} [b] (nm)	FWHM (nm)	CIE (x,y)
1B–CzCrs	1	75.5	447	25	0.151, 0.037
	3	82.7	450	26	0.148, 0.043
	5	67.2	451	28	0.151, 0.065
2B–CzCrs	1	86.9	446	20	0.149, 0.043
	3	72.7	448	23	0.147, 0.053
	5	58.9	449	28	0.150, 0.088

[a] Absolute Φ_{PL} of thin films was measured using an integrating sphere at λ_{exc} = 340 nm. [b] Fluorescence maximum at RT. (λ_{exc} = 310 nm). [e] Under vacuum conditions (λ_{exc} = 355 nm).

Subsequently, the transient decay profiles of the doped films were examined under vacuum conditions. Interestingly, both doped films with **1B-** and **2B-CzCrs** exhibited delayed emission, confirming TADF activity in both emitters. The rate constants for both doped films with **1B-** and **2B-CzCrs** were calculated according to a previously reported method in the literature and are summarized in **Table 2-5**.[62] Compared to the 5 wt% doped **2B-CzCrs (**k_{RISC} = 0.41 × 10^3 s^{-1}, τ_d = 2.98 ms), the 5 wt% doped **1B-CzbCrs** exhibited faster k_{RISC} with a shorter τ_d **(**k_{RISC} = 3.36 × 10^3 s^{-1}, τ_d = 0.33 ms). It is worth noting that **1B-DTACrs** did not exhibit TADF behavior, but **1B-CzCrs** showed delayed emission. As mentioned in **Section 2.1**, the ring fusion forming a carbazole moiety plays a crucial role in conferring the TADF property at the minimum component of MR-emitter.[59] This trend was also followed in **1B-CzCrs** and **1B-DTACrs**. Notably, contrary to the trend in the parent molecules, better TADF properties were observed in asymmetric **1B-CzCrs** compared to the symmetric **2B-CzCrs** with one-order of higher k_{RISC} in **1B-CzCrs** than in **2B-CzCrs**. However, the k_{RISC} values for **1B-** and **2B-CzCrs** were two orders different from that of **2B-DTACrs** (1.3 × 10^5 s^{-1}) and also the τ_d of **1B-** and **2B-CzCrs** were longer than that of the **2B-DTACrs** (13.1 μs).[43]

Therefore, for further understanding, the SOC magnitudes were investigated with PBE0/6-31g(d,p) level of theory in the gas phase. Calculated SOC values for each optimized S_0, S_1, T_1, and T_2 geometry are depicted in **Table 2-6**. For the comparison, the SOC values for **1B-** and **2B-DTACrs** were also calculated using the same method. Considering the T_1 optimized geometry, the SOC value between T_1 and S_1 for **1B-CzCrs** was 0.119 cm^{-1}, a twofold higher value compared with the SOC value of the **2B-CzCrs**, 0.059 cm^{-1}. Furthermore, the

SOC between T_2 and S_1 was also higher for **1B-CzCrs**, giving **SOC** values of 0.100 and 0.060 cm^{-1} for **1B-** and **2B-CzCrs**, respectively. Considering the **SOC** values, it is evident that asymmetric **1B- CzCrs** have faster k_{RISC} than symmetric **2B-CzCrs**. However, the SOC values for both **1B-** and **2B-CzCrs** were significantly smaller compared to those of **2B-DTACrs**, resulting in slower k_{RISC} values for **1B-** and **2B-CzCrs** than for **2B-DTACrs**. These results suggest that the extension of π-conjugation through carbazole formation has both advantages and disadvantages: enhancing the TADF property (from TADF inactive **1B-DTACrs** to TADF active **1B-CzCrs**) and reducing k_{RISC} (slower k_{RISC} in **2B-CzCrs** compared to the **2B-DTACrs**).

Table 2-6. Estimated SOC values for **1B-CzCrs**, **2B-CzCrs**, **1B-DTACrs**, and **2B-DTACrs** at PBE0/6-31g(d,p) based on each optimized geometry (using ORCA software package).

	S_0 optimized		**S_1 optimized**		**T_1 optimized**		**T_2 optimized**	
Emitter	$\langle S_1 \| H_{soc} \| T_1 \rangle$ (cm^{-1})	$\langle S_1 \| H_{soc} \| T_2 \rangle$ (cm^{-1})	$\langle S_1 \| H_{soc} \| T_1 \rangle$ (cm^{-1})	$\langle S_1 \| H_{soc} \| T_2 \rangle$ (cm^{-1})	$\langle S_1 \| H_{soc} \| T_1 \rangle$ (cm^{-1})	$\langle S_1 \| H_{soc} \| T_2 \rangle$ (cm^{-1})	$\langle S_1 \| H_{soc} \| T_1 \rangle$ (cm^{-1})	$\langle S_1 \| H_{soc} \| T_2 \rangle$ (cm^{-1})
1B-CzCrs	0.0374	0.1342	0.0640	0.1315	0.1187	0.0995	0.1187	0.0995
2B-CzCrs	0.0000	0.0592	0.0000	0.1005	0.0592	0.0600	0.0500	0.1005
1B-DTACrs	0.0748	0.4730	0.0671	0.3750	0.0458	0.3746	0.0458	0.3746
2B-DTACrs	0.0300	0.9111	0.1217	0.8810	0.3713	0.8108	0.37135	0.8108

To gain deeper insights, the temperature-dependent transient emission decay profiles of **1B-** and **2B-CzCrs** doped films were investigated, and the activation energies for ISC (E_a^{ISC}) and RISC (E_a^{RISC}) processes, and thereby the ΔE_{ST} and the effective spin-orbit coupling matrix element (SOCME) values, were estimated using the Marcus plot, based on **Eq. 13**.[59] Calculations were performed considering the two limiting conditions, k_{nr}^{T} = 0 and k_{nr}^{S} = 0 (**Figure 2-10** and **Table 2-7**).

$$\ln\left(\sqrt{T}k_{\mathrm{RISC}}\right) = -\frac{E_a^{RISC}}{k_B}\cdot\frac{1}{T} + \ln\left(\frac{2\pi}{\hbar\sqrt{4\pi\lambda k_B}}\left|\langle\psi_{\mathrm{S}}|\hat{H}_{\mathrm{SOC}}|\psi_{\mathrm{T}}\rangle\right|^2\right) \qquad \textbf{Eq. 13}$$

where T is the temperature, $\left|\langle\psi_{\mathrm{S}}|\hat{H}_{\mathrm{SOC}}|\psi_{\mathrm{T}}\rangle\right|$ is the effective SOCME, $\hbar$ is the Dirac constant, λ is the reorganization energy, and the k_{B} is the Boltzman constant. λ is given by the equation,

$$\lambda = E_a^{\mathrm{ISC}} - E_a^{\mathrm{RISC}} \pm 2\sqrt{E_a^{ISC}E_a^{RISC}} \qquad \textbf{Eq. 14}$$

where $+2\sqrt{E_a^{ISC}E_a^{RISC}}$ represents under Marcus's normal region and $-2\sqrt{E_a^{ISC}E_a^{RISC}}$ represents under the inverted region. In here, I assumed the systems are in the normal region.

The intensity of the delayed components of both emitters increased and shortened the delayed lifetime as the temperature rose from 150 K to 300 K, reinforcing the TADF properties of both emitters (**Figure 2-9**). By considering the limiting condition, k_{nr}^{T} = 0, the ΔE_{ST} estimated from the Marcus plot were significantly higher values for **1B-CzCrs** (65.9 meV) than that for **2B-CzCrs** (19.9 meV). Nevertheless, **1B-CzCrs** demonstrated significantly higher k_{RISC} than **2B-CzCrs** across the entire temperature range. This can be attributed to the larger effective SOC of **1B-CzCrs** (0.017 cm^{-1}) than that of **2B-CzCrs** (0.003 cm^{-1}). This is clear evidence of the contribution of the T_2 state to the RISC process of **1B-CzCrs**. ΔE_{ST} and effective SOC values at the limiting condition, k_{nr}^{S} = 0 also showed a similar trend.

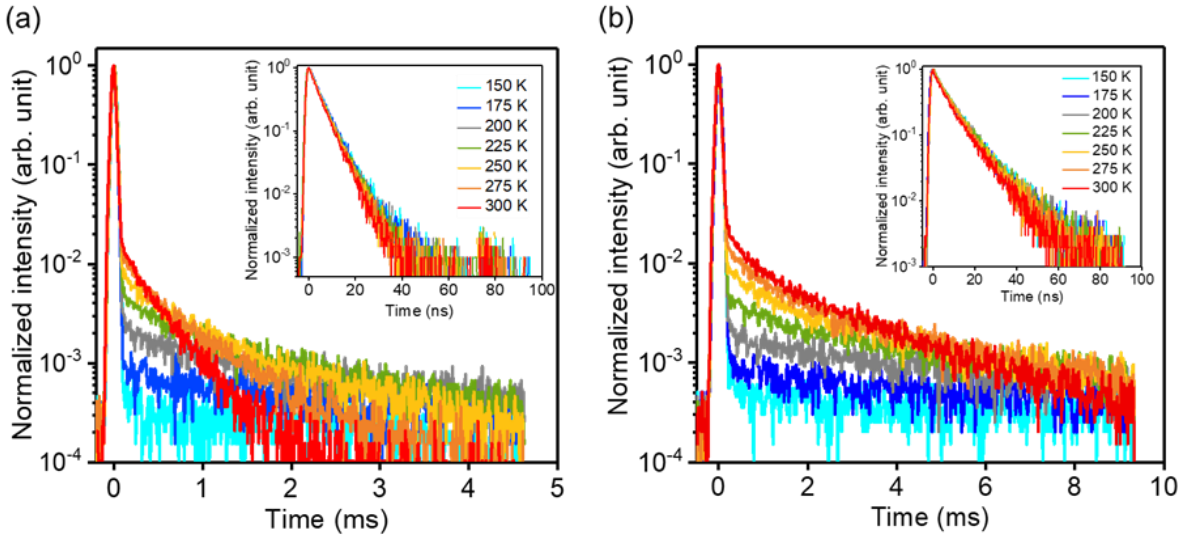

Figure 2-9. Temperature-dependent time-resolved PL decay curves of (a) 5 wt% **1B-CzCrs** in ***m*CBP**. Inset: Prompt PL decay and (b) 5 wt% **2B-CzCrs** in ***m*CBP**. Inset: Prompt PL decay.

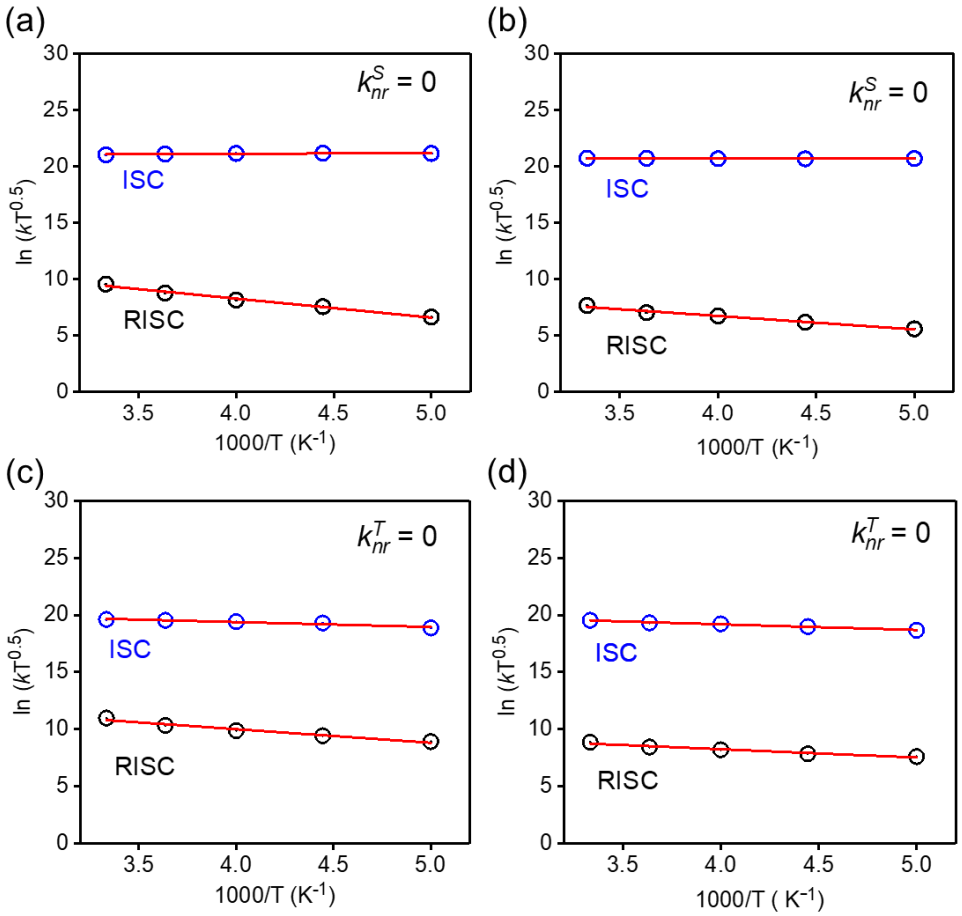

Figure 2-10. Marcus plots (for ISC and RISC) for 5 wt% doped films of **1B -CzCrs** (a, c) and **2B-CzCrs** (b, d) in ***m*CBP**, at the limit conditions of $k_{nr}^{S} = 0$ (a, b) and $k_{nr}^{T} = 0$ (c, d).

Table 2-7. Results of Marcus plot analysis for **1B-** and **2B-CzCrs** doped in ***m*CBP** (5 wt%).

	E_a^{ISC} (meV)		E_a^{RISC} (meV)		ΔE_{ST}[a] (meV)		Effective SOCME[b] for RISC (cm^{-1})	
	$k_{nr}^{S} = 0$	$k_{nr}^{T} = 0$	$k_{nr}^{S} = 0$	$k_{nr}^{T} = 0$	$k_{nr}^{S} = 0$	$k_{nr}^{T} = 0$	$k_{nr}^{S} = 0$	$k_{nr}^{T} = 0$
1B–CzCrs	-6.4	36.7	145.1	102.5	151.5	65.9	0.0181	0.0173
2B–CzCrs	2.4	43.1	102.8	63.0	100.4	19.9	0.0029	0.0027

[a] $\Delta E_{ST} = E_a^{RISC} - E_a^{ISC}$, [b] $SOCME = \sqrt{e^{\ln\beta}\hbar(4\pi\lambda k_B)^{0.5}/2\pi}$ where β is intercept of Marcus plot for k_{RISC}, $\hbar$ is Dirac constant, λ is reorganization energy ($\lambda = E_a^{ISC} + E_a^{RISC} + 2\sqrt{E_a^{ISC}E_a^{RISC}}$, assuming under Marcus's normal region), and k_B is Boltzmann constant.

The film state photophysics of **1B-** and **2B-CzCrs** were also studied in the host, 1,3-di(9*H*-carbazol-9-yl) benzene (***m*CP**). Compared with the ***m*CBP**, both emitters exhibited

slightly broadened and redshifted emission in ***m*CP**, even at 1 wt% doping concentrations (**Figure 2-8** and **Table 8**). This can be ascribed to the more polar nature of the ***m*CP** with a higher dipole moment (1.35 D) compared with the ***m*CBP** (0.8 D).[63,64] However, when the doping concentrations of the **1B-** and **2B-CzCrs** increased, both emitters showed less aggregation in the host ***m*CP** compared to those in the host ***m*CPB**, as reflected by the emission spectra of the emitters in ***m*CP** at different doping levels (**Figure 2-11** and **Table 2-8**). This reduced aggregation can be explained by the strong dipole-dipole interactions in the more polar ***m*CP** host matrix. These interactions would stabilize the individual MR dopant molecules within the ***m*CP** host matrix through dipole-dipole interactions, limiting their tendency to aggregate by reducing the attractive interactions between the dopant molecules.

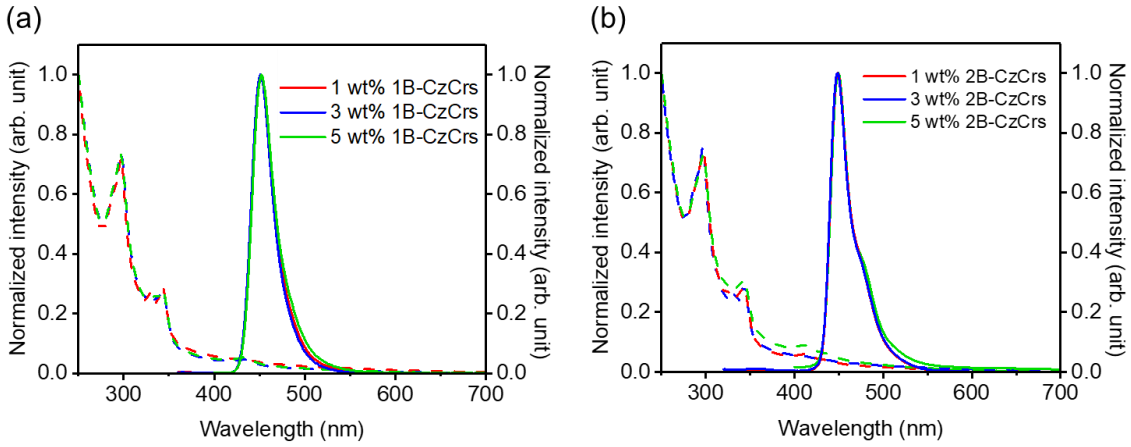

Figure 2-11. Steady-state absorption (dashed lines) and emission spectra (solid lines) of (a) **1B-CzCrs** and (b) **2B-CzCrs** at different doping concentrations in ***m*CP** (λ_{exc} = 310 nm).

Table 2-8. Steady-state photophysical properties **1B-** and **2B-CzCrs** at different doping concentrations in ***m*CP** host and corresponding CIE values.

Emitter	wt%	$\Phi_{PL_{(Ar)}}$ [a] (%)	λ_{PL} [b] (nm)	FWHM (nm)	CIE (x,y)
1B-CzCrs	1	72	451	28	0.146, 0.054
	3	79	451	28	0.145, 0.052
	5	75	452	29	0.145, 0.063
2B-CzCrs	1	65	448	25	0.141, 0.056
	3	64	448	25	0.144, 0.060
	5	62	449	26	0.145, 0.062

[a] Absolute Φ_{PL} of thin films was measured using an integrating sphere at λ_{exc} = 340 nm. [b] Fluorescence maximum at RT. (λ_{exc} = 310 nm).

2.2.4. OLED performance

To explore the electroluminescence characteristics of **1B-** and **2B-CzCrs**, TADF-OLEDs were fabricated utilizing the vacuum deposition technique. The OLED using **1B-DTACrs** was also fabricated as a reference. In pursuit of high external quantum efficiency and considering the energy level alignment, the following device structure was employed. Indium-tin-oxide (**ITO**)-coated glass (100 nm)/**HAT-CN** (10 nm)/ **TAPC** (30 nm)/***m*CP** (10 nm)/***m*CP**: 5 wt% of **1B-CzCrs** or **2B-CzCrs** (20 nm)/ **PPT** (10 nm)/ **TmPyPB** (30 nm)/ **Liq** (2 nm)/ **Al** (100 nm). Where, **ITO**, 1,4,5,8,9,11-Hexaazatriphenylenehexacarbonitrile (**HAT-CN**), 1,1-bis[(di-4-tolylamino)phenyl] cyclohexane (**TAPC**), 5 wt% of **1B-CzCrs** or **2B-CzCrs** in ***m*CP**, 2,8-Bis(diphenyl-phosphoryl)-dibenzo[b,d]thiophene (**PPT**), 1,3,5-tris(3-pyridyl-3-phenyl)benzene (**TmPyPB**), 8-hydroxyquinolinolatolithium (**Liq**) and Al are the anode, hole injection, hole-transporting, electron-blocking, emitting, hole-blocking, electron-transporting, and electron injection and cathode layers, respectively. The chemical structures of the molecules used for the OLED fabrication are depicted in **Figure 2-12**.

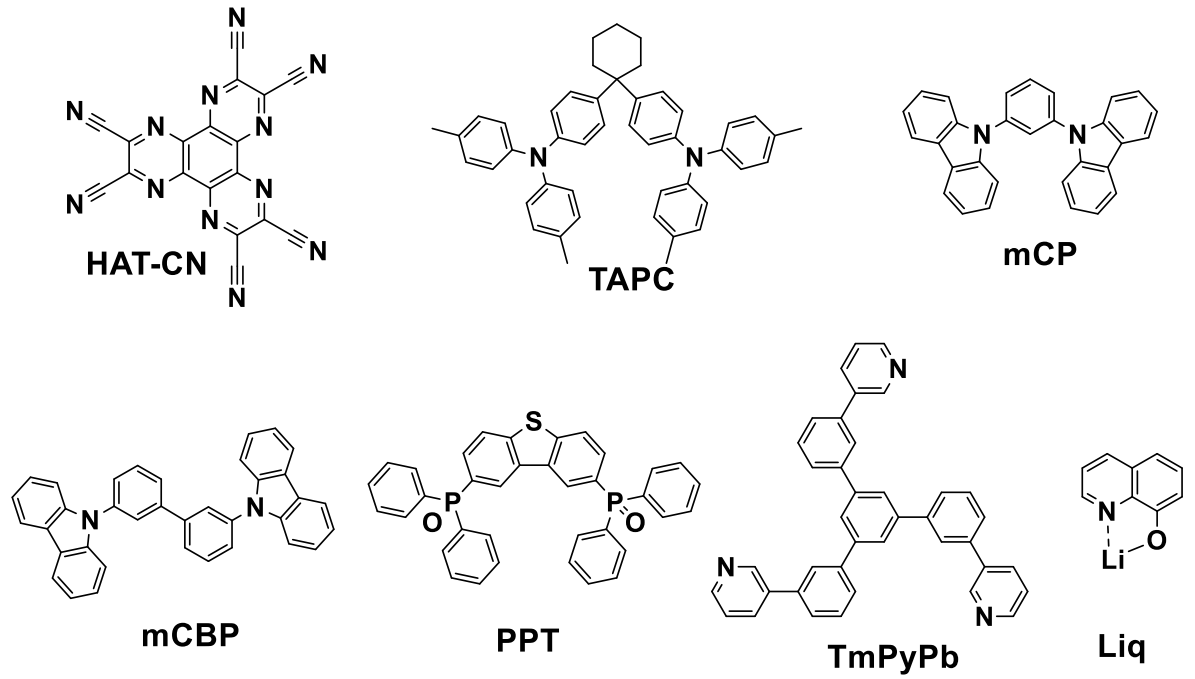

Figure 2-12. Chemical structures of the compounds used for OLEDs.

The device structure and the EL properties of these two devices are summarized in **Figure 2-13** and **Table 2-9**. The OLED based on the **1B-CzCrs** emitter exhibited a higher EQE_{max} of 12.8%, surpassing the EQE_{max} of 8.4%. This can be ascribed to the combined effect

of the faster k_{RISC}, smaller ΔE_{ST}, and higher PLQY of **1B-CzCrs** compared with those of the **2B-CzCrs**. The EL emission of **1B-** and **2B-CzCrs** were observed at 451 and 450 nm, similar to PL emission in ***m*CP**. Both devices demonstrated a relatively low turn-on voltage below 4.0 V due to enhanced carrier transport properties resulting from the incorporation of carbazole and tert-butyl groups. Furthermore, the device using **1B-CzCrs** showed a higher EQE_{max} of 12.8% than that using **1B-DTACrs** (2.1%) due to the ability of harvesting triplets in **1B-CzCrs**. This again confirms the TADF property by forming carbazole moiety in minimum MR component. Although the devices with **1B-** and **2B-CzCrs** could not satisfy BT.2020 CIE_y for blue pixels, the device with **1B-CzCrs** exhibits better CIE coordinates compared to that of **2B-CzCrs**, giving CIE coordinates of (0.146, 0.062) and (0.153, 0.143), respectively, due to the narrower EL of the device with **1B-CzCrs** (FWHM = 30 nm).

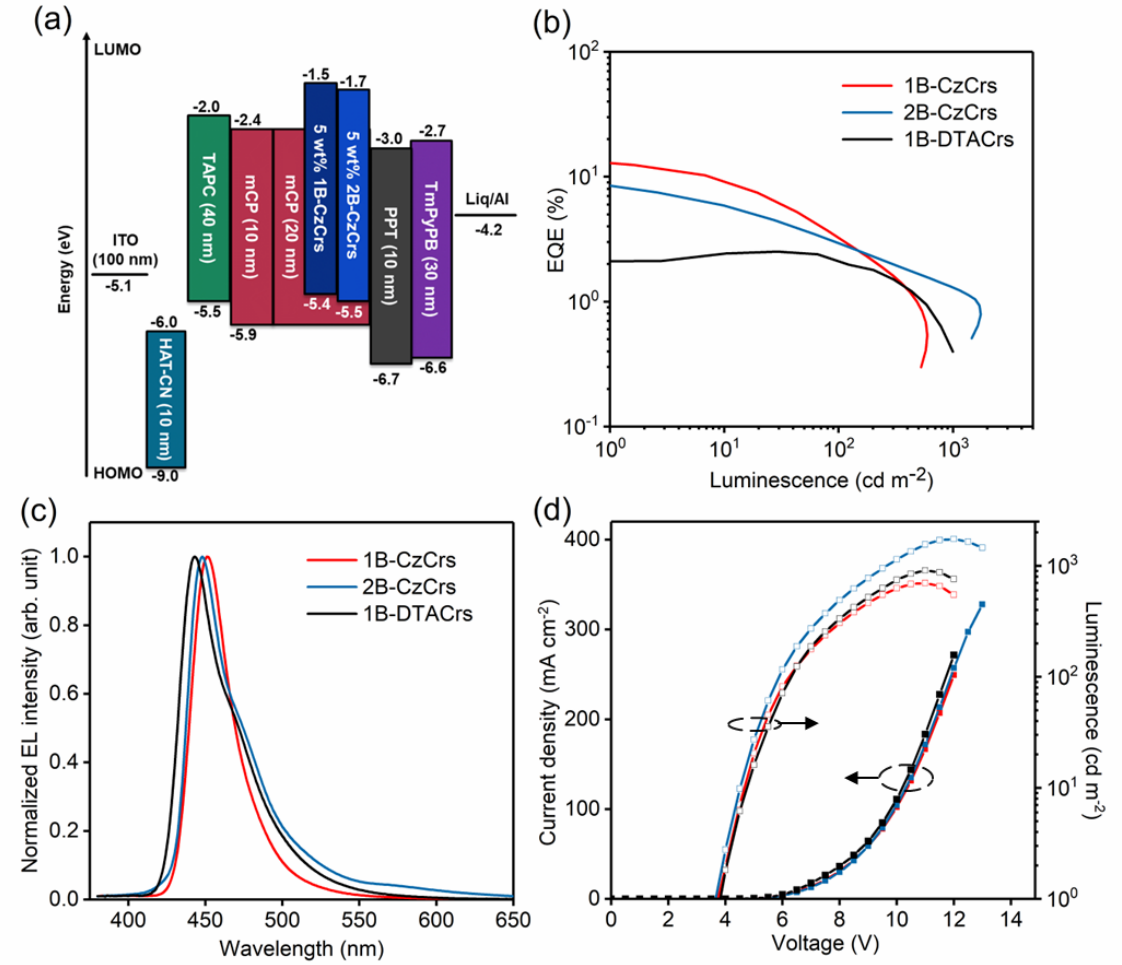

Figure 2-13. Device performance of devices with 5 wt% **1B-** and **2B-CzCrs** in ***m*CP**. (a) Device structure, (b) Graph of EQE vs. Luminescence, (c) EL spectra, and (d) Graph of current density (closed circle) and luminance (open circle) vs. driving voltage.

Table 2-9. Device performance of 5 wt% **1B-** and **2B-CzCrs** in ***m*CP** host.

Emitter	V_{on} (V)	EQE_{max} (%)	λ_{EL} (nm)	FWHM (nm)	Lum_{max} (cd m^{-2})	CIE_x	CIE_y
1B-CzCrs	3.8	12.8	451	30	688	0.146	0.062
2B-CzCrs	3.7	8.4	450	36	1712	0.153	0.143
1B-DTACrs	3.9	2.1	443	39	902	0.155	0.079

While the highest Φ_{PL} for **1B-CzCrs** in ***m*CP** (79.7%) was observed at 3 wt% of **1B-CzCrs**, the device with 3% doped **1B-CzCrs** in ***m*CP** showed inferior device performance compared to the device with 5 wt% doped **1B-CzCrs** in ***m*CP** (**Figure 2-14** and **Table 2-10**). The reason can be ascribed to the poor charge transporting characteristic of the device with 3 wt% doped **1B-CzCrs** in which a high turn-on voltage was obtained compared to the device with 5 wt% doped **1B-CzCrs**.

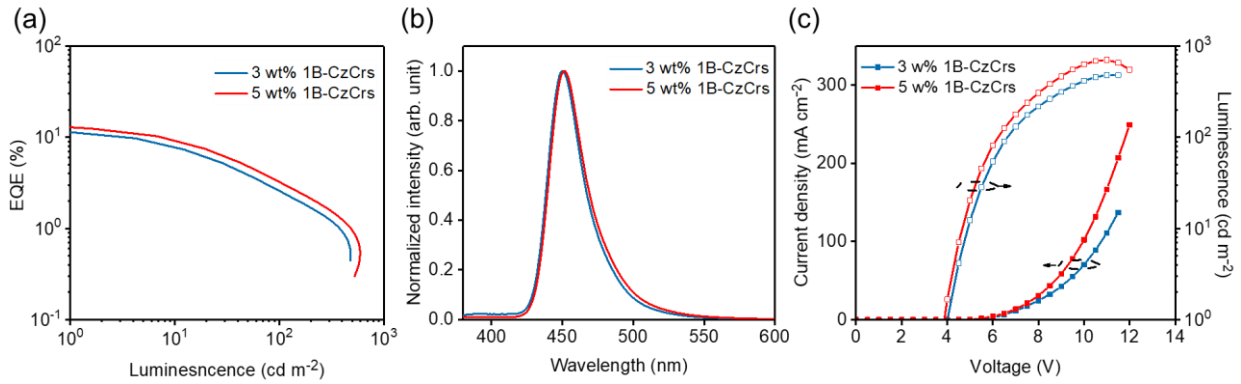

Figure 2-14. Device performance of devices with 3 wt% (blue line) and 5 wt% (red line) **1B-CzCrs** in ***m*CP**. (a) Graph of EQE vs. Luminescence, (b) EL spectra, and (c) Graph of current density (closed circle) and luminance (open circle) vs. driving voltage.

Table 2-10. Device performance of 3 and 5 wt% **1B-CzCrs** in ***m*CP** host.

Emitter	V_{on} (V)	EQE_{max} (%)	λ_{EL} (nm)	FWHM (nm)	Lum_{max} (cd m^{-2})
3 wt% **1B-CzCrs**	4.0	11.4	450	30	487
5 wt% **1B-CzCrs**	3.8	12.8	451	30	688

Compared with previously reported deep-blue MR-TADF emitters, the EQE of the device with 5 wt% **1B-CzCrs** can be considered as a moderate value (EQE_{max} = 12.8%). These EQE_{max} values of **1B-** and **2B-CzCrs** devices compared with those of Φ_{PL} were explained by the dipole orientation of the emitters in the emissive layer, which directly affects the light outcoupling efficiency (η_{OC}) as mentioned in **Chapter 1**. To understand the molecular orientation of both emitters in ***m*CP**, the angle-dependent PL was conducted for the 5 wt% doped **1B-CzCr** and **2B-CzCrs** in ***m*CP** (**Figure 2-15** and **Table 2-11**). The angular-dependent PL properties were simulated using SETFOS software to determine the dipole orientation of the doped films and subsequently to determine the η_{OC}. The experimental data of 5 wt% doped **1B-** and **2B-CzCrs** in ***m*CP** were well fitted with horizontal-dipole ratios of (Θ) = 0.43 and Θ = 0.50, respectively, where the Θ values of 0, 0.33, and 1 correspond to perfectly horizontal, isotropic, and vertical orientation, respectively. The isotropic alignments of both MR emitters in ***m*CP** explain the relatively modest EQE values observed in resulting devices which was further confirmed by the calculation of η_{OC} values, yielding η_{OC} of 17.7 and 15.3% for the devices with **1B-** and **2B-CzCrs**, respectively.[29,44] The theoretical EQE values were determined by **Eq. 6**, by assuming a balanced charge and 100% harvesting of electrically generated excitons (γ = η = 1).[44] The calculated EQE values for the devices incorporating **1B-** and **2B-CzCrs** were 13.3 and 9.5%, respectively, and closely align with the experimental results.

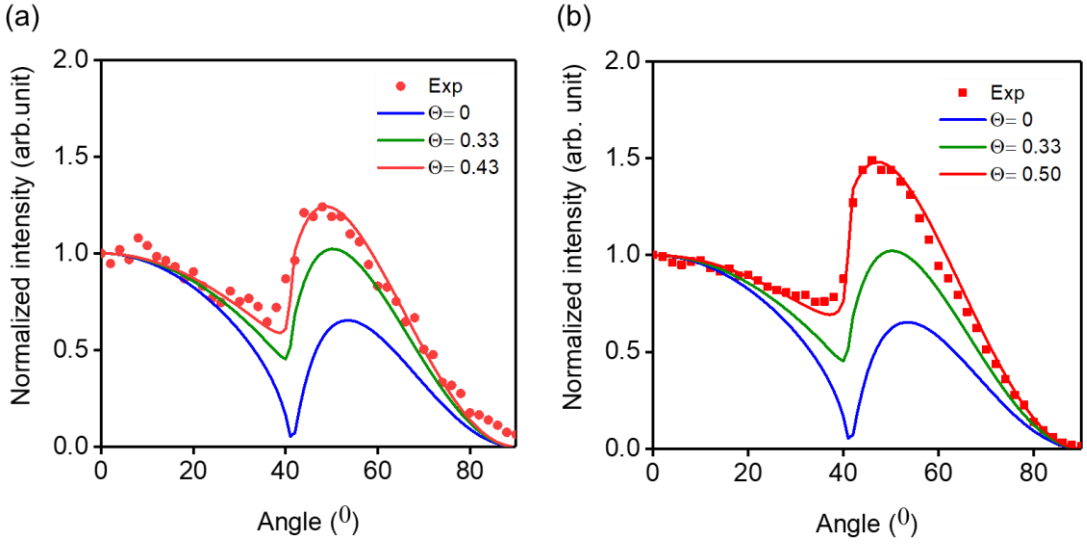

Figure 2-15. Angular-dependent PL profiles of 5 wt% **1B-CzCrs** (a) and **2B-CzCrs** (b) doped in ***m*CP** host. The horizontal (blue line), isotropic (green line), and fitting curves for the experimental data (red line) were provided using the optical simulation software SETFOS 5.1 (Fluxim).

Table 2-11. Orientational order parameter (S), η_{oc}, theoretical and the experimental EQE values of the devices with **1B-** and **2B-CzCrs**.

Emitter	S	η_{oc} (%)	Theoretical EQE_{max} (%)	Experimental EQE_{max} (%)
1B-CzCrs	0.30	17.7	13.3	12.8
2B-CzCrs	0.50	15.3	9.5	8.4

According to the device data with the ***m*CP** host, the CIEy > 0.05 and was not up to the satisfactory of BT.2020 standard. This can be ascribed to the broadened emission of both emitters in the ***m*CP** host matrix.

Since the PL emission showing better CIE coordinates for the **1B-** and **2B-CzCrs** were obtained with the low doping concentration of 1 wt% in the ***m*CBP** host (**Figure 2-8** and **Table 2-5**) in which CIE_y values satisfied BT.2020, respective OLEDs were fabricated with host ***m*CBP**. However, the OLED devices with ***m*CBP** host showed slightly broader emission compared to the PL spectra with CIE_y of 0.048 and 0.049 for **1B-** and **2B-CzCrs**, respectively (**Figure 2-16** and **Table 2-12**). Furthermore, the EQE_{max} of both devices were 8.1 and 7.7 % for **1B-** and **2B-CzCrs**, respectively. The inferior device performance in the ***m*CBP** host can be ascribed to the charge carrier imbalance where the devices with ***m*CPB** show higher turn-on voltage than those with the ***m*CP** host. Nevertheless, the devices with both emitters in the ***m*CBP** host almost satisfied BT.2020 with $CIE_y < 0.05$.

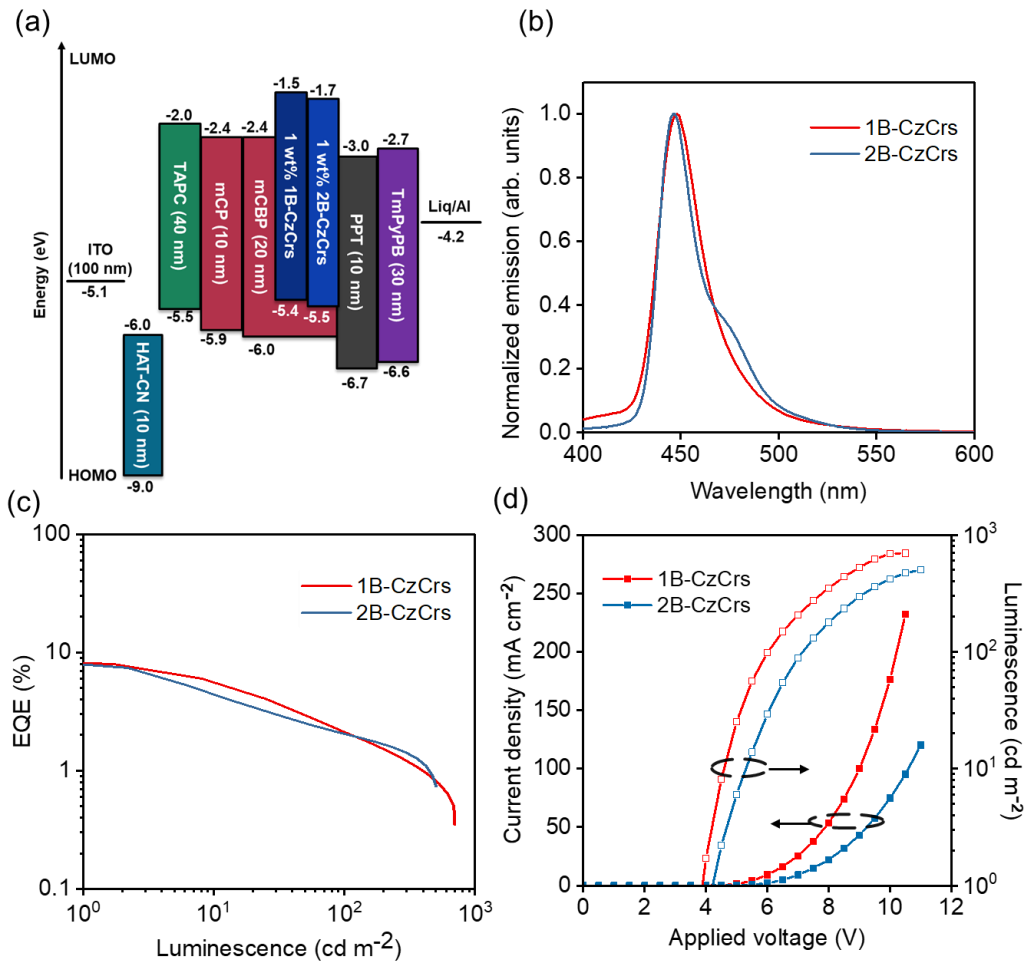

Figure 2-16. Device performance of **1B-**and **2B-CzCrs** with ***m*CBP** host, (a) Device structure, (b) EL spectra of devices, (c) Graph of EQE vs. Luminescence, and (d) Graph of current density (closed circle) and luminance (open circle) vs. driving voltage.

Table 2-12. Device performance of 1 wt% **1B-** and **2B-CzCrs** in ***m*CBP** host.

Emitter	**V_{on} (V)**	**EQE_{max} (%)**	**λ_{EL} (nm)**	**FWHM (nm)**	**Lum_{max} (cd m^{-2})**	**CIE_x**	**CIE_y**
1B-CzCrs	3.9	8.1	448	26	705	0.152	0.048
2B-CzCrs	4.2	7.7	447	22	485	0.150	0.049

2.3. Conclusion

In summary, two deep-blue emitters, **1B-** and **2B-CzCrs**, were successfully synthesized by introducing a carbazole unit to the MR core. Both emitters exhibited high Φ_{PL} values in toluene. **1B-CzCrs** exhibited a small ΔE_{ST} value of 0.16 eV compared to **2B-CzCrs**. Both **1B-** and **2B-CzCrs** emitted a deep-blue color at 451 and 449 nm, respectively, with a narrow FWHM of 28 nm in doped films. Notably, both emitters exhibited TADF properties in doped films. It is worth mentioning that **1B-CzCrs** gained TADF activity by a carbazole induction to the previously reported non-TADF **1B-DTACrs**. Although the carbazole moiety contributed to the expression of the TADF property in the minimum MR core, reduced k_{RISC} was observed in the symmetrical MR structure. The OLED devices having ***m*CP** as the host material demonstrated a high EQE_{max} of 12.8% for **1B-CzCrs**, together with CIE coordinates of (0.146, 0.062). In contrast, the device with **2B-CzCrs** showed a lower EQE_{max} of 8.4% with CIE coordinates of (0.153, 0.143). The devices with ***m*CBP** host achieved CIE_y < 0.05, demonstrating its potential as an emitter for next-generation deep-blue devices.

2.4. Materials and methods

2.4.1. Material synthesis and characterization

1B- and **2B-CzCrs** emitters were synthesized and characterized by Dr. J. M. Dos Santos in Prof. Zysman-Colman's group at St. Andrews university. The detailed synthesis procedures and the characterizations are attached in **Appendix A**.

2.4.2. Photophysical measurements

Optically dilute solutions of emitters were prepared in spectroscopic or HPLC-grade solvents for absorption and emission analysis. Organic thin films for photophysical measurements (except for streak camera measurements) were fabricated on quartz substrates, which were pre-cleaned using acetone and isopropanol followed by 15 min UV treatment (NL-UV253, Nippon Laser & Electronics Lab., Japan) just prior to the film preparation to remove adsorbed organic species before deposition. Thin films for the streak camera measurements were prepared on silicon substrates. All the films were fabricated by vacuum thermal evaporation at a pressure below 10^{-4} Pa. UV-vis absorption spectra were recorded at room temperature using a Lambda 950-PKA spectrophotometer (Perkin-Elmer, USA). 1 cm quartz cuvettes were used for the solutions. Steady-state emission spectra were recorded using an FP-

8600 fluorometer (JASCO, Japan). Phosphorescence measurements were taken at 77 K (delay 115 ms, gate 150 ms). A Quantaurus-QY C11347-01 (Hamamatsu Photonics, Japan) integrating sphere was used to measure the absolute PL quantum yields. The transient photoluminescence decay characteristics were measured with a Quantaurus-Tau C11367-03 (Hamamatsu Photonics, Japan) instrument and a streak camera system (C10910-01, Hamamatsu Photonics, Hamamatsu, Japan) with a third harmonic YAG laser (355 nm, 10 Hz, PL-2250, EKSPLA, Lithuania) as an excitation source. The thicknesses of all the films were measured using Variable-angle spectroscopic ellipsometry with an M-2000U (J.A. Woollam Co. Inc., USA) instrument. The angular-dependent PL properties were simulated using SETFOS 5.1 (Fluxim) software to determine the dipole orientation of the doped films and consequently to determine the light outcoupling efficiency.

2.4.3. Device fabrication and measurement of OLED properties

OLEDs were fabricated on glass substrates coated with a patterned transparent ITO conductive layer (50 nm). ITO glass substrates were cleaned using detergent, followed by de-ionized water, acetone, and isopropanol and dried with isopropanol. Then, they were subjected to the UV treatment for 15 min just prior to the device fabrication. The devices were fabricated by using vacuum deposition under 1.0×10^{-5} Pa. After the fabrication, devices were immediately encapsulated with encapsulation glasses using epoxy glue in a nitrogen-filled glove box ($O_2 < 0.1$ ppm, $H_2O < 0.1$ ppm). The current density-voltage-luminance (*J-V-L*) characteristics of the OLEDs were assessed using a source meter (Keysight B2911A, Keysight Technologies, USA) and a luminance meter (CS-2000, Konica Minolta, Japan) at a constant DC current at room temperature.

Chapter 3

A boron, nitrogen, and oxygen incorporated π-extended helical pure blue MR-TADF emitter having fast k_{RISC}

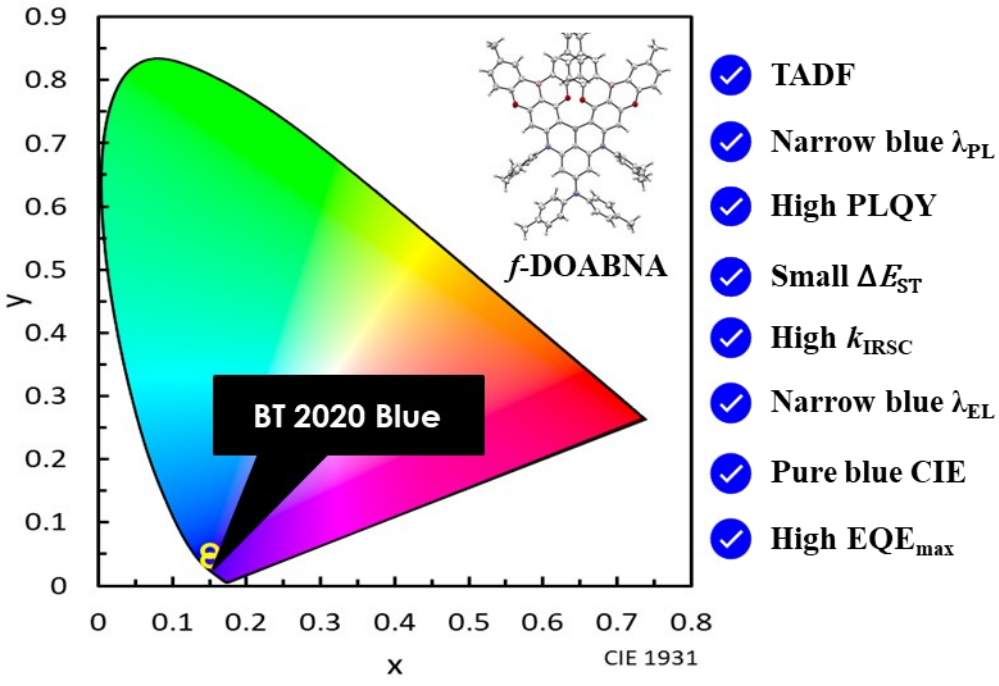

3.1. Introduction and motive of the study

Although I succeeded in developing TADF active deep-blue MR-TADF emitter (**1B-CzCrs** and **2B-CzCrs**) with CIE < 0.05, it did not satisfy the most recent color standard, BT.2020 for blue pixels due to their moderate FWHM values and the device EQE was not up to the satisfactory due to the slow k_{RISC} and moderate SOC values which are more common drawbacks of MR-TADF emitters. Hence, in this chapter, I introduced different design strategies aiming for a deep-blue MR-TADF emitter to satisfy BT.2020, together with high EQE and narrowband emission. As mentioned in **Section 1.5**, In spite of the narrow emission, MR-TADF emitters have slow k_{RISC} values (< 10^5 s^{-1}), due to their moderately large ΔE_{ST}, and low SOC values, which perpetually limit the device performance.[28,65]

Recently, it has been found that a helical π-system of MR-TADF emitter can result in a smaller ΔE_{ST} and a high SOC, hence a higher k_{RISC} and better device performances.[66,67] The synthesis of highly distorted MR-TADF emitter keeps challenging. Hatakeyama et al. reported a π-extended helical MR-TADF, **V-DABNA-Mes** (**Figure 3-1a**), with a smaller ΔE_{ST} of 5.2 meV, shorter delayed lifetime (τ_d) of 2.39 μs, and a k_{RISC} of 4.4 × 10^5 s^{-1} in doped films which showed highly efficient (EQE_{max} = 22.9%) sky-blue emission at 480 nm in solution-processed OLEDs with at CIE coordinates of (0.09, 0.21).[66] By replacing the peripheral mesityl units of **V-DABNA-Mes** with phenyl groups, the same group developed a new emitter, **V-DABNA** (**Figure 3-1b**), which showed similar photophysical and OLED properties to that of **V-DABNA-Mes**. The device showed EQE_{max} of 26.2% with λ_{PL} of 483 nm, FWHM of 17 nm, and CIE coordinates of (0.09, 0.25).[67] Notably, the derivative **V-DABNA-F** (**Figure 3-1c**) based OLED showed an EQE_{max} of 26.6% at λ_{EL} of 468 nm and CIE coordinates of (0.12, 0.10). These works emphasize the helical designs demonstrating improved k_{RISC} to > 10^5 s^{-1}. Nevertheless, it is also clear that the difficulty of achieving the desired color standard, BT.2020, for blue pixels with those emitters due to their redshifted emission by π-conjugated systems. Several studies suggested that, properly arranging nitrogen and oxygen donor atoms with boron acceptors can blueshift the emission with the aid of oxygen donor, while it resulted in rather large ΔE_{ST} and slow k_{RISC} values.[43,68,69] For examples, in 2022, Suresh et al. reported a deep blue nonacene, **NOBNacene** in which the 1.5 wt% doped **NOBNacene** in **TSPO1** exhibited λ_{PL} at 410 nm with a ΔE_{ST} of 0.30 eV and k_{RISC} of 3.74 × 10^3 s^{-1}.[68] In 2023, the same group reported the MR-emitter, **DIDOBNA-N**, in which the 1.5 wt% doped MR-emitter in **TSPO1** exhibited λ_{PL} at 444 nm with a ΔE_{ST} of 0.23 eV and k_{RISC} of 3.14 × 10^4 s^{-1}.[69]

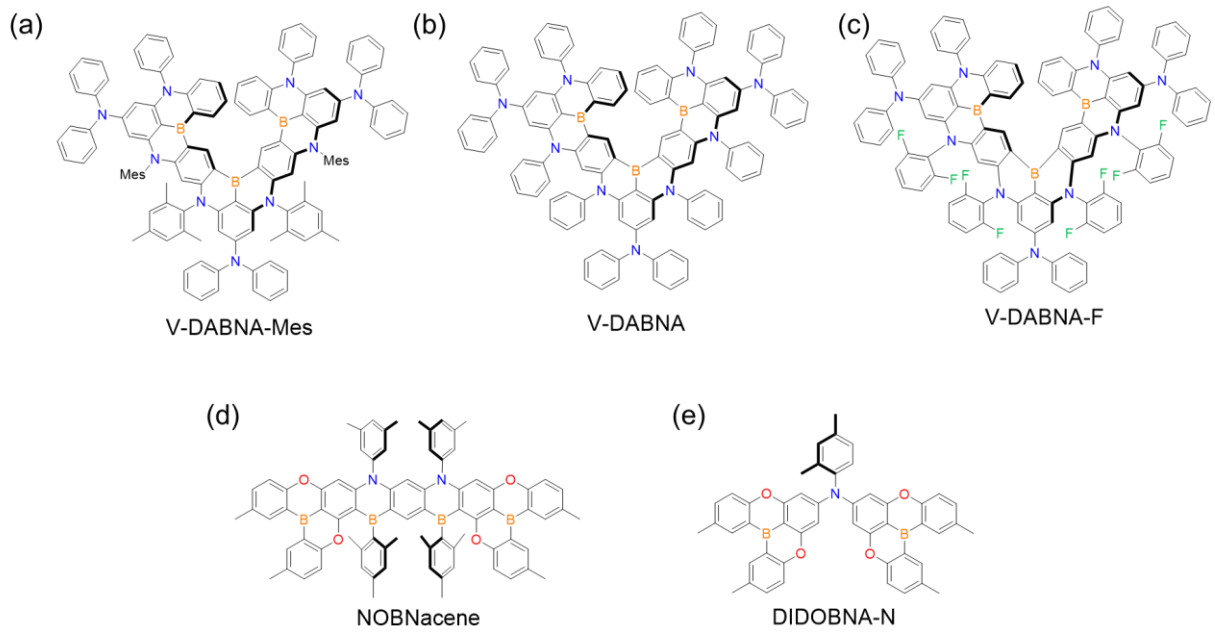

Figure 3-1. Structures of MR-TADF emitters describe in **Section 3.1.** (a) **V-DABNA-Mes**, (b) **V-DABNA** and, (c) **V-DABNA-F**, (d) **NOBNacene**, and (e) **DIDOBNA-N**.

Therefore, developing pure blue narrowband emitters that are efficient triplet harvesters and proper device engineering to achieve blue OLEDs satisfying BT.2020 simultaneously achieving narrowband emission and high EQE is still an important concern for the OLED industry.

This study synthesized and characterized a helical MR-TADF emitter, ***f*-DOABNA**, aiming to enhance k_{RISC} with deep blue emission. In toluene, ***f*-DOABNA** not only exhibited narrowband emission (18 nm), but also demonstrated a remarkably high k_{RISC} (1.0×10^6 s^{-1}) and a short delay lifetime (1.93 μs). Deep-blue OLEDs have been fabricated by employing ***f*-DOABNA** as a dopant, which exhibited a maximum EQE of ~ 20%. Most importantly, the ***f*-DOABNA**-based OLED device with ***m*CP** as host satisfied the requirement of BT.2020 standard for the blue pixel (0.131, 0.046) while achieving nearly 20% EQE and narrowband emission (< 25 nm), indicating the potential application of ***f*-DOABNA** in the display industry.

3.2. Results and discussion

3.2.1. Molecular design

Since the first reported MR emitter, **DABNA 1** (**Figure 3-2a**), **DABNA**-based emitters have shown narrower FWHM and better performances with an extended **DABNA** core.[28] However, most of the **DABNA**-based molecules show redshifted emission. On the other hand, the B/O embedded **DOBNA** core (**Figure 3-2b**) can exhibit blueshifted emission; however, a very high energy emission below 400 nm which is undesirable.[70] In this study, helical ***f*-DOABNA** was synthesized by fusing two **DOBNA** cores to a **DABNA** core, aiming for enhanced k_{RISC} with deep blue emission in the 440-455 nm region.

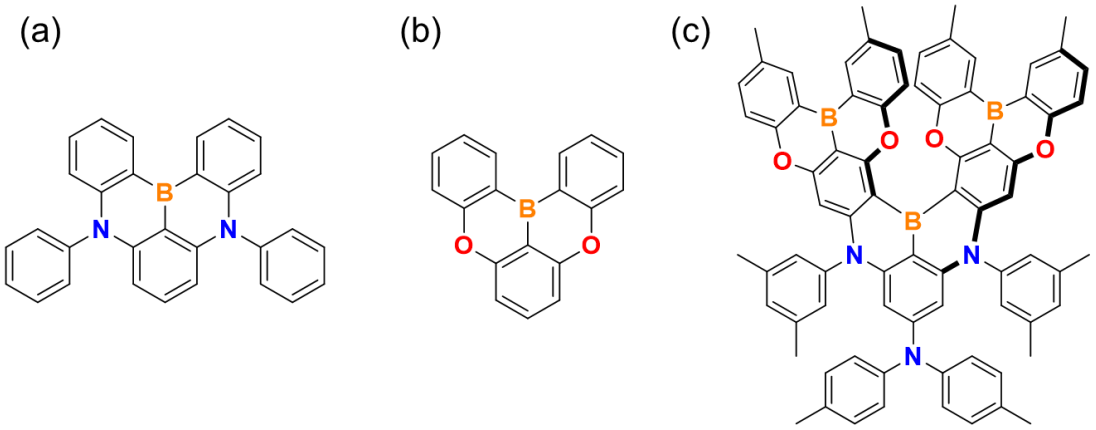

Figure 3-2. Chemical structures of (a) **DABNA 1**, (b) **DOBNA**, and (c) ***f*-DOABNA**.

3.2.2. Theoretical calculations

The ground state optimizations were carried out using the DFT with the PBE0 functional and the 6-31G(d,p) basis set in the gas, whereas the excited state optimizations were carried out using the time-dependent within the TDA-DFT with the same functional and the basis in the gas phase. Excited states' excitation energies were modeled with the SCS-CC2 method using a cc-pVDZ basis set, based on the ground and excited state geometries calculated by DFT and TDA-DFT, respectively (**Figure 3-3**). Above calculations were performed by Zyzman-Colman group at St Andrews University, UK.

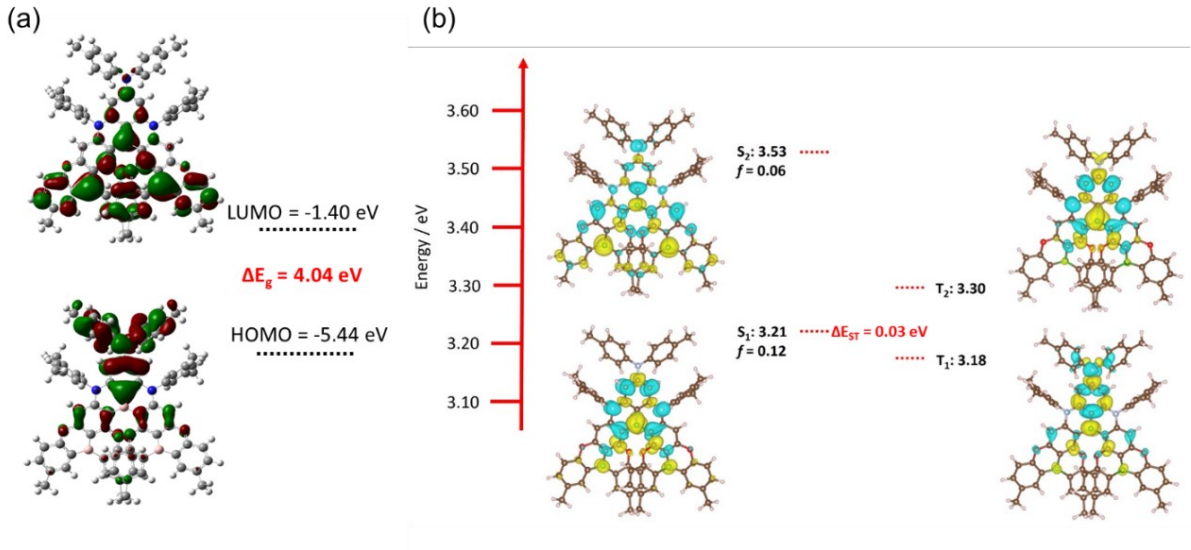

Figure 3-3. (a) HOMO/LUMO energies and electron density distributions of the ground-state geometry of ***f*-DOABNA** in the gas phase and (b) Excited-state energies and difference density plots of S_1, S_2, T_1, and T_2 calculated of ***f*-DOABNA**.

According to the HOMO/LUMO energies distribution of ***f*-DOABNA** in ground state geometry, the HOMO is mainly localized on the diphenylamine (DPA) unit with strong electron donating ability and the phenyl connected to the DPA unit, and the LUMO is mainly localized on the DOBNA cores with weak donating ability. Therefore, ***f*-DOABNA** exhibited a mixture of SRCT and LRCT characters which are a deviated trend from the typical MR-TADF emitters commonly having SRCT characteristics. At the DFT level, the calculated HOMO and LUMO were −5.44 and −1.40 eV, respectively, giving an energy gap of 4.04 eV, promising for deep-blue emission. The SRCT characteristics, typically inherent by MR-TADF emitters, were also indicated in ***f*-DOABNA** by the difference density plot of the S_1 excited state, which displayed an alternating pattern of increasing and decreasing electron density akin to MR-TADF emitters. Notably, the nature of the T_1 excited state significantly diverges from the nature of the S_1 state, similar to an LE excited state, with density delocalized to the DPA unit. Due to this different nature of T_1 and S_1 excited states, the SOC constant between T_1 and S_1 was obtained at 0.44 cm^{-1}, surpassing that of most MR-TADF compounds, facilitating a notably accelerated k_{RISC}. In addition, calculations anticipate a closely lying T_2 state with non-negligible SOC to S_1 (0.01 cm^{-1}), suggesting the contribution of T_2 for an accelerated k_{RISC}. The S_1 and T_1 energies, calculated at the SCS-CC2, were 3.21 and 3.18 eV, respectively, resulting in a significantly smaller ΔE_{ST} of 0.03 eV, which would facilitate the fast RISC process which is discussed in **Section 3.2.3**.

3.2.3. Photophysical studies

The photophysical properties of ***f*-DOABNA** were studied in diluted solutions and in doped films with different host materials. The solution state photophysics was measured in toluene (1.0×10^{-5} mol L^{-1}). The absorption and emission spectra of solution state ***f*-DOABNA** are shown **in Figure 3-4**, and the data are summarized in **Table 3-1**. the absorption spectrum of ***f*-DOABNA** in toluene exhibited a strong absorption band with $\varepsilon = 9.58 \times 10^4$ L mol^{-1} cm^{-1} at 369 nm corresponding to the π to π* and a weak band with $\varepsilon = 2.49 \times 10^4$ L mol^{-1} cm^{-1} at 428 nm, corresponding to the SRCT transitions. The steady-state emission of ***f*-DOABNA** showed deep blue with emission maxima at 442 nm as predicted by the DFT calculations and an excellent narrowband emission with FWHM of 18 nm. Compared with the previously reported π-conjugated helical MR-emitters, **V-DABNA-Mes** (486 nm), **V-DABNA** (483 nm), and **V-DABNA-F** (467 nm) (**Figure 2.1**), the emission of ***f*-DOABNA** has largely blueshifted due to the **DOBNA** core with oxygen, having weak electron-donating ability than nitrogen.[67] Sharp narrowband emission can be ascribed to the suppression of the stretching and scissoring vibrations and the vibronic coupling between S_1 and S_0 states due to the nonbonding nature of HOMO and LUMO in ***f*-DOABNA**.

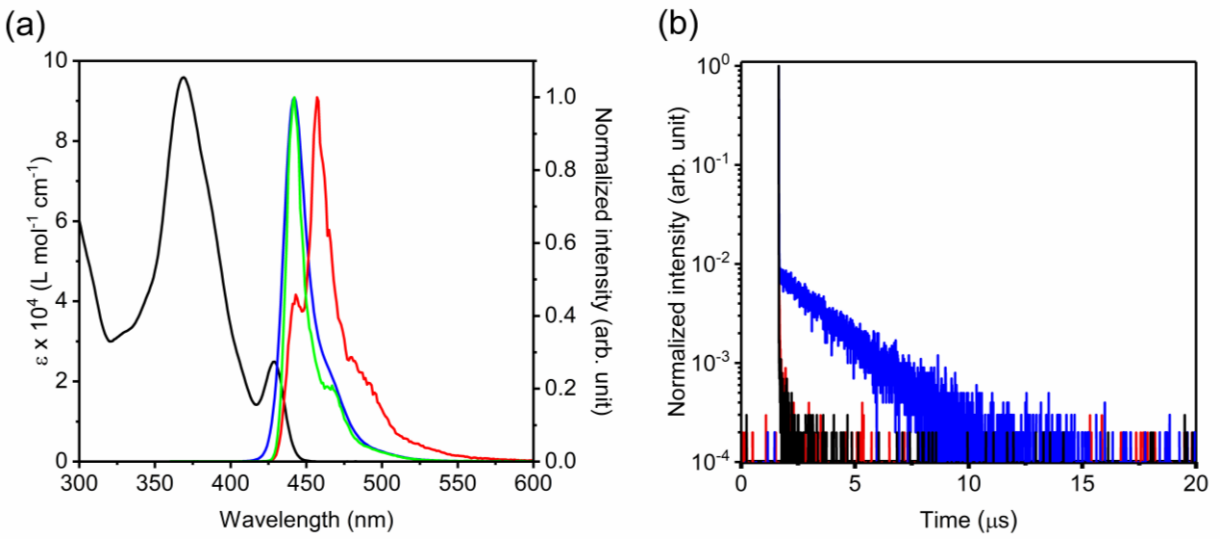

Figure 3-4. (a) Absorption (black line), steady-state PL at RT (blue line, λ_{exc} = 340 nm), steady-state PL at 77 K (green line) and phosphorescence spectra at 77 K (red line, delay 270 ms, gate 20 ms) of ***f*-DOABNA** in toluene (1.0×10^{-5} mol L^{-1}) and (b) Time-resolved emission decays at 300 K (λ_{exc} = 340 nm) under Ar saturated (blue line), aerated conditions (red line), and IRF (black line).

Table 3-1. Steady-state photophysical properties of ***f*-DOABNA** in toluene.

	Φ_{PL}[a] (%)	Φ_{PL}[b] (%)	λ_{PL}[c] (nm)	FWHM (nm)	E_{S1}[d] (eV)	E_{T1}[d] (eV)	ΔE_{ST} (eV)
***f*-DOABNA in Toluene**	46	93	442	18	2.88	2.80	0.08

[a] Absolute Φ_{PL} of thin films measured using an integrating sphere under aerated condition. [b] Absolute Φ_{PL} of thin films measured using an integrating sphere under Ar saturated condition. [c] fluorescence maximum at RT. λ_{exc} = 340 nm in toluene and λ_{exc} = 310 nm for doped films. [d] S_1 and T_1 energies determined from the onset of the total emission and phosphorescence spectra at 77 K, respectively.

The phosphorescence spectrum of ***f*-DOABNA** at 77 K exhibited two emission peaks around 443 nm and 457 nm. The first emission peak around 443 nm coincided with the fluorescence spectrum of ***f*-DOABNA** at 77 K, indicating that it originated from the fluorescence. This was confirmed by the observed decrease in the intensity of the first peak as the delay time increased (**Figure 3-5a**). The S_1, T_1, and the ΔE_{ST} values for ***f*-DOABNA** in toluene were estimated from the onset of fluorescence and phosphorescence spectra at 77 K, applying Jacobian conversion (**Figure 3-5b**).[60] The calculated S_1 and T_1 energies were 2.88 and 2.80 eV, respectively, resulting in a ΔE_{ST} of 0.08 eV, only a slightly larger value than the estimated ΔE_{ST} from SCS-CC2/cc-pVDZ calculations.

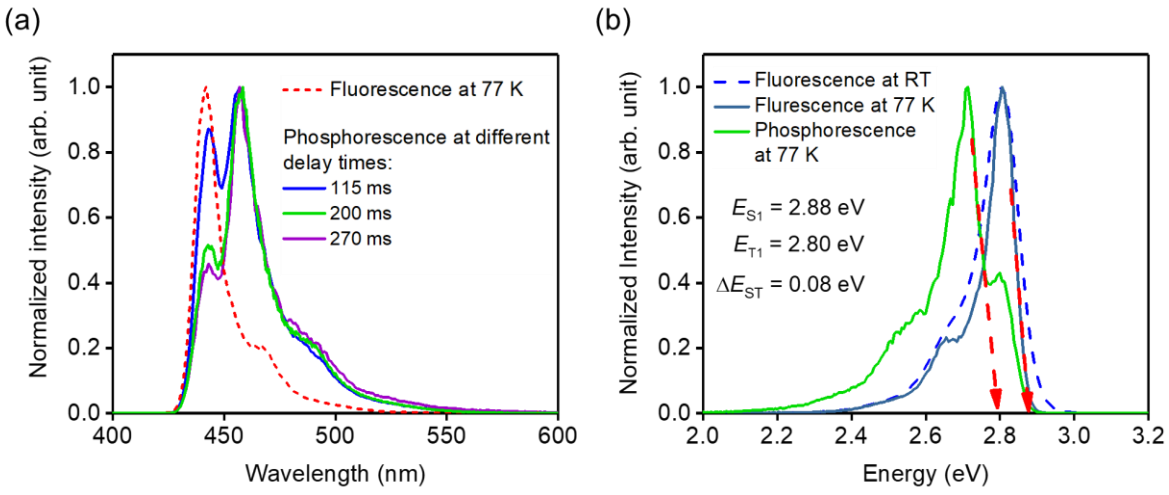

Figure 3-5. (a) Steady-state fluorescence and delayed emission (77 K) spectra of ***f*-DOABNA** in toluene; phosphorescence spectra were measured at different delay times to start emission integration after closing shutter for excitation light and (b) Steady-state emission profiles in energy scale (λ_{exc} = 340 nm).

In an aerated toluene solution, ***f*-DOABNA** exhibited a PLQY of 46%, which was drastically increased to 93% in an Ar-saturated toluene solution, suggesting a substantial contribution of triplets in the light emission process. Furthermore, the high PLQY of ***f*-DOABNA** indicates limited nonradiative decay even in solution conditions, where molecular vibrations and solute-solvent interactions often lead to increased nonradiative decay.

Then, I measured the transient decay profiles of ***f*-DOABNA** in toluene (**Figure 3-4b**). In aerated conditions, only the prompt component was observed in the PL decay, with a τ_p of 2.99 ns. On the other hand, under Ar saturated conditions, ***f*-DOABNA** exhibited a two-component decay profile (both prompt and delay) with lifetimes of 3.34 ns and 1.93 μs for τ_p and τ_d, respectively. A previously reported method by our group was used to estimate the rate constants for the transient decay of ***f*-DOABNA**.[62] The calculated values of k_r, k_{nr}, k_{ISC}, k_{RISC}, and the potential range for the rate constants k_{ISC}, and k_{RISC} considering the limiting conditions $k_{nr}^{T} = 0$ and $k_{nr}^{S} = 0$ are shown in **Table 3-2**. [62] According to the calculations, a large k_r of 1.05×10^8 s^{-1} and a relatively small k_{nr} of 7.92×10^6 s^{-1} were obtained for ***f*-DOABNA**, resulting in a significantly high k_r to k_{nr} ratio of 13.26. This is reflected in the high Φ_{PL} obtained for ***f*-DOABNA** in toluene. Outstandingly, ***f*-DOABNA** possessed an extremely fast k_{RISC} of 1.01×10^6 s^{-1} in toluene, one of the fastest values amongst previously reported MR-TADF molecules. It is worth noting that this fast k_{RISC} was obtained without the incorporation of heavy atoms.[28,65]

Table 3-2. Transient decay data and estimated rate constants for ***f*-DOABNA** in toluene.

	τ_p[a] (ns)	τ_d[a] (μs)	k_r[b] (10^8 s^{-1})	k_{ISC}[b] (10^8 s^{-1})	k_{RISC}[b] (10^6 s^{-1})	k_{nr}[b] (10^7 s^{-1})	Avg. k_{ISC} (10^8 s^{-1})	Avg. k_{RISC} (10^6 s^{-1})
***f*-DOABNA in Toluene**	3.34	1.93	1.05	1.08	1.02	0.79	1.13 ± 0.04	0.98 ± 0.03

[a] Prompt and delayed lifetimes obtained under Ar-saturated conditions. [b] Rate constants were calculated using three-state model approximating no phosphorescence in emission.[62]

This exceptionally fast k_{RISC} can be explained by the combination effect of small ΔE_{ST} and large SOC between S_1 and T_1 states observed in ***f*-DOABNA**. As predicted, the π-conjugated helical molecular design of ***f*-DOABNA** allows the delocalization of molecular orbitals via the π-extension, leading to a small ΔE_{ST}. It is worth to mentioning that, unlike

previously reported helical MR-TADF emitters (without oxygen), this small ΔE_{ST} was achieved without compromising color purity due to the emission control using B, N, O hetero atoms. Furthermore, as described in **Section 1.3**, the spatial separation of HOMO and LUMO is favorable for achieving a small ΔE_{ST}. Unlike typical MR-TADF emitters which show moderate ΔE_{ST} values due to SRCT characteristics, as indicated by theoretical calculations ***f*-DOABNA** showed mixed LRCT and SRCT characteristics with spatially separating HOMO and LUMO. This tendency may further contribute to the small ΔE_{ST} observed in ***f*-DOABNA**. In contrast to the majority of MR-TADF compounds in which the nature of S_1 and T_1 are identical, the dissimilar nature of the S_1 and T_1 states in ***f*-DOABNA** having significantly high SOC between S_1 and T_1 may also aid in accelerating the RISC process.[71]

Next, to study the effect of the solvent polarity on ***f*-DOABNA**, the emission profiles of ***f*-DOABNA** in solvents with different polarities were recorded. As changing the solvent polarity from non-polar toluene to polar acetonitrile, the PLQY was decreased and a weak positive solvatochromatic effect (13.7 nm) on ***f*-DOABNA** was observed, confirming the SRCT nature of ***f*-DOABNA** (**Figure 3-6** and **Table 3-3**). Although the solvatochromatic effect in ***f*-DOABNA** was weaker compared to the D-A type TADF emitters with CT characteristics, it was slightly larger than that of previously reported boron-based MR-TADF emitters.[28] This again confirms that ***f*-DOBNA** has LRCT character while maintaining the MR nature.

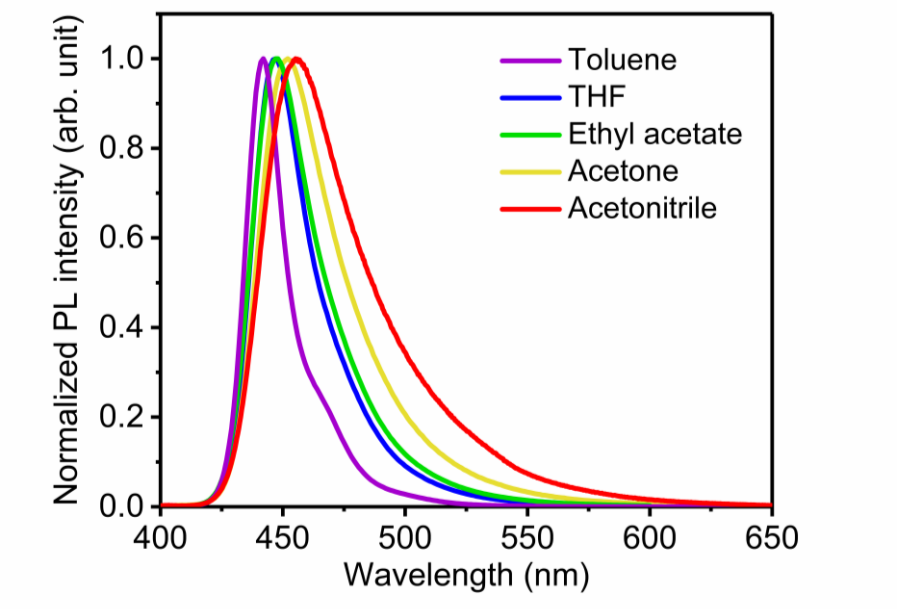

Figure 3-6. Steady-state photoluminescence spectra of ***f*-DOABNA** in different solvents (λ_{exc} = 340 nm).

Table 3-3. Photophysical properties of ***f*-DOABNA** in different solvents.

Solvent	λ_{PL}[a] (nm)	FWHM (nm)	Φ_{PL}[b] (%)
Toluene	442	18	93.4
THF	447	28	94.2
Ethyl acetate	447	32	90.8
Acetone	452	38	86.8
Acetonitrile	456	47	74.9

[a] Fluorescence maximum at RT. λ_{exc} = 340 nm. [b] Absolute Φ_{PL} of thin films measured using an integrating sphere under Ar saturated condition.

Then, the film state photophysics of ***f*-DOABNA** was investigated in a 1 wt% doped in three different host materials, bis[2-(diphenylphosphino)phenyl]ether oxide (**DPEPO**), ***m*CP**, and 3,11-di-*o*-tolyl-5,9-dioxa-13b-boranaphtho[3,2,1-de]anthracene (**DOBNA-Tol**) (**Figure 3-7**). The steady state and transient decay data are depicted in **Figure 3-8** and **Table 3-4**. The 1 wt% doped ***f*-DOABNA** in all three hosts exhibited high Φ_{PL} values, ranging from 69-90%. All doped films, however, displayed slightly redshifted and broadened emission spectra than those in toluene, even at 1 wt% doping concentration.

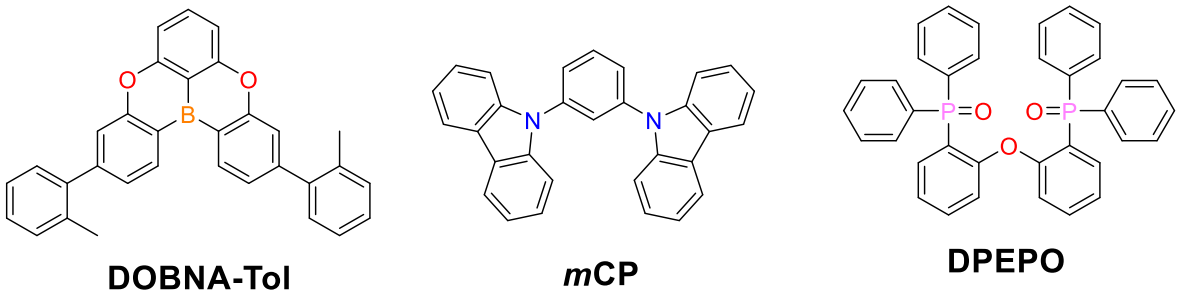

Figure 3-7. Molecular structures of the host materials used in this study.

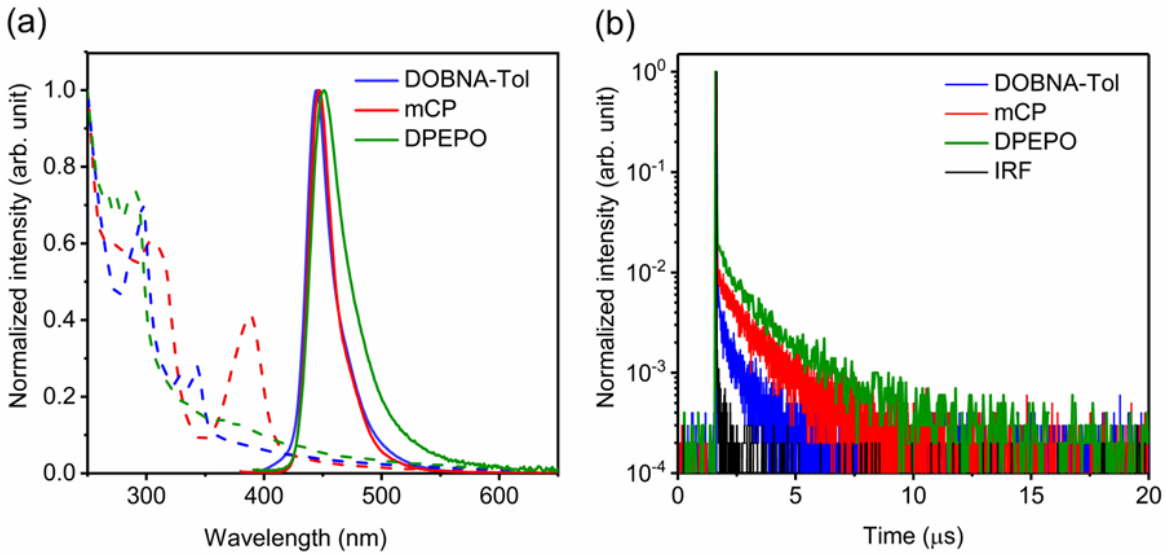

Figure 3-8. Photophysical properties of 1 wt% of ***f*-DOABNA** doped in different hosts: (a) normalized absorption (dotted lines), and fluorescence (solid lines, λ_{exc} = 310 nm) spectra and (b) Transient decay curves (λ_{exc} = 280 nm) under the degassed conditions for hosts **DOBNA-Tol**, ***m*CP**, and **DPEPO** and the IRF (black line) at 300 K.

Table 3-4. Film-state photophysical properties of 1 wt% doped ***f*-DOABNA** in different hosts.

	Φ_{PL}[a] (%)	λ_{PL}[b] (nm)	FWHM (nm)	τ_p[c] (ns)	τ_d[c] (μs)	k_r[d] (10^8 s^{-1})	k_{ISC}[d] (10^8 s^{-1})	k_{RISC}[d] (10^6 s^{-1})	k_{nr}[d] (10^7 s^{-1})	Avg. k_{ISC} (10^8 s^{-1})	Avg. k_{RISC} (10^6 s^{-1})
DOBNA-Tol	90	444	25	6.20	0.50	1.21	0.28	2.30	1.50	0.36 ± 0.08	1.90 ± 0.39
***m*CP**	80	447	24	3.67	1.22	1.11	1.13	1.41	3.28	1.34 ± 0.17	1.26 ± 0.15
DPEPO	69	450	32	3.04	1.47	1.51	1.09	1.02	6.77	1.44 ± 0.34	0.83 ± 0.19

[a] Absolute Φ_{PL} of thin films measured using an integrating sphere under Ar saturated condition. [b] fluorescence maximum at RT. λ_{exc} = 340 nm in toluene and λ_{exc} = 310 nm for doped films. [c] Prompt and delayed lifetimes obtained under Ar-saturated conditions. [d] Rate constants were calculated using three-state model approximating no phosphorescence in emission.

This broadened redshifted emission can be ascribed to the concentration quenching or/and the effect of the host polarity on the emission profile of ***f*-DOABNA** in doped films.

When considering the ***f*-DOABNA** in **DPEPO**, there was evidence of molecular aggregation even at 1 wt% doping level (FWHM of 32 nm). This was confirmed by the narrower emission (FWHM of 30 nm) at the lower doping level (0.5 wt%) of ***f*-DOABNA** in **DPEPO** and the FWHM rising with increasing doping concentration (**Figure 3-9c** and **Table 3-5**). Nevertheless, the imperfect energy transfer resulted decline in a Φ_{PL} to 48% in the 0.5 wt% ***f*-DOABNA** in **DPEPO** film. However, when considering the trend obtained in solvatochromism studies in solution state, the effect of host polarity on ***f*-DOABNA** doped in **DPEPO** cannot be neglected. Compared to the ***m*CP** and **DOBNA-Tol** with dipole moments of 1.35 and 1.51 D respectively, **DPEPO** has the biggest dipole moment of 5.5 D.[29] Hence, the most pronounced red shift of 9 nm with FWHM of 32 nm was observed for the ***f*-DOABNA** in **DPEPO** and the FWHM was 30 nm even at 0.5 wt%. The PL of the 0.5 wt% ***f*-DOABNA** in ***m*CP** film matched that of 1 wt% doped film and hence, the aggregated emission was not observed at 1 wt% doping level compared. However, the 2 wt% doped ***f*-DOABNA** in ***m*CP** film showed a shoulder at around 500 nm, which can be ascribed to the aggregate emission (**Figure 3-9a** and **Table 3-5**).

1 wt% doped ***f*-DOABNA** in **DOBNA-Tol** exhibited the best photophysical properties, with the most blue-shifted emission of (444 nm) and the highest Φ_{PL}. However, the 2 wt% doped ***f*-DOABNA** in **DOBNA-Tol** film showed broadened emission with reduced Φ_{PL}, which can be ascribed to the aggregate emission (**Figure 3-9b** and **Table 3-5**). ***f*-DOABNA** in **DOBNA-Tol** at a lower doping level (0.5 wt%) also exhibits a broadened emission with reduced PLQY. When the doping concentration of ***f*-DOABNA** in **DOBNA-Tol** is increased to 1 wt%, the emission spectrum is narrower. Given the emission spectrum of **DOBNA-Tol** neat film (**Figure 3-10b**), there might be an incomplete energy transfer from host to emitter, leading to broadened emission at 0.5 wt%. Although the emission spectrum of **DOBNA-Tol** in toluene significantly overlapped with the absorbance spectra of ***f*-DOABNA** in toluene (**Figure 3-10a**), the emission of **DOBNA-Tol** neat film showed a redshifted emission around 400-550 nm, covering the emission of ***f*-DOABNA**. Consequently, the overlap between the emission spectrum of **DOBNA-Tol** neat film and the absorbance spectra of ***f*-DOABNA** neat film is less compared to the results obtained in the solution state (**Figure 3-10b**). Nonetheless, as reflected by the narrower emission of 1 wt% ***f*-DOABNA** in **DOBNA-Tol**, we can suggest that at 1 wt%, sufficient energy transfer occurred between **DOBNA-Tol** and ***f*-DOABNA**.

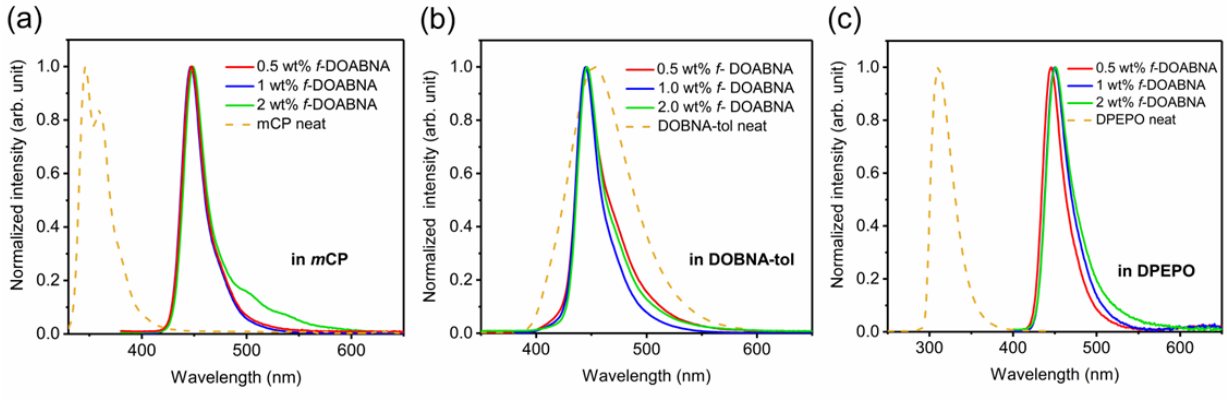

Figure 3-9. Fluorescence spectra of ***f*-DOABNA** doped (a) ***m*CP**, (b) **DOBNA-Tol**, and (c) **DPEPO** films at the various concentrations (λ_{exc} = 310 nm).

Table 3-5. Photophysical properties of ***f*-DOABNA** in doped films in **DPEPO**, ***m*CP**, and **DOBNA-Tol** at various concentrations.

	DPEPO			***m*CP**			**DOBNA-Tol**		
wt% of *f*-DOABNA	**λ_{PL} (nm)**	**FWHM (nm)**	**Φ_{PL} (%)**	**λ_{PL} (nm)**	**FWHM (nm)**	**Φ_{PL} (%)**	**λ_{PL} (nm)**	**FWHM (nm)**	**Φ_{PL} (%)**
0.5 wt%	445	30	54	447	24	51	444	31	47
1 wt%	450	32	69	447	24	80	444	25	90
2 wt%	452	36	48	449	32	56	445	28	51

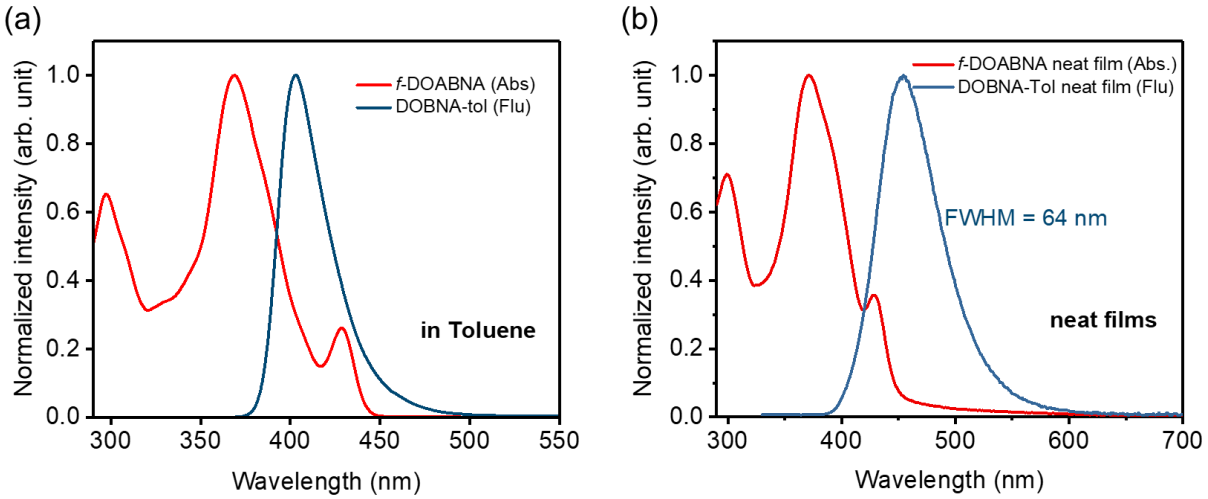

Figure 3-10. Absorbance spectra of ***f*-DOABNA** (red lines) and fluorescence spectra of **DOBNA-Tol** (blue lines) in (a) toluene and (b) neat films.

Notably, when compared to the previously reported MR-TADF emitters, ***f*-DOABNA** in **DOBNA-Tol** showed a remarkably short delayed lifetime of 0.5 μs, due to its high k_{RISC} rate of 2.3 × 10^6 s^{-1}. The delayed lifetimes of 1 wt% doped ***f*-DOABNA** in ***m*CP** (1.22 μs) and **DPEPO** (1.47 μs) hosts were slightly longer compared to ***f*-DOABNA** in the **DOBNA-Tol**, yet persisted very short compared to most other MR-TADF emitters. For further understanding, I examined the temperature dependency of 1 wt% ***f*-DOABNA** in the most promising **DOBNA-Tol** and ***m*CP** hosts. The TADF property of ***f*-DOABNA** in both hosts increased by shortening the delayed lifetime as the temperature rose from 150 K to 300 K, reinforcing the TADF properties (**Figure 3-11**).

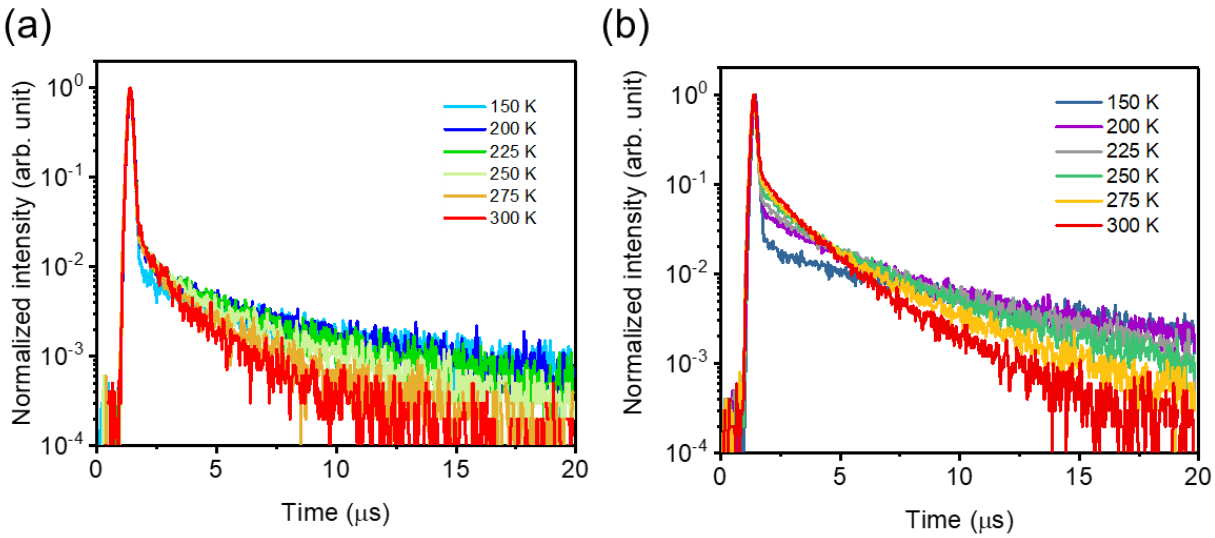

Figure 3-11. Temperature-dependent time-resolved PL decay curves of 1 wt% ***f*-DOABNA** in (a) **DOBNA-Tol** and (b) ***m*CP** hosts.

Based on the temperature dependence data, Marcus plot was exploited to determine the activation energies for ISC (E_a^{ISC})and RISC (E_a^{RISC}) processes, and thereby to estimate the ΔE_{ST}, values for the 1 wt% ***f*-DOABNA** in most promising hosts, **DOBNA-Tol** and ***m*CP** (**Figure 3-12** and **Table 3-6**). The estimated ΔE_{ST} and E_a^{RISC} values for 1 wt% ***f*-DOABNA** in ***m*CP** were 58.9, and 30.9 meV, respectively, whereas both ΔE_{ST} and E_a^{RISC} values for the 1 wt% ***f*-DOABNA** in **DOBNA-Tol** were lower (ΔE_{ST} = 19.7 meV and E_a^{RISC} = 42.9 meV) compared to those for the 1 wt% ***f*-DOABNA** in ***m*CP**. This nearly zero ΔE_{ST} and smaller E_a^{RISC} can be a possible reason for the faster k_{RISC} and shorter delayed lifetime observed in **DOBNA-Tol**

compared to the ***f*-DOABNA** in ***m*CP**. However, further study is needed to determine the exact mechanisms for the fastest k_{RISC} in **DOBNA-Tol**.

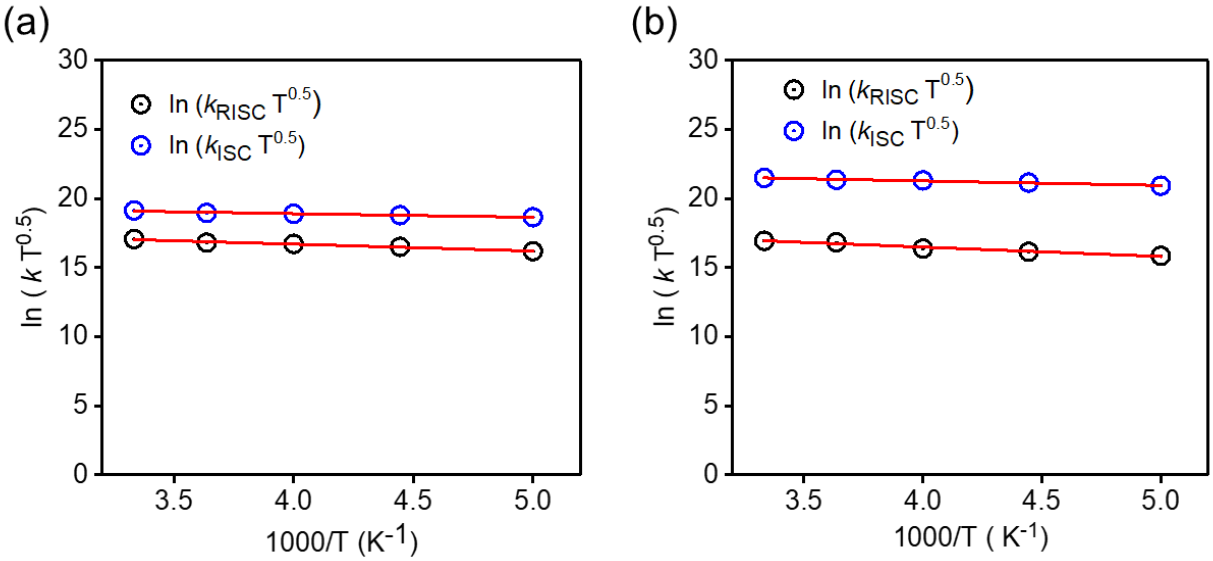

Figure 3-12. Marcus plots (at k_{nr}^{T} = 0) for 1 wt% ***f*-DOABNA** in (a) **DOBNA-Tol** and (b) ***m*CP** hosts.

Table 3-6. Results of Marcus plot analysis for 1 wt% ***f*-DOABNA** in **DOBNA-Tol** and ***m*CP** hosts.

Host	E_a^{ISC} (meV)	E_a^{RISC} (meV)	ΔE_{ST} (meV)
DOBNA-Tol	23.2	42.9	19.7
mCP	28.0	58.9	30.9

3.2.4. OLED device performance

After realizing the excellent photophysical properties of ***f*-DOABNA**, OLEDs were fabricated by vacuum deposition to examine the EL characteristics. Devices with the following structure gave the best performances based on efficiency and color purity: indium-tin-oxide (**ITO**)-coated glass/**TAPC** (55 nm)/***m*CP** (15 nm)/1 wt% ***f*-DOABNA** in **DOBNA-Tol** or ***m*CP** (30 nm)/**PPT** (10 nm)/**BPy-TP2** (30 nm)/ **Liq** (2 nm)/ Al (100 nm), where, **TAPC**, ***m*CP**, ***f*-DOABNA** in **DOBNA-Tol**, **PPT**, **BPy-TP2**, and **Liq** are the hole-transporting, electron-blocking, emitting, hole-blocking, electron-transporting, and electron injection layers, respectively. The device structure and device properties are shown in **Figure 3-13** and **Table 3-7**. Both **DOBNA-Tol**-based and ***m*CP**-based devices showed high EQE_{max} values of nearly

20%, together with narrowband deep blue emissions. The high EQE_{max} values of both devices can be ascribed to the high Φ_{PL} and fast k_{RISC} values observed in ***f*-DOABNA**. The device with **DOBNA-Tol** host showed a lower turn-on voltage of 4.2 V, compared to that of the device with ***m*CP** host (5.0 V) due to the smaller energy barrier for electron injection owing to the lower LUMO level of **DOBNA-Tol** compared to that of ***m*CP**. The EL from both the **DOBNA-Tol** and ***m*CP**-based devices occurred at λ_{EL} of 445 nm, which were in close alignment with the PL spectra of ***f*-DOABNA**. Importantly, the EL of the device with the ***m*CP** host demonstrated the intended blue emission, meeting the requirement of BT.2020 for blue pixels, with a CIE_y of 0.041 owing to its narrower emission (FWHM = 24 nm) EL spectrum. However, the device with the **DOBNA-Tol** host showed a slightly increased CIE_y value (0.051) due to its broadened emission towards the green region of the visible spectrum compared to the device with the ***m*CP** host.

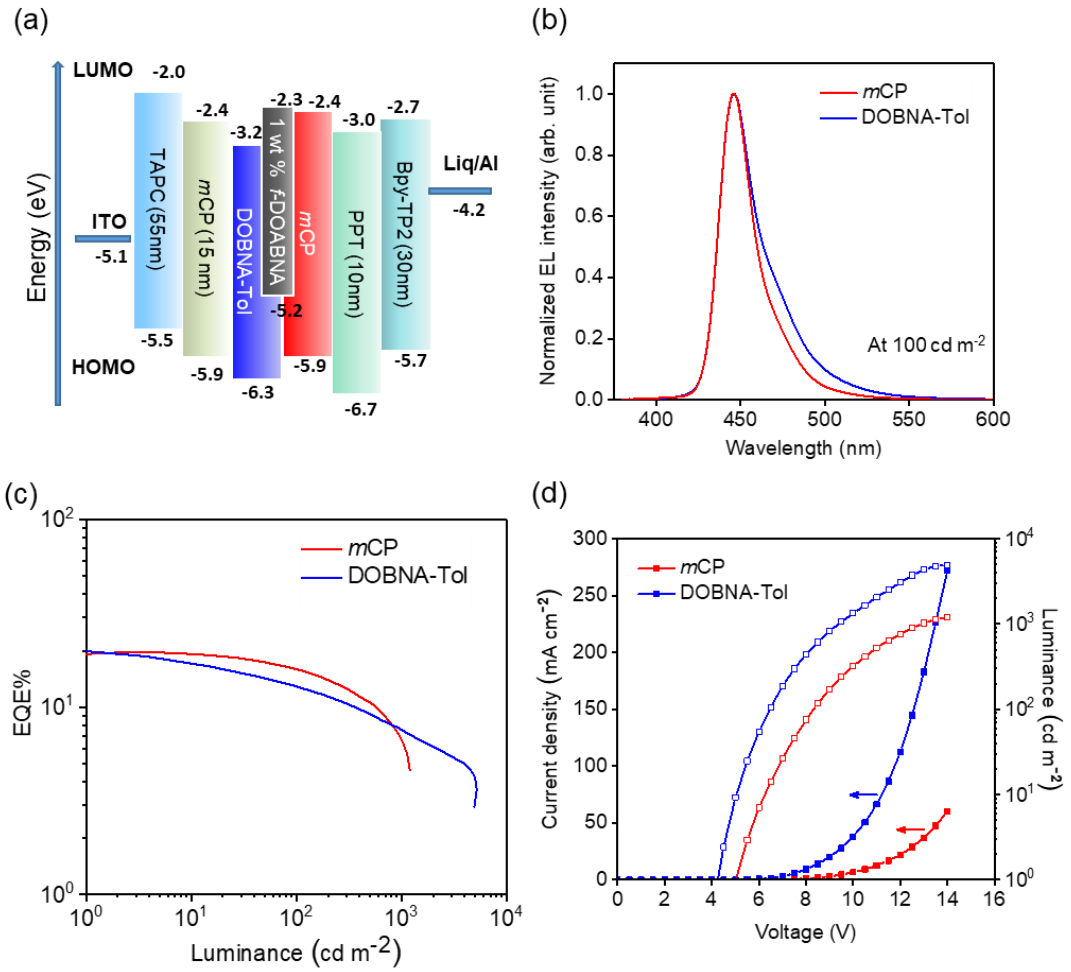

Figure 3-13. OLED performance of ***f*-DOABNA** (1 wt%) doped in ***m*CP** (red line) and **DOBNA-Tol** (blue line) hosts: (a) Device structure, (b) Electroluminescence spectra at 100 cd m^{-2}, (c) EQE vs. luminance curves, and (d) Current density (closed circle) and luminance (open circle) vs. driving voltage curves.

Table 3-7. Device performance of ***f*-DOABNA** in **DOBNA-Tol** or ***m*CP** as a host in the emissive layer.

Host	V_{on} (V)	EQE_{max} (%)	Lum_{max} (cd m^{-2})	CE (cd A^{-1})	PE (lm W^{-1})	λ_{EL} (nm)	FWHM (nm)	CIE (x,y)
DOBNA-Tol	4.2	19.9	4858	11.4	8.4	445	28	0.153, 0.056
***m*CP**	5.0	19.5	1194	7.6	4.7	445	24	0.150, 0.041

To determine whether the emitter's dipole orientation is favorably oriented in ***m*CP** and **DOBNA-Tol** hosts, which would contribute to enhanced light-outcoupling efficiency, angle-dependent PL studies in 1 wt% doped ***f*-DOABNA** in **DOBNA-Tol** and ***m*CP** were performed (**Figure 3-14**). The simulations were done with SETFOS software, where the horizontal-dipole ratios (Θ) of 0, 0.33, and 1 are assigned to perfectly horizontal, isotropic, and vertical orientation, respectively. The ***f*-DOABNA** doped in ***m*CP** film provided Θ of 0.21, giving 79% horizontal orientation of the dipole moment of ***f*-DOABNA** in ***m*CP**. The horizontal dipole orientation of ***f*-DOABNA** doped in **DOBNA-Tol** is slightly weaker, resulting in Θ = 0.26, yet giving 74% horizontal orientation, which is still favorable for light outcoupling. Therefore, the simulated light outcoupling efficiencies were almost similar with outcoupling efficiencies of 26 and 24% for 1 wt% ***f*-DOABNA** in ***m*CP** and **DOBNA-Tol** hosts, respectively.

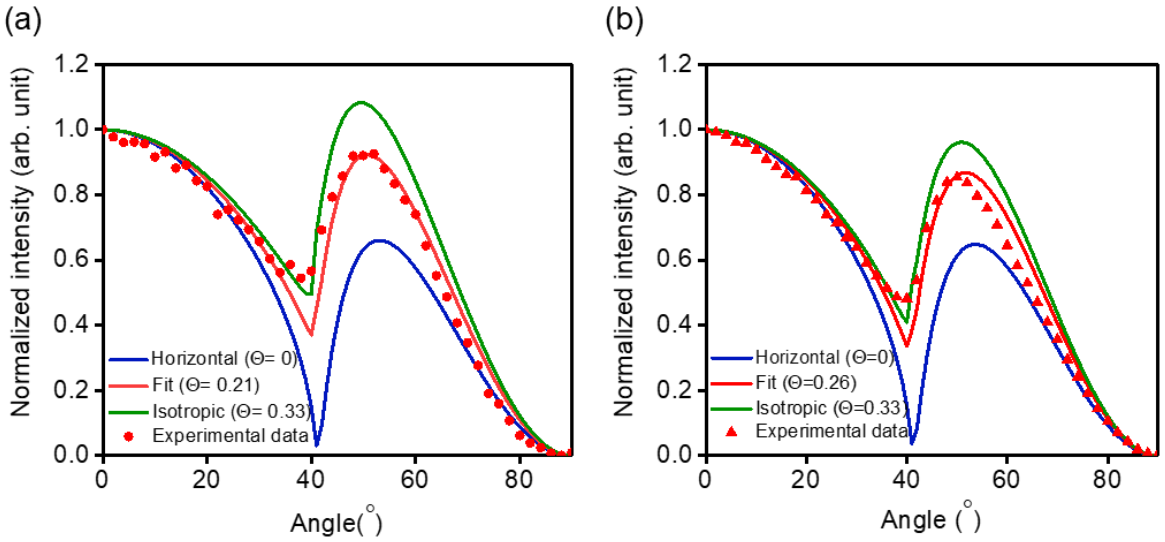

Figure 3-14. Angular-dependent PL profiles of 1 wt% ***f*-DOABNA** doped in ***m*CP** (a, closed circle) and **DOBNA-Tol** (b, closed triangle). The horizontal (blue lines), isotropic (green lines), and fitting curves for the experimental data (red lines) were provided using the optical simulation software SETFOS 4.6 (Fluxim).

As mentioned above, the color purity of the device with **DOBNA-Tol** host was poor compared to the device based on ***m*CP** due to the broadened EL spectrum. Moreover, **DOBNA-Tol** based devices exhibited undesirable roll-off at low current densities regardless of the faster k_{RISC} of ***f*-DOBNA** in **DOBNA-Tol** host. To rationalize this behavior, I studied the *J-V* characteristics of hole-only and electron-only devices (HOD and EOD) with both hosts (**Figure 3-15**).

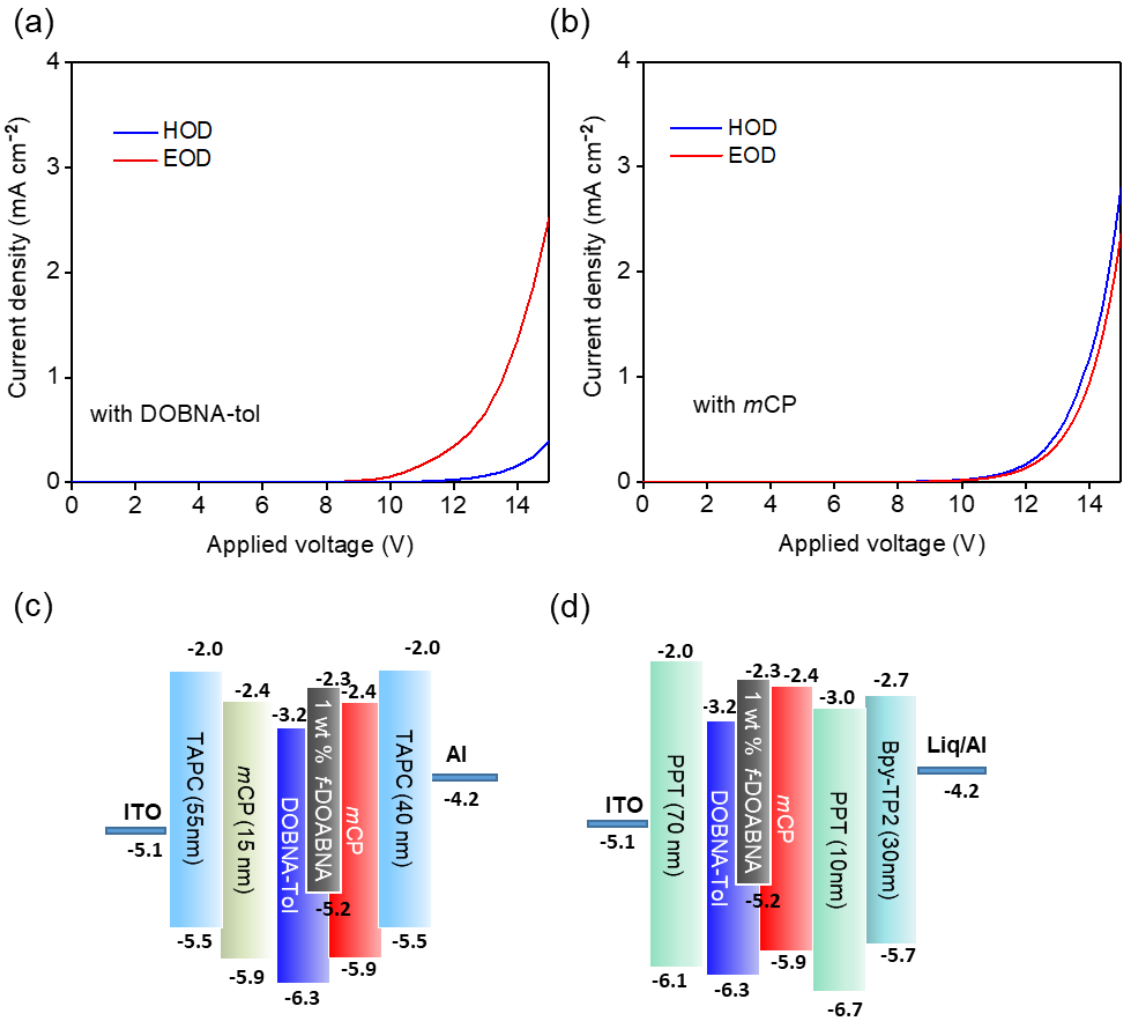

Figure 3-15. Current density Vs. driving voltage curves for HODs and EODs with different hosts (a) **DOBNA-Tol** and (b) ***m*CP**, and the device structures of (c) HODs and (d) EODs.

The *J-V* characteristics of HODs and EODs demonstrate balanced electron and hole-transporting properties in ***m*CP** based devices. In contrast, the **DOBNA-Tol** based device shows unbalanced charge transporting properties. Therefore, the efficiency roll-off and emission broadening in **DOBNA-Tol** based devices can be elucidated by the unbalanced carrier

transporting properties of **DOBNA-Tol**, causing the recombination zone to shift towards the EBL. Considering the HOMO energies of **DOBNA-Tol** and ***m*CP** with ***f*-DOABNA**, ***f*-DOABNA** should play as an efficient hole trap in both hosts. This strongly suggests that excitons are formed directly on ***f*-DOABNA** at low current densities. Meanwhile, electrons should be transported by the LUMO of hosts. With the unbalanced charge transporting properties in **DOBNA-Tol**, further electron accumulation would occur at the EBL:EML interface as current density increases, leading to significant polaron (electron)-exciton annihilation in **DOBNA-Tol** based devices ultimately causing efficiency roll-off.

Despite high EQE at low luminescence, the substantial efficiency roll-off in both devices at high brightness values remains an outstanding challenge to overcome. Moreover, the device lifetimes of ***f*-DOABNA** with both host materials are considerably short as depicted in **Figure 3-16**. Shorter device lifetimes and efficiency roll-off at high luminescence have been an issue for blue TADF and phosphorescent emitters for many years. However, this cannot be attributed only to the emitter's performance; there are other factors like the lack of a suitable host, stability of the host, and supporting layer materials. Due to the high T_1 of ***f*-DOABNA**, I can only use high T_1 host and exciton-blocking materials, which are chemically unstable, to confine the excitons. Thus, it is envisaged that the device efficiency roll-off can be greatly improved with more stable high T_1 hosts and exciton blocking materials.

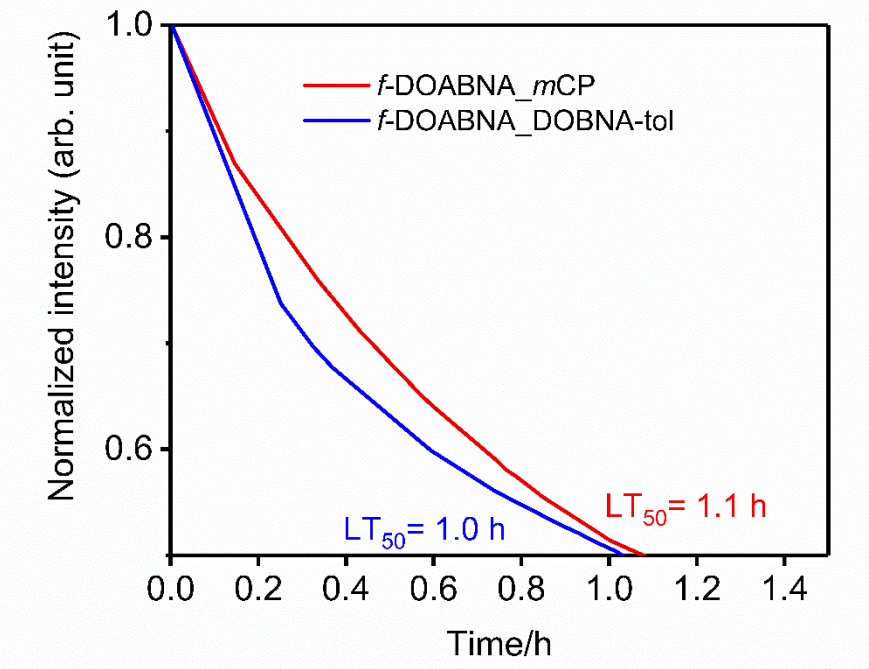

Figure 3-16. Device stability measurements: LT_{50} values of OLEDs with ***f*-DOABNA** in ***m*CP** (red) and **DOBNA-Tol** (blue) hosts.

3.3. Conclusion

A deep-blue helical MR-TADF emitter, ***f*-DOABNA** exhibited a small ΔE_{ST} of 80 meV, and a high SOC of 0.44 cm^{-1} owing to the delocalized π-conjugated structure with B, N, O heteroatoms leading to a short-delayed lifetime of 1.93 μs and an extraordinarily fast k_{RISC} rate of 1.02×10^6 s^{-1} in toluene. Most importantly, deep blue emission was possessed at 442 nm regardless of the π-conjugated structure, with a narrow FWHM of 18 nm and a high Φ_{PL} of 0.93. The k_{RISC} of ***f*-DOABNA** was further enhanced in 1 wt% doped films, particularly up to 2.3×10^6 s^{-1} in 1 wt% doped film in **DOBNA-Tol**, which, to the best of our understanding, represents one of the best values in k_{RISC} for deep-blue MR-TADF emitters. Notably, the devices based on the ***m*CP** host satisfied BT.2020 standard for blue pixel with CIEs of (0.150, 0.041) simultaneously achieving high EQE_{max} of nearly 20%. Therefore, in this study, I demonstrated outstanding device performance at this color point compared to the state-of-the-art, which I was able to achieve at low emitter doping and without the need to invoke a hyperfluorescence device structure.

3.3.Materials and methods

3.4.1. Material synthesis and characterization

***f*-DOABNA** was synthesized and characterized by Dr. S. M. Suresh in Prof. Zysman-Colman's group at St. Andrews University. The detailed synthesis procedures and the characterizations are attached in **Appendix B**.

3.4.2. Photophysical measurements

Organic thin films for photophysical measurements were fabricated on quartz substrates, which were pre-cleaned using acetone and isopropanol followed by 15 min UV treatment (NL-UV253, Nippon Laser & Electronics Lab., Japan) just prior to the film preparation to remove adsorbed organic species before deposition. Thin films for the streak camera measurements were prepared on silicon substrates. All the films were fabricated by vacuum thermal evaporation at a pressure below 10^{-4} Pa. UV-vis absorption spectroscopy was carried out using a Lambda 950-PKA spectrophotometer (Perkin-Elmer, USA). Fluorescence and phosphorescence measurements were acquired using an FP-8600 fluorometer (JASCO, Japan). A Quantaurus-QY C11347-01 (Hamamatsu Photonics, Japan) integrating sphere was used to

measure the absolute PL quantum yields, while the transient photoluminescence decays were measured with a Quantaurus-Tau C11367-03 (Hamamatsu Photonics, Japan) instrument. The thicknesses of all the films were measured using Variable-angle spectroscopic ellipsometry with an M-2000U (J.A. Woollam Co. Inc., USA) instrument.

3.4.3. Device fabrication and measurement of electroluminescence characteristics

OLEDs were fabricated on glass substrates coated with a patterned transparent ITO conductive layer (50 nm). ITO glass substrates were cleaned using detergent followed by de-ionized water, acetone, and isopropanol, and dried with isopropanol vapor. Then they were subjected to the UV treatment for 15 min just prior to the device fabrication. The devices were fabricated by using vacuum deposition under 1.0×10^{-5} Pa. The current density-voltage-luminance (*J*-*V*-*L*) characteristics of the OLEDs were assessed using a source meter (Keysight B2911A, Keysight Technologies, USA) and a luminance meter (CS-2000, Konica Minolta, Japan) at a constant DC current at room temperature. Device lifetimes were evaluated using a luminance meter (SR-3AR, TOPCON, Japan) under constant current density driving conditions with an initial luminance of 500 cd m^{-2}.

Chapter 4

Summary and Future Prospective

4.1. Summary

In this study, I focused on the, photophysical investigation and device engineering of novel deep-blue MR-TADF emitters with the objective of achieving both high color purity and high efficiency. Blue MR-TADF emitters often face significant challenges, including lower efficiency and color purity compared to their green and red counterparts. My goals were to address those issues as well as common drawbacks associated with MR-TADF emitters such as slow k_{RISC}, longer delayed lifetimes, small SOC values, etc., and to develop highly efficient deep-blue OLEDs that meet the stringent color specifications of the BT.2020 standard, which is critical for advanced display technology.

To address these drawbacks, I implemented strategic modifications in the molecular design of the emitters and proper device engineering to aim for highly efficient OLEDs with high color purity. My approach began with the identification of design strategies for novel MR-TADF molecules aimed at accomplishing my goal, followed by comprehensive characterization using a combination of theoretical calculations and experimental photophysical studies. Theoretical calculations were employed to predict the electronic properties and optimize the molecular structures, while experimental photophysical studies were conducted in both solution and film states to evaluate the excited-state characteristics of the emitters. In addition to photophysical characterization, I fabricated OLEDs incorporating each of the newly designed MR-TADF emitters with proper device engineering. The performances of these OLEDs were rigorously tested to assess their efficiency and color purity.

In **Chapter 2**, I introduced two deep-blue MR emitters, **1B-CzCrs** with an asymmetric structure and symmetric **2B-CzCrs**. These emitters were developed by introducing a carbazole moiety into the MR core of the previously reported emitters **1B-** and **2B-DTACrs** through ring fusing, and the impact of introducing the carbazole moiety to the MR core was thoroughly examined.[43] Interestingly, the asymmetric **1B-CzCrs** gained TADF activity through carbazole incorporation into the non-TADF **1B-DTACrs**. Although the carbazole moiety contributed to the expression of the TADF property in the minimum MR core, it reduced the k_{RISC} in the symmetrical MR structure. Additionally, the extended π-plane enhanced aggregation propensity, even with the introduction of several steric hindrance units. Contrary to their planar structure, the emitters exhibited a slightly vertical dipole orientation in the ***m*CP** matrix. The best device performance was achieved with the OLED incorporating **1B-CzCrs** in the ***m*CP** host, which could almost realize BT.2020 with a CIE of (0.146, 0.06) along with a moderate EQE of 12.8%. On the other hand, the devices with the ***m*CBP** host achieved CIE_y values below

0.05 for both emitters, while it resulted in a lower efficiency with an EQE_{max} of around 8% due to the charge imbalance (**Figure 4-1**). Despite the moderated performances of these emitters, particularly concerning the asymmetric design of **1B-CzCrs**, I provided here a comparative example that demonstrates enhanced photophysical properties. Therefore, this study suggests that molecular asymmetry combined with the planarization of MR core can induce and enhance TADF properties, which is a feasible approach that could potentially be implemented in future designs of MR-TADF emitters.

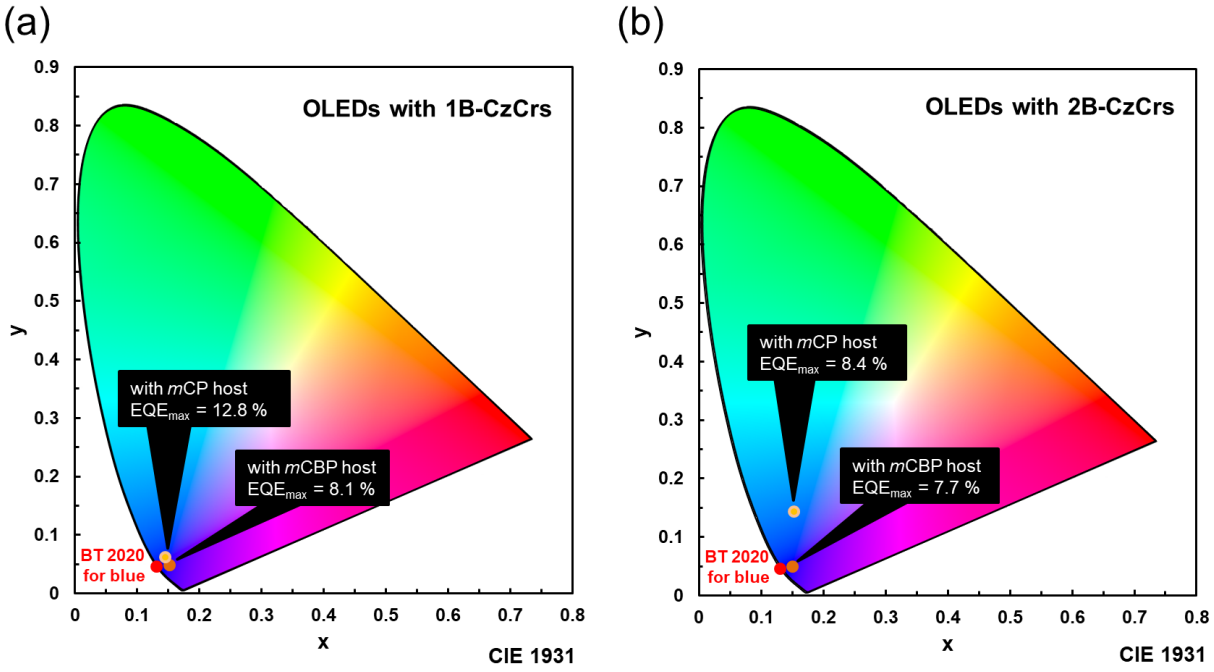

Figure 4-1. Representation of the CIE coordinates on the CIE 1931 color space chromaticity diagram for the OLEDs with (a) **1B-CzCrs** and (b) **2B-CzCrs**.

In **Chapter 3**, I approached a different molecular design strategy to accomplish my target. As a result, a narrowband emitting deep blue helical MR-TADF emitter, ***f*-DOABNA** (λ_{PL} = 442 nm and FWHM = 18 nm in toluene) was developed with the incorporation of B, N, and O heteroatoms. Even in the solution state where nonradiative decays are prominent, ***f*-DOABNA** exhibited high PLQY (93%) with a fast radiative rate and an exceptionally fast k_{RISC} rate of 1.02×10^6 s^{-1}, which is one of the highest values among MR-TADF emitters without heavy atom effect and reached the k_{RISC} range of conventional TADF emitters (**Figure 4-2**). Enhanced k_{RISC} was achieved by the synergistic effect of a small ΔE_{ST} and significant SOC between the S_1 and T_1 states. Therefore, this design strategy with the π-conjugated helical

structure succeeded in addressing the common drawbacks associated with MR-TADF emitters. Notably, unlike previously reported helical MR-TADF emitters, this small ΔE_{ST} was achieved without compromising color purity. With **DOBNA-Tol** as a host, ***f*-DOABNA** exhibited further enhanced k_{RISC} of 2.3 × 10^6 s^{-1} and a shorter delayed lifetime of 0.5 μs, which are the best values among the previously reported MR-TADF emitters to date.

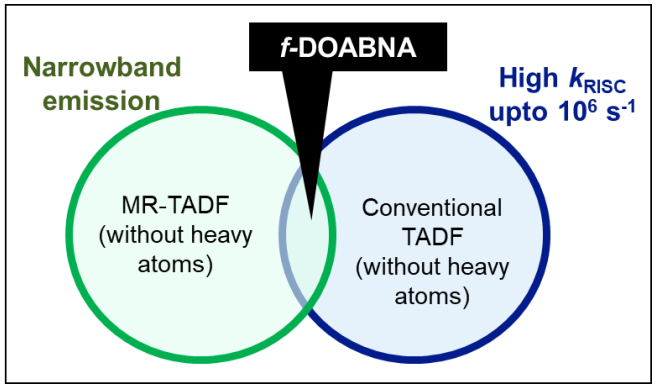

Figure 4-2. *f*-DOABNA with fast k_{RISC} and narrow emission.

Importantly, the device with the ***m*CP** host satisfied the most difficult-to-satisfy CIE_y value of BT.2020 standard for blue pixels, exhibiting CIE coordinates of (0.150, 0.041) and achieving a high EQE_{max} of nearly 20% (**Figure 4-3**). Therefore, this study was able to succeed in developing highly efficient binary OLED with high color purity without going for more complex device architectures such as hyperfluorescence systems. However, severe efficiency roll-off was observed in both devices. Therefore, to improve device stability, future studies should focus on developing stable hosts and exciton-blocking materials suitable for deep-blue emitters and hyperfluorescence architecture.

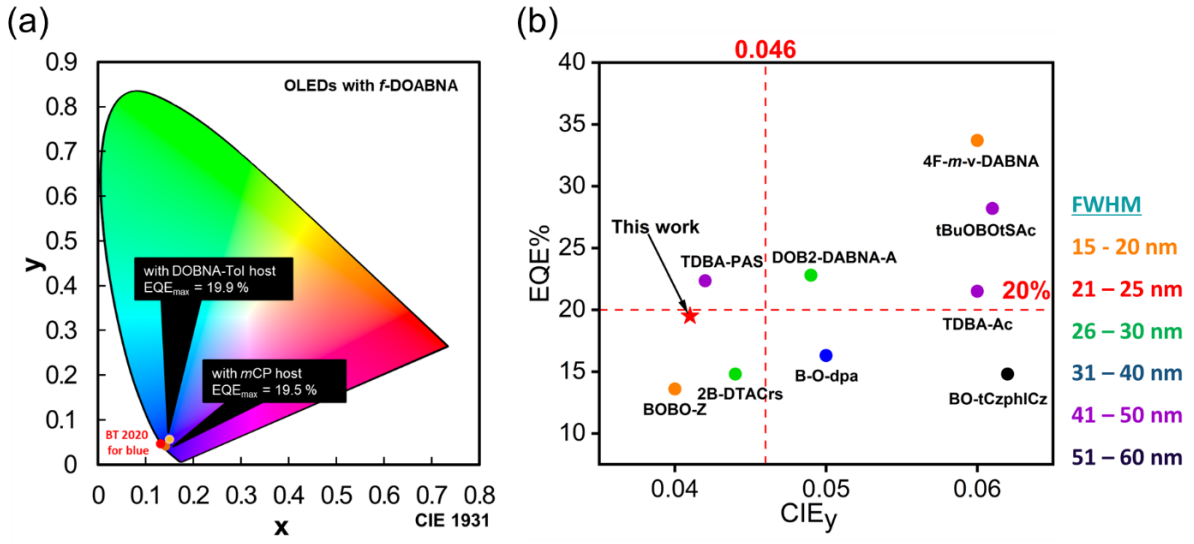

Figure 4-3. (a) CIE coordinates m for the OLEDs with ***f*-DOABNA** and (b) EQE vs CIE_y values of reported TADF/ MR-TADF molecules with corresponding FWHMs.

4.2. Future prospective

As described in **Chapter 3**, the unique molecular design of ***f*-DOABNA** resulted in exceptional photophysical properties, characterized by a fast k_{RISC} due to its small ΔE_{ST} and large SOC between the S_1 and T_1 states. These properties are attributed to its specific molecular structure. The design of ***f*-DOABNA** incorporates weaker electron- donating (wD) regions with **DOBNA** cores and stronger electron-donating (sD) regions with a **DABNA** core (**Figure 4-2**). This configuration induces LRCT while maintaining its MR nature, leading to a small ΔE_{ST} and a large SOC between S_1 and T_1. Notably, these advantageous properties were achieved without redshifting the emission, thanks to the **DOBNA** cores, unlike other π-conjugated systems with B, N cores.

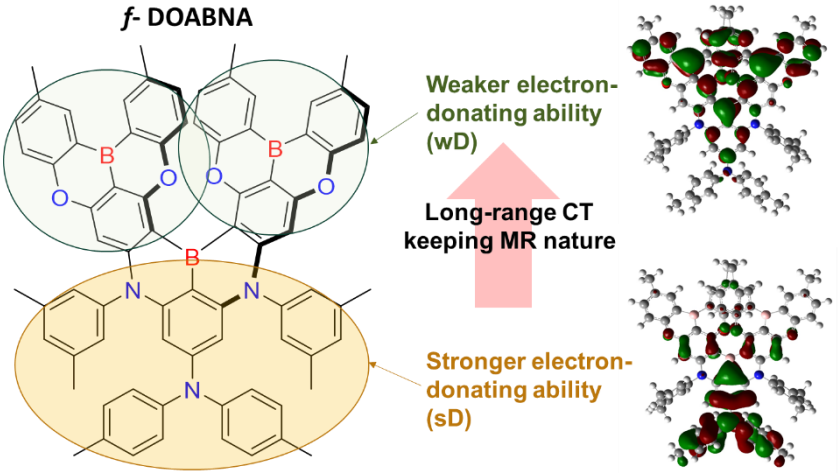

Figure 4-4. *f*-DOABNA with wD and sD regions for mixed SRCT and LRCT.

This phenomenon is further supported by recent reports of molecules with similar molecular designs (**Figure 4-5** and **Table 4.1**).[72,73] These results clearly indicate that a molecular design featuring wide and symmetrical orbital configurations as wD-sD-wD MR units is ideal for achieving fast k_{RISC} in MR-TADF emitters. Therefore, this molecular design can serve as a guideline for developing MR-TADF emitters with fast RISC. Therefore, in the future, I intend to further develop this molecular design strategy to achieve highly efficient deep-blue MR-TADF emitters. Furthermore, without limiting to deep blue, this design concept can be applied to green MR-TADF emitters by properly managing the emissions through structural modifications.

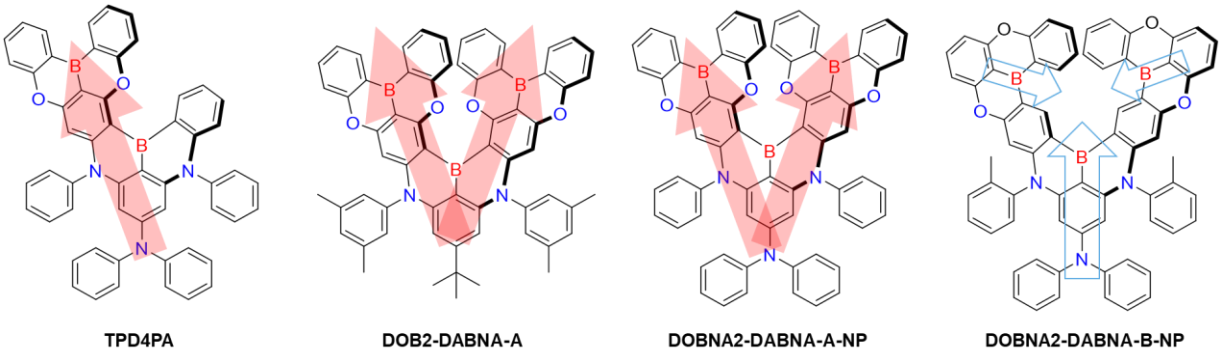

Figure 4-5. molecular structures of most recently reported MR-TADF emitters with similar molecular design to ***f*-DOABNA**.[40,73]

Figure 4-1. Photophysical properties and SOC values for the molecules in **Figure 4-5**.

	λ_{PL} (nm)	FWHM (nm)	ΔE_{ST} (meV)	SOC_{S1-T1} (cm^{-1})	SOC_{S1-T2} (cm^{-1})	k_{RISC} (10^5 s^{-1})	τ_d (μs)
TPD4PA	445	19	50	0.10	0.33	2.5	4.7
DOB2-DABNA-B-NP	471	27	3.6	0.059	0.895	3.8	3.0
DOB2-DABNA-A-NP	451	27	3.6	0.059	0.895	11.0	3.4
DOB2-DABNA-A	446	29	18	0.035	0.206	12.0	1.5
***f*-DOABNA**	444	25	20	0.44	0.01	23.0	0.5

Moreover, ***f*-DOABNA** demonstrated a considerably large SOC between S_1 and T_1 states, attributed to their distinct nature, whereas most MR materials exhibit a similar nature between S_1 and T_1 states.[74] However, this trend was not observed in the other molecules reported with the same design strategy, which show a larger SOC between S_1 and T_2 and a smaller SOC between S_1 and T_1 (**Table 4-1**). Understanding the mechanism behind the unique dissimilar nature between S_1 and T_1 in ***f*-DOABNA** would be beneficial for designing MR-TADF molecules to achieve high SOC between S_1 and T_1. To accomplish this, first a comprehensive theoretical assessment of the molecular geometries of these MR-emitters with several computational methods is required. Identifying the factors causing the distinct nature of S_1 and T_1 would lead to new design concepts for achieving high k_{RISC}.

In addition, device stability is a critical factor that should be taken into consideration for the commercialization of OLEDs. However, achieving a stable deep-blue OLED remains a

challenge, partially due to the instability of the host and supporting layer materials, which deteriorate the device stability. In this study, ***f*-DOABNA** exhibited exceptional TADF properties characterized by a high k_{RISC} and a shorter delayed lifetime when used with the **DOBNA-Tol** host. Furthermore, recent studies have consistently demonstrated that **DOBNA-Tol** is a promising host material for deep blue/blue MR-TADF emitters.[67,72] However, due to its smaller molecular weight (450 g mol^{-1}), **DOBNA-Tol** exhibits low thermal stability, which poses a challenge for thermal evaporation. Moreover, the crystallization was observed in **DOBNA-Tol** films over time, negatively impacting the device stability. The considerably planar structure also promotes aggregation in the solid state. To address these issues, modifications to the **DOBNA** core could grant better-performing host materials. In this regard, I plan to investigate **DOBNA**-based host materials with higher molecular weights, aiming to develop highly stable host materials for blue and green MR emitters. **Figure 4-6** shows the proposed structure for this study. Increased molecular weight would enhance thermal stability and facilitate the formation of amorphous films. Furthermore, I expect that partial overlap between two **DOBNA** cores will induce intra-molecular interactions, thereby locking the structure, reducing vibration motions, and leading to higher stability.

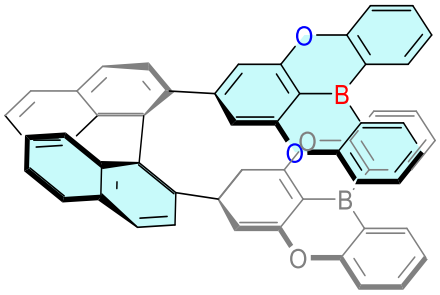

Figure 4-6. Proposed host, **BINAP-DOBNA2**.

References

[1] P. Atkins, J. De Paula, *Atkins' Physical Chemistry. 10th Ed.,* Oxford University Press*:* Oxford, **2014***, 1008*.

[2] N. J. Turro, *Modern Molecular Photochemistry. University Science Books,* California, **1991***, 628.*

[3] H. Nakanotani, K. Masui, J. Nishide, T. Shibata, C. Adachi, *Sci. Rep.* **2013**, *3*, 2127.

[4] H. Uoyama, K. Goushi, K. Shizu, H. Nomura, C. Adachi, *Nature.* **2012**, *492*, 234.

[5] C. W. Tang, S. A. VanSlyke, *Appl. Phys. Lett.* **1987**, *51*, 913.

[6] G. Hong, X. Gan, C. Leonhardt, Z. Zhang, J. Seibert, J. M. Busch, S. Bräse, *Adv. Mater.* **2021**, *33*. 202005630.

[7] Y. Pu, G. Nakata, F. Satoh, H. Sasabe, D. Yokoyama, J. Kido, *Adv. Mater.* **2012**, *24*, 1765–1770.

[8] J. C. Scott, S. Karg, S. A. Carter, *J. Appl. Phys.* **1997**, *82*, 1454.

[9] A. Köhler, H. Bässler, *Mater. Sci. Eng. R.* **2009**, *66*, 71–109.

[10] Q.-L. Xu, X. Liang, S. Zhang, Y.-M. Jing, X. Liu, G.-Z. Lu, Y.-X. Zheng, J.-L. Zuo, *J Mater. Chem. C.* **2015**, *3*, 3694.

[11] M. Kim, J. Y. Lee, *ACS Appl. Mater. Interfaces.* **2014**, *6*, 14874.

[12] C. W. Lee, J. Y. Lee, *Adv. Mater.* **2013**, *25*, 5450.

[13] C. Adachi, M. A. Baldo, M. E. Thompson, S. R. Forrest, *J. Appl. Phys.* **2001**, *90*, 5048.

[14] M. Godumala, S. Choi, M. J. Cho, D. H. Choi, *J. Mater. Chem.* **2016**, *4*, 11355.

[15] M. Zhu, C. Yang, *Chem. Soc. Rev.* **2013**, *42*, 4963.

[16] P. Rajamalli, N. Senthilkumar, P. Gandeepan, P.-Y. Huang, M.-J. Huang, C.-Z. Ren-Wu, C.-Y. Yang, M.-J. Chiu, L.-K. Chu, H.-W. Lin, C.-H. Cheng, *J. Am. Chem. Soc.* **2016**, *138*, 628.

[17] R. Delorme, F. Perrin, *J. Phys. Radium.* **1929**, *10*, 177.

[18] G. N. Lewis, D. Lipkin, T. T. Magel, *J. Am. Chem. Soc.* **1941**, *63*, 3005.

[19] C. A. Parker, C. G. Hatchard, *J. Chem. Soc., Faraday Trans.* **1961**, *57*, 1894.

[20] F. Wilkinson and A. R. Horrocks, *Phosphorescence and delayed fluorescence of organic substances Luminescence in Chemistry*, Van Nostrand, London, **1968**, 116–53.

[21] C. A. Parker, T. A. Joyce, *Photochem. Photobiol.* **1967**, *6*, 395.

[22] M. N. Berberan-Santos, J. M. M. Garcia, *J. Am. Chem. Soc.* **1996**, *118*, 9391.

[23] R. E. Brown, L. A. Singer, J. H. Parks, *Chem. Phys. Lett.* **1972**, *14*, 193.

[24] A. Endo, M. Ogasawara, A. Takahashi, D. Yokoyama, Y. Kato, C. Adachi, *Adv. Mater.* **2009**, *21*, 4802.

[25] A. Endo, K. Sato, K. Yoshimura, T. Kai, A. Kawada, H. Miyazaki, C. Adachi, *Appl. Phys. Lett.* **2011**, *98*, 3558906.

[26] H. J. Kim, T. Yasuda, *Adv. Opt. Mater.* **2022**, *10*, 2201714.

[27] T. Hatakeyama, K. Shiren, K. Nakajima, S. Nomura, S. Nakatsuka, K. Kinoshita, J. Ni, Y. Ono, T. Ikuta, *Adv. Mater.* **2016**, *28*, 2777.

[28] S. Madayanad Suresh, D. Hall, D. Beljonne, Y. Olivier, E. Zysman-Colman, *Adv. Funct. Mater.* **2020**, *30*, 1908677.

[29] B. A. Naqvi, M. Schmid, E. Crovini, P. Sahay, T. Naujoks, F. Rodella, Z. Zhang, P. Strohriegl, S. Bräse, E. Zysman-Colman, W. Brütting, *Front. Chem.* **2020**, *8*, 33102430.

[30] F. B. Dias, T. J. Penfold, A. P. Monkman, *Methods Appl. Fluoresc.* **2017**, *5*, 012001.

[31] T. J. Penfold, F. B. Dias, A. P. Monkman, *Chem. Commun.* **2018**, *54*, 3926.

[32] N. Lin, J. Qiao, L. Duan, L. Wang, Y. Qiu, *J. Phys. Chem. C.* **2014**, *118*, 7569.

[33] Y. Liu, C. Li, Z. Ren, S. Yan, M. R. Bryce, *Nat. Rev. Mater.* **2018**, *3*, 18020.

[34] Z. Yang, Z. Mao, Z. Xie, Y. Zhang, S. Liu, J. Zhao, J. Xu, Z. Chi, M. P. Aldred, *Chem. Soc. Rev.* **2017**, *46*, 915.

[35] Y. Im, M. Kim, Y. J. Cho, J.-A. Seo, K. S. Yook, J. Y. Lee, *Chem. Mater.* **2017**, *29*, 1946.

[36] A. Pershin, D. Hall, V. Lemaur, J.-C. Sancho-Garcia, L. Muccioli, E. Zysman-Colman, D. Beljonne, Y. Olivier, *Nat. Commun.* **2019**, *10*, 597.

[37] Y. Ohno, CIE fundamentals for color measurements, NIP & Digital Fabrication Conference, Society of Imaging Science and Technology. **2000**, pp. 425–873.

[38] *In BT.2020-2 (10/2015), Vol. 2015-10, International Telecommunication Union, Geneva, Switzerland 2015*.

[39] X. Fan, X. Hao, F. Huang, J. Yu, K. Wang, X. Zhang, *Adv. Sci.* **2023**, *10*, 2303504.

[40] M. Mamada, M. Hayakawa, J. Ochi, T. Hatakeyama, *Chem. Soc. Rev.* **2024**, *53*, 1624.

[41] S. K. Jeon, H. L. Lee, K. S. Yook, J. Y. Lee, *Adv. Mater.* **2019**, *31*, 1803524.

[42] I. S. Park, M. Yang, H. Shibata, N. Amanokura, T. Yasuda, *Adv. Mater.* **2022**, *34*, 2107951.

[43] C.-Y. Chan, S. Madayanad Suresh, Y.-T. Lee, Y. Tsuchiya, T. Matulaitis, D. Hall, A. M. Z. Slawin, S. Warriner, D. Beljonne, Y. Olivier, C. Adachi, E. Zysman-Colman, *Chem.Commun.* **2022**, *58*, 9377.

[44] H. Nakanotani, T. Higuchi, T. Furukawa, K. Masui, K. Morimoto, M. Numata, H. Tanaka, Y. Sagara, T. Yasuda, C. Adachi, *Nat. Commun.* **2014**, *5*, 4016.

[45] F. Tenopala-Carmona, O. S. Lee, E. Crovini, A. M. Neferu, C. Murawski, Y. Olivier, E. Zysman-Colman, M. C. Gather, *Adv. Mater.* **2021**, *33*, 2100677.

[46] K. R. Naveen, H. Lee, R. Braveenth, K. Joon Yang, S. Jae Hwang, J. Hyuk Kwon, *Chem. Eng. J.* **2022**, *432*, 134381.

[47] Y. Kondo, K. Yoshiura, S. Kitera, H. Nishi, S. Oda, H. Gotoh, Y. Sasada, M. Yanai, T. Hatakeyama, *Nat. Photon.* **2019**, *13*, 678.

[48] H. Tanaka, S. Oda, G. Ricci, H. Gotoh, K. Tabata, R. Kawasumi, D. Beljonne, Y. Olivier, T. Hatakeyama, *Angew. Chem. Int. Ed.* **2021**, *60*, 17910.

[49] Y. Qi, W. Ning, Y. Zou, X. Cao, S. Gong, C. Yang, *Adv. Funct. Mater.* **2021**, *31*, 202102017.

[50] Y. Lee, J. Hong, *Adv. Opt. Mater.* **2021**, *9*, 202100406.

[51] J. Park, J. Lim, J. H. Lee, B. Jang, J. H. Han, S. S. Yoon, J. Y. Lee, *ACS Appl. Mater. Interfaces.* **2021**, *13*, 45798.

[52] H. Tan, G. Yang, Y. Deng, C. Cao, J. Tan, Z. Zhu, W. Chen, Y. Xiong, J. Jian, C. Lee, Q. Tong, *Adv. Mater.* **2022**, *34*, 2200537.

[53] D. H. Ahn, S. W. Kim, H. Lee, I. J. Ko, D. Karthik, J. Y. Lee, J. H. Kwon, *Nat. Photon.* **2019**, *13*, 540.

[54] H. Lim, H. J. Cheon, S. Woo, S. Kwon, Y. Kim, J. Kim, *Adv. Mater.* **2020**, *32*, 2004083.

[55] Y. Gan, X. Peng, W. Qiu, L. Wang, D. Li, W. Xie, D. Liu, M. Li, J. Lin, S.-J. Su, *Chem. Eng. J.* **2022**, *430*, 133030.

[56] J. Hwang, C. W. Koh, J. M. Ha, H. Y. Woo, S. Park, M. J. Cho, D. H. Choi, *ACS Appl. Mater. Interfaces.* **2021**, *13*, 61454.

[57] Y. Zhang, D. Zhang, J. Wei, Z. Liu, Y. Lu, L. Duan, *Angew. Chem. Int. Ed.,* **2019**, *58*, 16912.

[58] T. Serevičius, R. Skaisgiris, I. Fiodorova, V. Steckis, J. Dodonova, D. Banevičius, K. Kazlauskas, S. Juršėnas, S. Tumkevičius, *Org. Electron.* **2020**, *82*, 105723.

[59] J. Bae, M. Sakai, Y. Tsuchiya, N. Ando, X.-K. Chen, T. B. Nguyen, C.-Y. Chan, Y.-T. Lee, M. Auffray, H. Nakanotani, S. Yamaguchi, C. Adachi, *Front. Chem.* **2022**, *10*, 10:990918.

[60] J. Mooney, P. Kambhampati, *J. Phys. Chem. Lett.* **2013**, *4*, 3316.

[61] N. Notsuka, H. Nakanotani, H. Noda, K. Goushi, C. Adachi, *J. Phys. Chem. Lett.* **2020**, *11*, 562.

[62] Y. Tsuchiya, S. Diesing, F. Bencheikh, Y. Wada, P. L. dos Santos, H. Kaji, E. Zysman-Colman, I. D. W. Samuel, C. Adachi, *J. Phys. Chem. A.* **2021**, *125*, 8074.

[63] F. Rodella, S. Bagnich, E. Duda, T. Meier, J. Kahle, S. Athanasopoulos, A. Köhler, P. Strohriegl, *Front. Chem.* **2020**, *8*, 657.

[64] S. Ihn, D. Jeong, E. S. Kwon, S. Kim, Y. S. Chung, M. Sim, J. Chwae, Y. Koishikawa, S. O. Jeon, J. S. Kim, J. Kim, S. Nam, I. Kim, S. Park, D. S. Kim, H. Choi, S. Kim, *Adv. Sci.* **2022**, *9*, 2102141.

[65] J.-M. Teng, Y.-F. Wang, C.-F. Chen, *J. Mater. Chem.* **2020**, *8*, 11340.

[66] S. Oda, B. Kawakami, Y. Yamasaki, R. Matsumoto, M. Yoshioka, D. Fukushima, S. Nakatsuka, T. Hatakeyama, *J. Am. Chem. Soc.* **2022**, *144*, 106.

[67] S. Oda, B. Kawakami, M. Horiuchi, Y. Yamasaki, R. Kawasumi, T. Hatakeyama, *Adv. Sci.* **2023**, *10*, 2205070.

[68] S. Madayanad Suresh, L. Zhang, D. Hall, C. Si, G. Ricci, T. Matulaitis, A. M. Z. Slawin, S. Warriner, Y. Olivier, I. D. W. Samuel, E. Zysman-Colman, *Angew. Chem. Int. Ed.* **2023**, *62*, e202215522.

[69] S. M. Suresh, L. Zhang, T. Matulaitis, D. Hall, C. Si, G. Ricci, A. M. Z. Slawin, S. Warriner, D. Beljonne, Y. Olivier, I. D. W. Samuel, E. Zysman-Colman, *Adv. Mater.* **2023**, *35*, 2300997.

[70] H. Hirai, K. Nakajima, S. Nakatsuka, K. Shiren, J. Ni, S. Nomura, T. Ikuta, T. Hatakeyama, *Angew. Chem. Int. Ed.* **2015**, *54*, 13581.

[71] D. Hall, J. C. Sancho-García, A. Pershin, G. Ricci, D. Beljonne, E. Zysman-Colman, Y. Olivier, *J. Chem. Theory Comput.* **2022**, *18*, 4903.

[72] J. Ochi, Y. Yamasaki, K. Tanaka, Y. Kondo, K. Isayama, S. Oda, M. Kondo, T. Hatakeyama, *Nat. Commun.* **2024**, *15*, 2361.

[73] K. R. Naveen, H. Lee, L. H. Seung, Y. H. Jung, C. P. Keshavananda Prabhu, S. Muruganantham, J. H. Kwon, *Chem. Eng. J.* **2023**, *451*, 138498.

[74] D. Hall, J. C. Sancho-García, A. Pershin, G. Ricci, D. Beljonne, E. Zysman-Colman, Y. Olivier, *J. Chem. Theory Comput.* **2022**, *18*, 4903.

List of abbreviations

- **A** Acceptor
- **BT** Broadcasting television
- **CIE** Commission Internationale de L'Éclairage
- **CT** Charge transfer
- **CV** Cyclic voltammetry
- **D** Donor
- **DFT** Density functional theory
- **DPA** Diphenylamine
- **EBL** Electron blocking layer
- **EML** Emitting layer
- **EL** Electroluminescence
- **EQE** External quantum efficiency
- **EQE_{max}** Maximum quantum efficiency
- **ETL** Electron transporting layer
- ***f*** Oscillator strength
- **FWHM** Fullwidth at half maximum
- **HBL** Hole blocking layer
- **HOMO** Highest occupied molecular orbital
- **HTL** Hole transporting layer
- **IRF** Instrument response function
- **ISC** Intersystem crossing
- **ITO** Indium tin oxide
- k_{nr} Non-radiative rate constant
- k_{nr}^{S} Singlet non-radiative rate constant
- k_{nr}^{T} Triplet non-radiative rate constant
- k_{ISC} Intersystem crossing rate constant
- k_{RISC} Reverse intersystem crossing rate constant
- k_r^S Fluorescence radiative rate constant
- k_r^S Phosphorescence radiative rate constant
- **LE** Locally excited

- **Lum_{max}** Maximum luminance
- **LUMO** Lowest unoccupied molecular orbital
- **MR** Multiple resonance
- **OLED** Organic light emitting diode
- **PL** Photoluminescence
- **PLQY** Photoluminescence quantum yield
- **RISC** Revers intersystem crossing
- **TADF** Thermally activated delayed fluorescence
- **S_0** Singlet ground state
- **S_1** Lowest singlet excited state
- **S_2** Second lowest singlet excited state
- **sD** Stronger electron donating
- **SOC** Spin-orbit coupling
- **SRCT** Short-range charge transfer
- **T_1** Lowest triplet excited state
- **T_2** Second lowest triplet excited state
- **TADF** Thermally activated delayed fluorescence
- **TDA-DFT** Tamm-Dancoff approximation
- **TD-DFT** Time-dependent density functional theory
- **wD** Weaker electron donating
- **ΔE_g** Energy difference between HOMO and LUMO
- **ΔE_{ST}** Energy difference between lowest singlet and triplet excited state
- **ε** Molar extinction coefficient
- **Φ_{PL}** Photoluminescence quantum yield
- **λ_{PL}** Photoluminescence emission maximum
- **λ_{exc}** Excitation wavelength
- **λ_{EL}** Electroluminescence emission maximum
- **τ_d** Delayed fluorescence lifetime
- **τ_p** Promt fluorescence lifetime

List of publication

- **Papers (first authorship)**

  - **R. W. Weerasinghe**[#], S. M. Suresh[#], D. Hall, T. Matulaitis, A. M. Z. Slawin, S. Warriner, Y-T. Lee; C-Y. Chan, Y. Tsuchiya, E. Zysman-Colman, and C. Adachi, *Adv. Mater.* **2024**, *36*, 2402289.
    ([#]Equally contributed with S. M. Suresh)

  - **R. W. Weerasinghe**, J. M. Dos Santos, D. Hall, Y. Chitose, D. Barman, C-Y. Chan, Y. Tsuchiya, E. Zysman-Colman, C. Adachi, Molecular asymmetry and rigidification as strategies to activate and enhance thermally activated delayed fluorescence in deep-blue MR-TADF emitters. *Phys. Chem. Chem, Phys*.

- **Joint papers**

  - Y-T. Lee; C-Y Chan, N. Matsuno, S. Uemura, S. Oda, M. Kondo, **R. W. Weerasinghe**, Y. Hu, G. N. I. Lestanto, Y. Tsuchiya, Y. Li, T. Hatakeyama, C. Adachi, *Nat. Commun.* **2024**, *15*, 3174.

- **The list of presentations at international conferences**

  - **R. W. Weerasinghe**, S. M. Suresh, D. Hall, C-Y. Chan, Y. Tsuchiya, E. Zysman-Colman, C. Adachi, *Japan Society of Applied Physics (JSAP Spring meeting-**2024**), Toky*o, Japan (March 22, **2024**, Oral presentation).

Acknowledgment

The studies presented in this thesis were conducted at the Adachi Laboratory, Department of Chemistry and Biochemistry, Graduate School of Engineering, Kyushu University, from 2022 to 2024.

First, I am deeply grateful to Prof. Chihaya Adachi for his continuous guidance and motivation throughout the entire research. This thesis would not have been possible without his excellent guidance and valuable suggestions. Throughout my PhD journey, he has provided immense supervision and assisted in the proper direction.

I would also like to express my sincere gratitude to Prof. Takuma Yasuda and Prof. Yuji Oki for taking the time to evaluate this thesis and for their valuable suggestions and comments.

My sincere thanks go to Prof. Youichi Tsuchiya for co-supervising me and for training me on various instruments essential for my research. His continuous encouragement, support, and guidance have been pivotal to my studies. I also extend my heartfelt thanks to Prof. Chin-Yiu Chan, currently working at City University of Hong Kong, for his co-supervision during the first year of my PhD and for his continued support thereafter.

I am indebted to Prof. Eli Zyzman-Colman of the University of St. Andrews, UK, and his research team, especially, Dr. S. M. Suresh and Dr. J. Dos Santos, for providing excellent molecules and for their helpful discussions and kind support.

I am grateful to Prof. Hajime Nakanotani for preparing me for departmental examinations, offering insightful comments, and providing kind support in my research. Additionally, I am grateful to Prof. Kenichi Goushi for his helpful discussions and support in my experiments. Moreover, I am thankful to Prof. Youhei Chitose for his kind support and discussions that greatly aided my understanding of the subject matter.

I would like to extend my gratitude to Prof. Atula Sandanayake, currently working at the University of Sabaragamuwa, Sri Lanka, for his kind assistance throughout my PhD journey. I am also thankful to Dr. C.M. Seneviratne, Dr. Bhuddika Karunathilake and Tharindu for their valuable discussions and kind support.

I would like to express my sincere thanks to Ms. Sachiko Higashikawa, Ms. Yuko Kawahara, Ms. Noriko Ooga, and Ms. Hino Nakanotani for their friendliness and kind support during my stay at OPERA. I am indebted to Ms. Ayano Abe, Mr. Nguyen Ba Thanh, Mr. Shintero Kohata, Mr. Sanghoon Lee, Ms. Nakamuka, and Mr. Keito Mizukoshi for teaching me to use various instruments at the beginning of my study. My gratitude also extends to all

OPERA members for their kind support in experiments and day-to-day life in the laboratory.

I am deeply grateful to the Japanese government for generously funding my PhD journey through the Monbukagakusho (MEXT) scholarship.

Last but not least, I would like to extend my deepest appreciation to my parents, my husband, and my friends for their continued support and encouragement to pursue my interest in this research.

Rangani Wathsala Weerasinghe
17.06.2024

Appendix A

Synthesis and characterization of 1B-CzCrs, and 2B-CzCrs.

The synthetic route to **1B-** and **2B-CzCrs** is outlined in **Figure A-1.** 4,4'-((5-Bromo-1,3-phenylene) bis(oxy)) bis(methylbenzene) (compound **1**), of which the synthesis was reported in our previous study[43] was first reacted with 3,6-di-*tert*-butylcarbazole (compound **2**) by palladium-catalyzed Buchwald-Hartwig cross-coupling reaction. Then, bromination of compound **3** was performed using N-bromosuccinimide at low temperatures. The brominated compound **4** was further coupled with *o*-tolylboronic acid, resulting in compound **5** in a good yield (95%). **1B-** and **2B-CzCrs** were obtained following a bora-Friedel-Crafts reaction with the help of BI_3, in 15 and 12% yield, respectively.

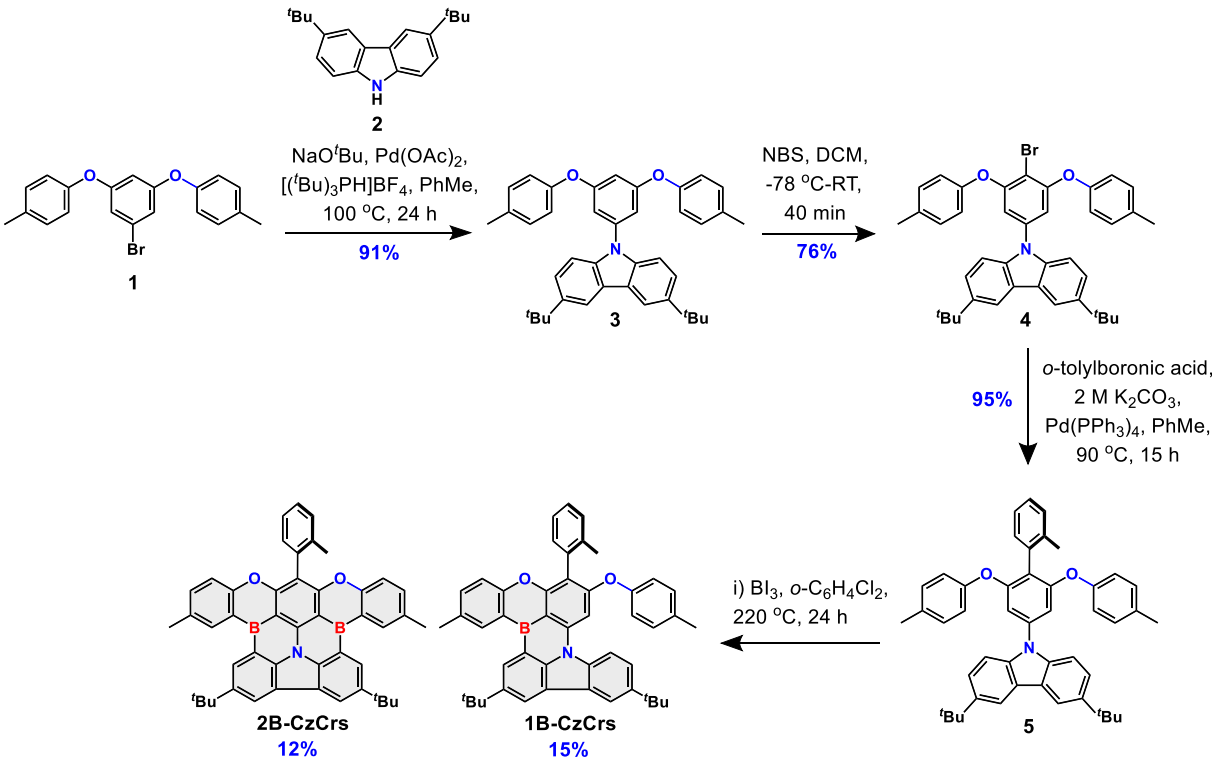

Figure A-1. The synthetic route of the **1B-** and **2B-CzCrs**.

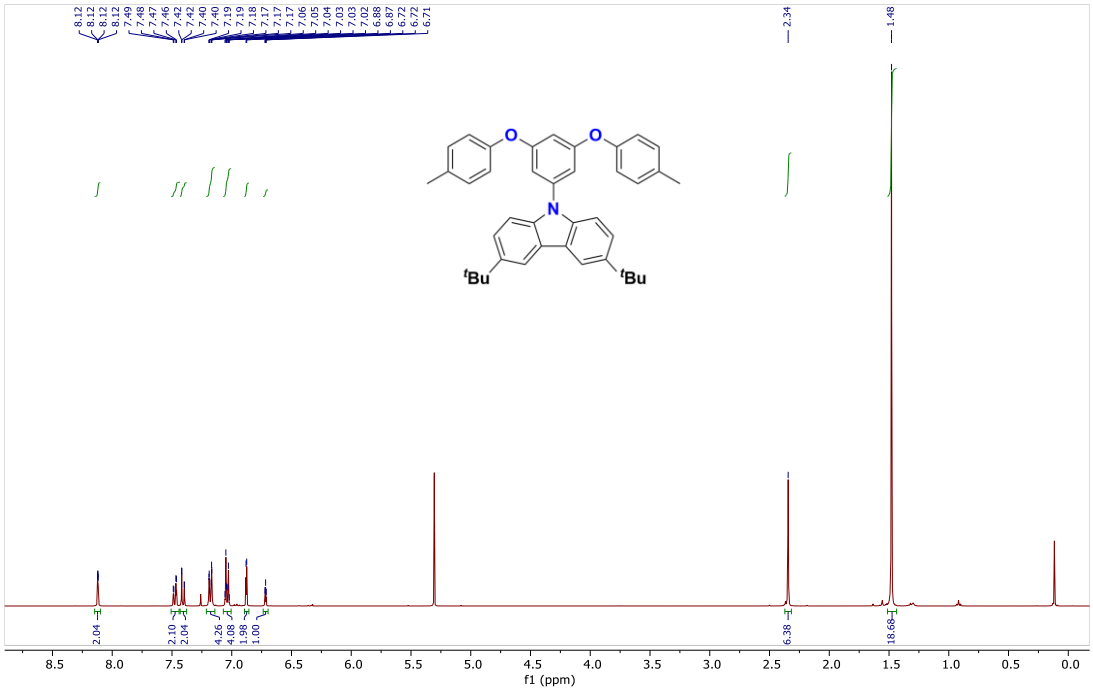

Figure A-2.[1]H NMR (400 MHz, $CDCl_3$) spectrum of **3**.

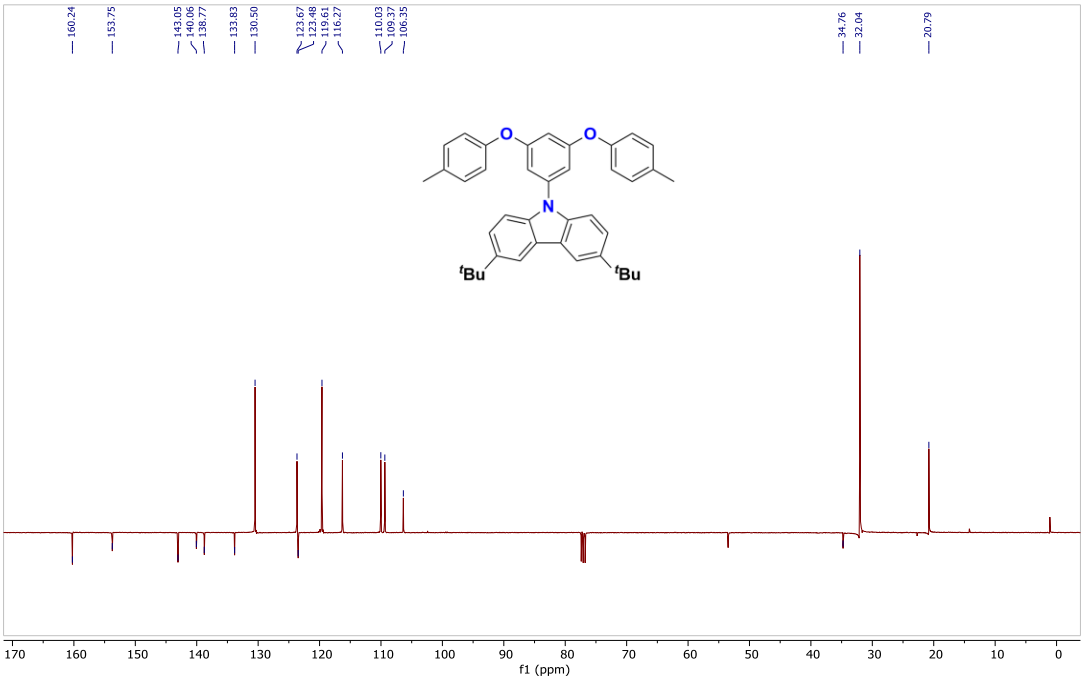

Figure A-3. [13] DEPTq-135 (101 MHz, $CDCl_3$) spectrum of **3**.

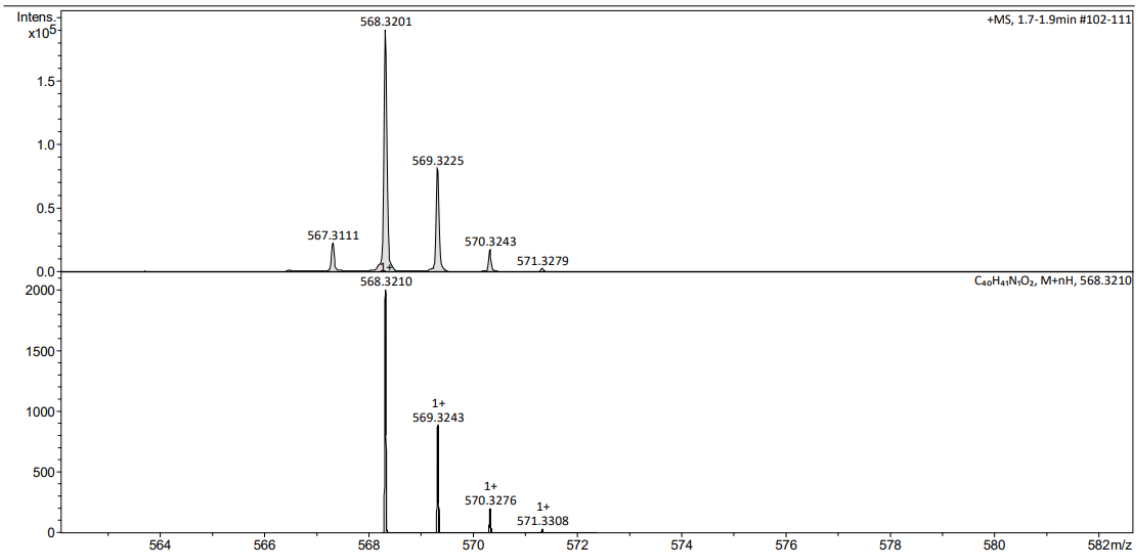

Figure A-4. HRMS of compound **3**.

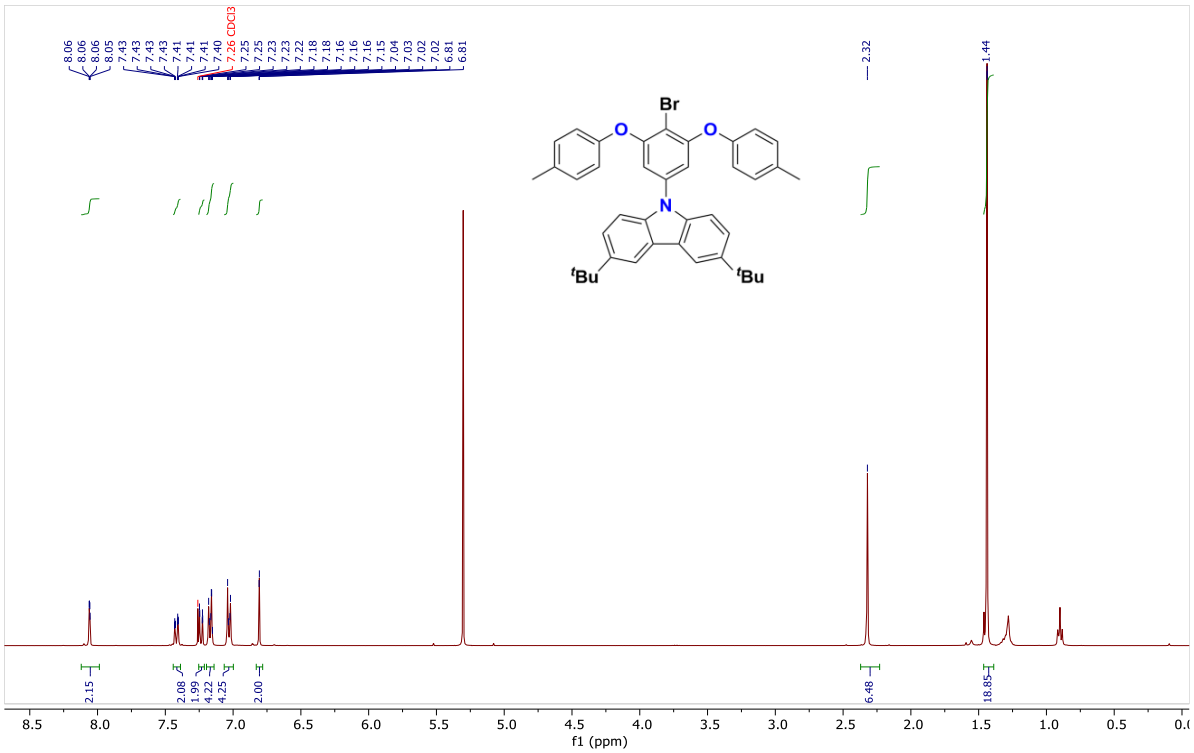

Figure A-5. ^{1}H NMR (400 MHz, $CDCl_3$) spectrum of **4**.

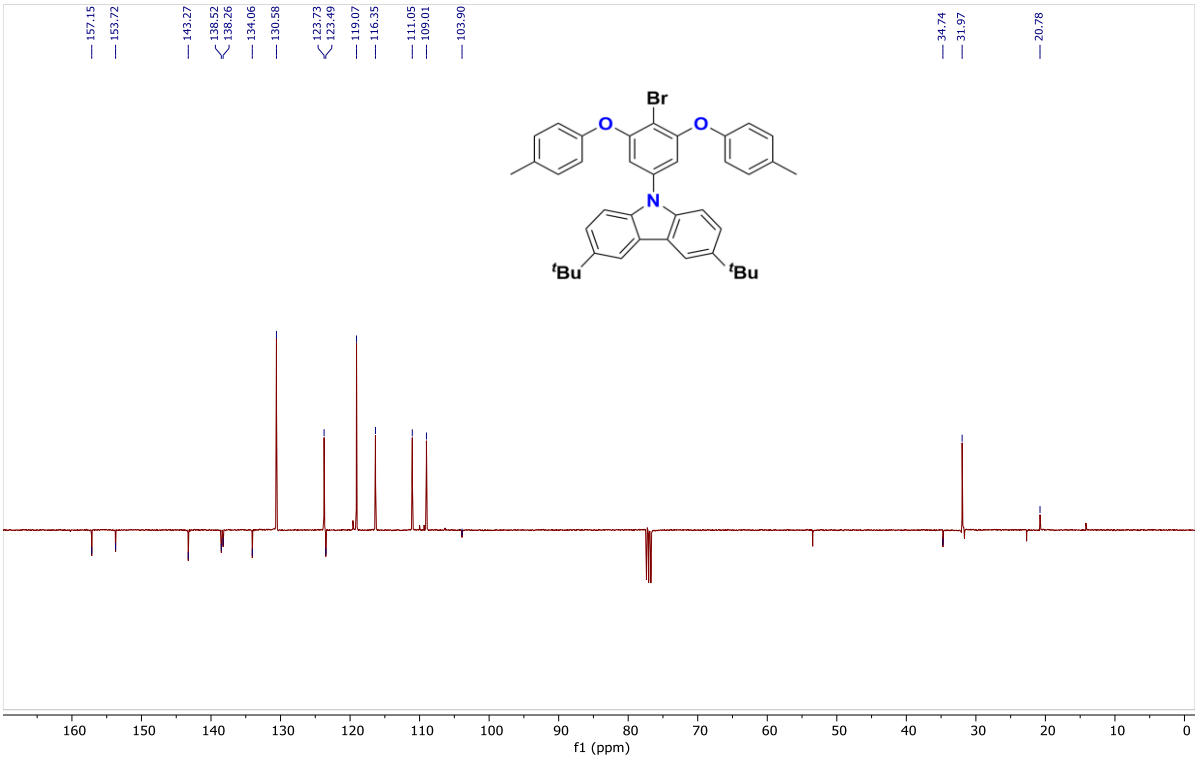

Figure A-6. DEPTq-135 (101 MHz, $CDCl_3$) spectrum of **4**.

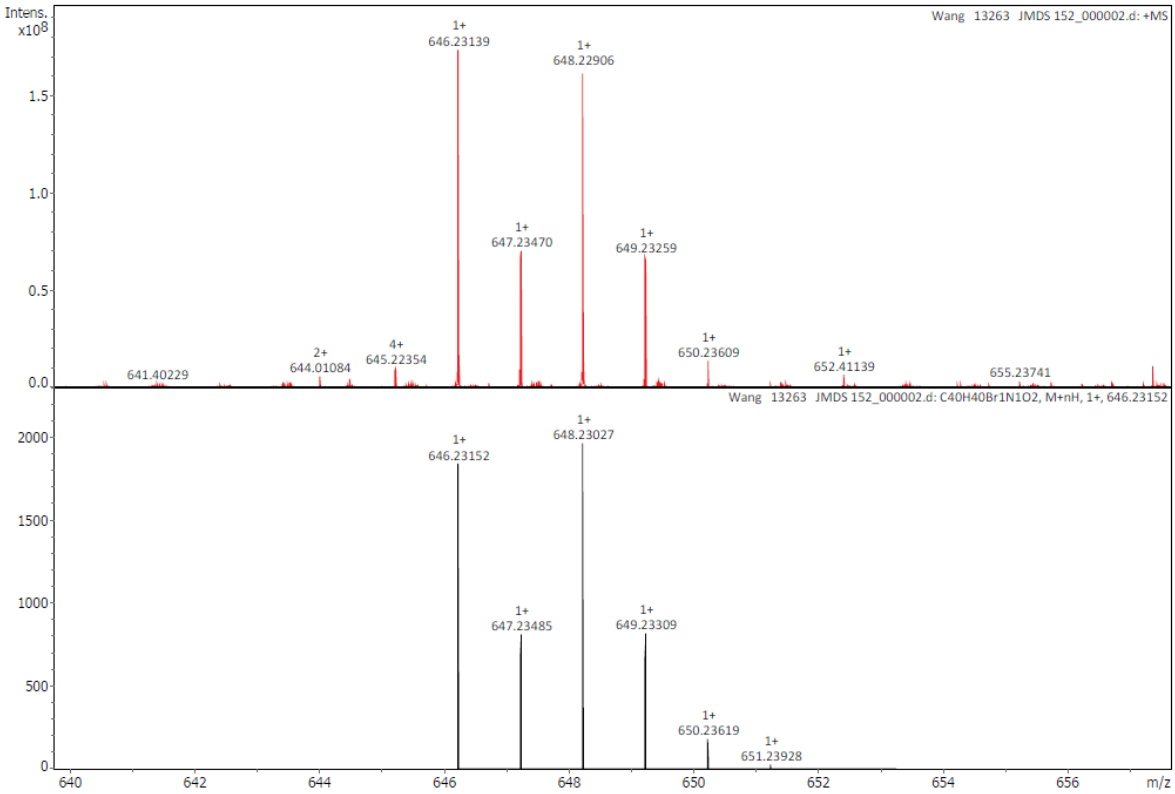

Figure A-7. HRMS of compound **4**.

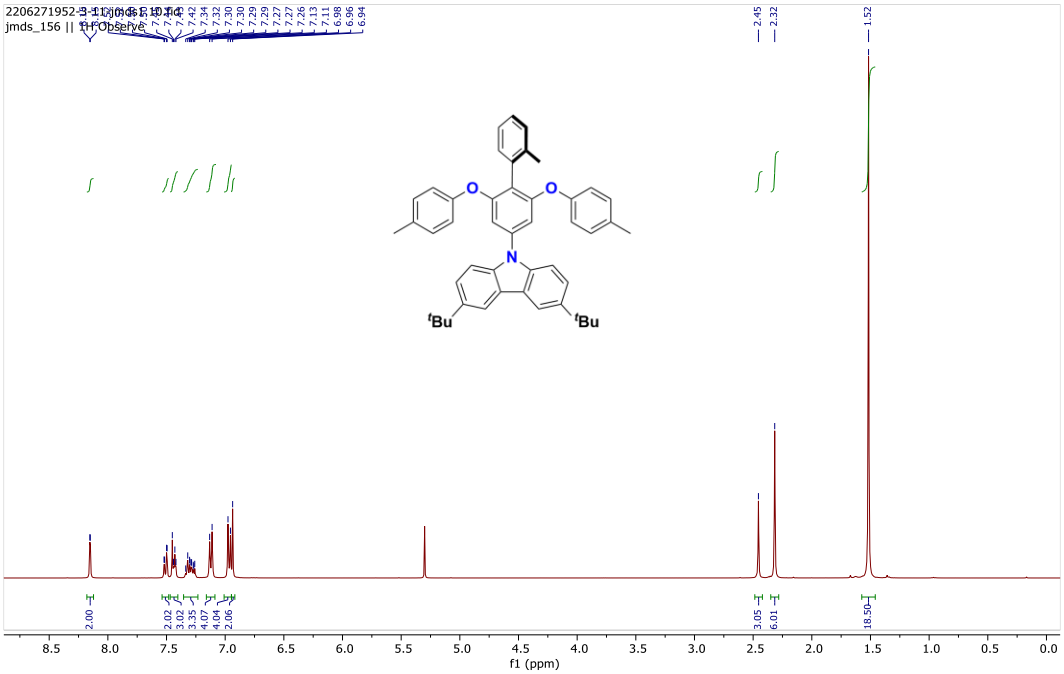

Figure A-8. ^{1}H NMR (400 MHz, $CDCl_3$) spectrum of **3**.

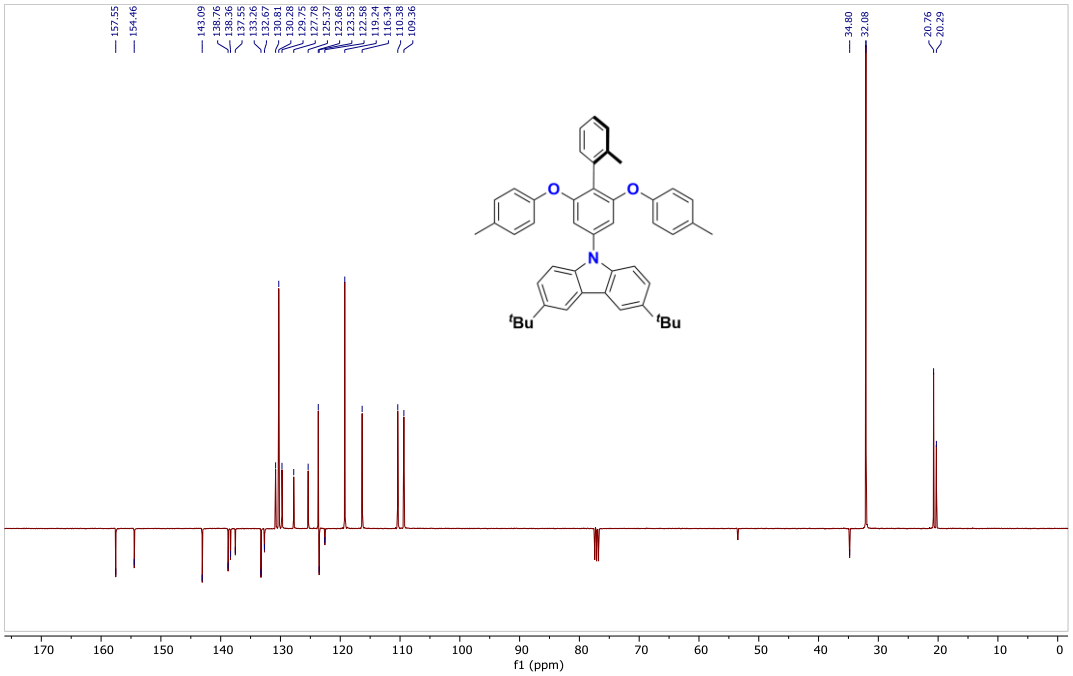

Figure A-9. DEPTq-135 (126 MHz, $CDCl_3$) spectrum of **5**.

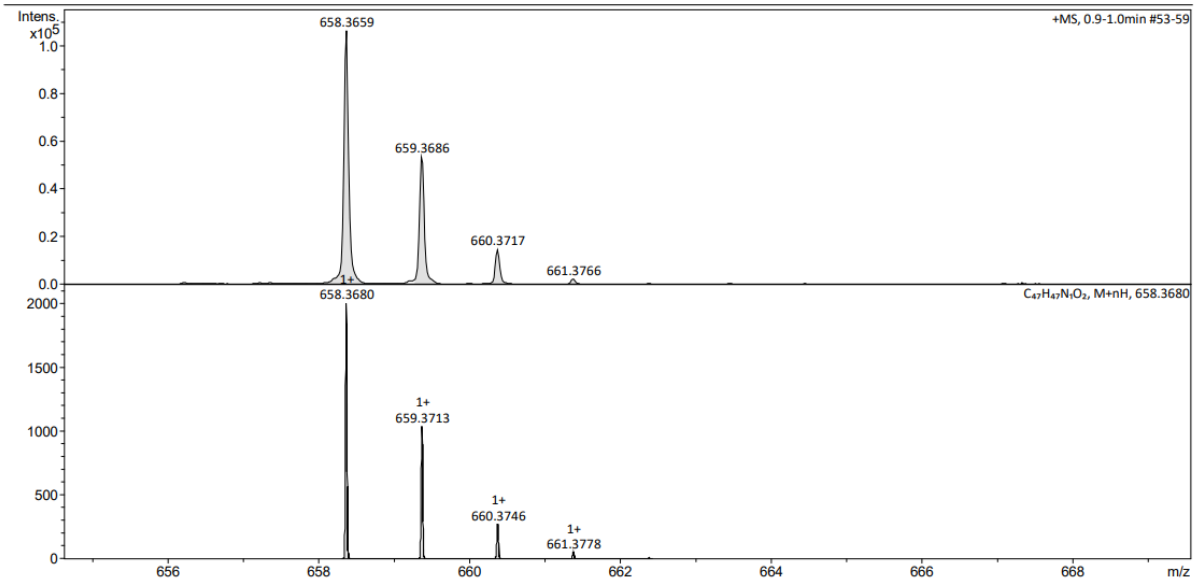

Figure A-10. HRMS of compound **5**.

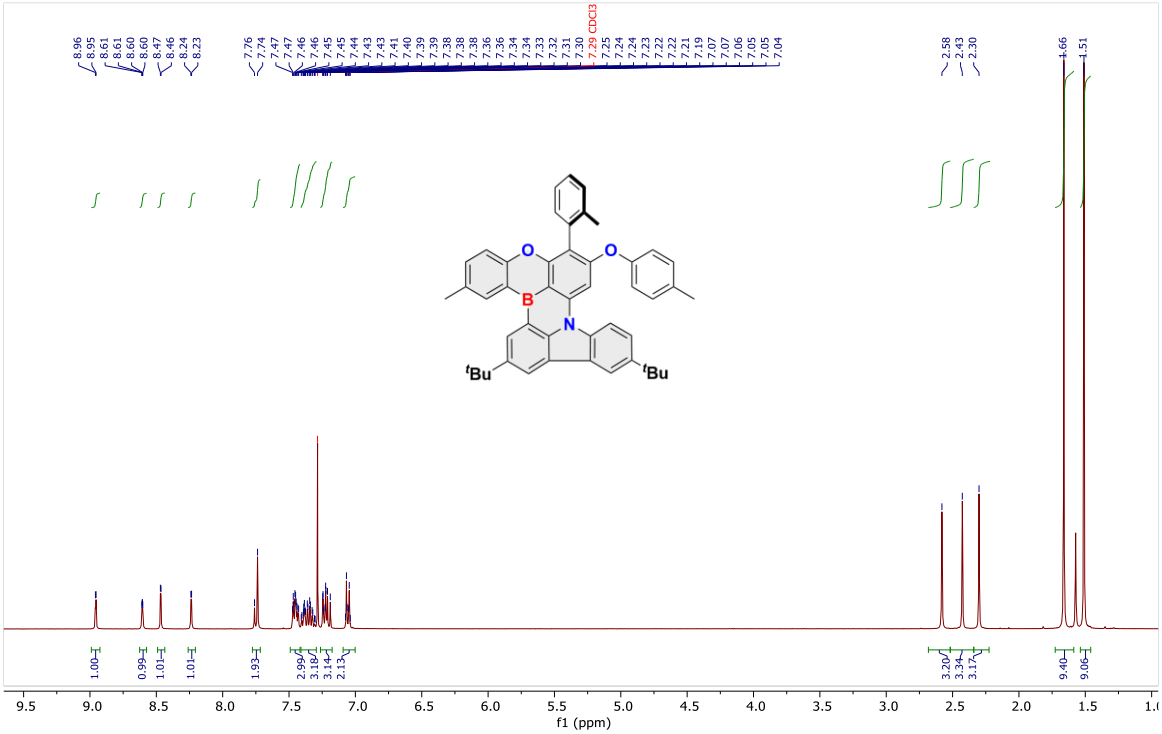

Figure A-11. ^{1}H NMR (400 MHz, $CDCl_3$) spectrum of **1B-CzCrs**.

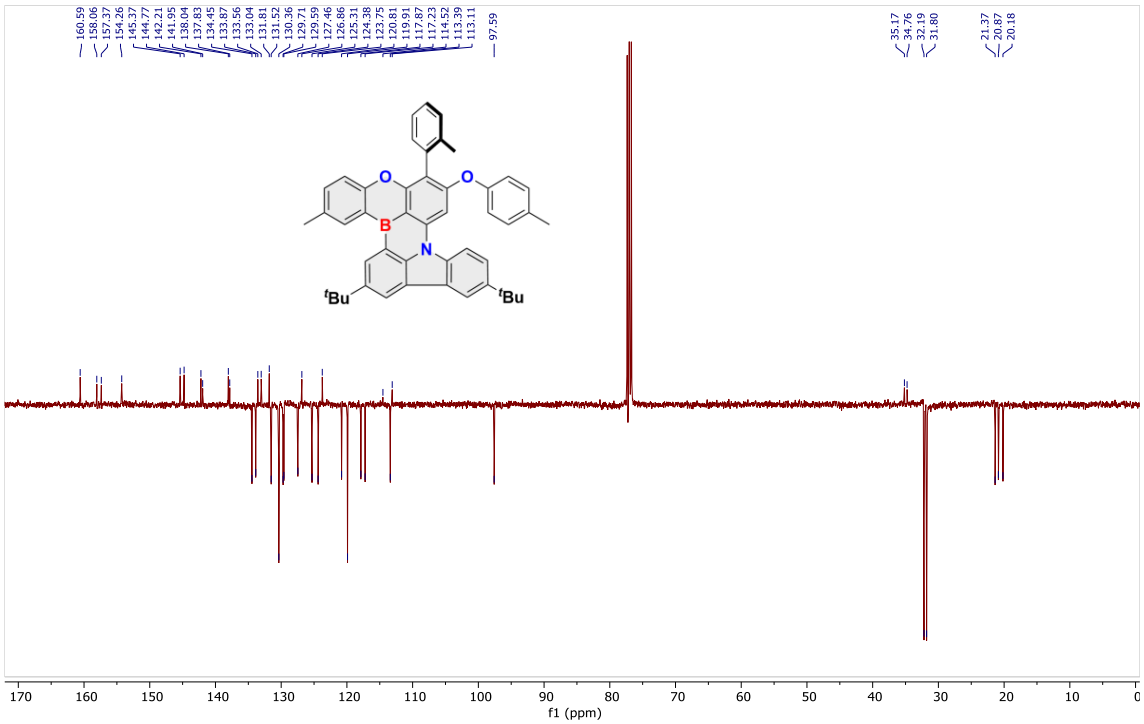

Figure A-12. DEPTq-135 (101 MHz, $CDCl_3$) spectrum of **1B-CzCrs**.

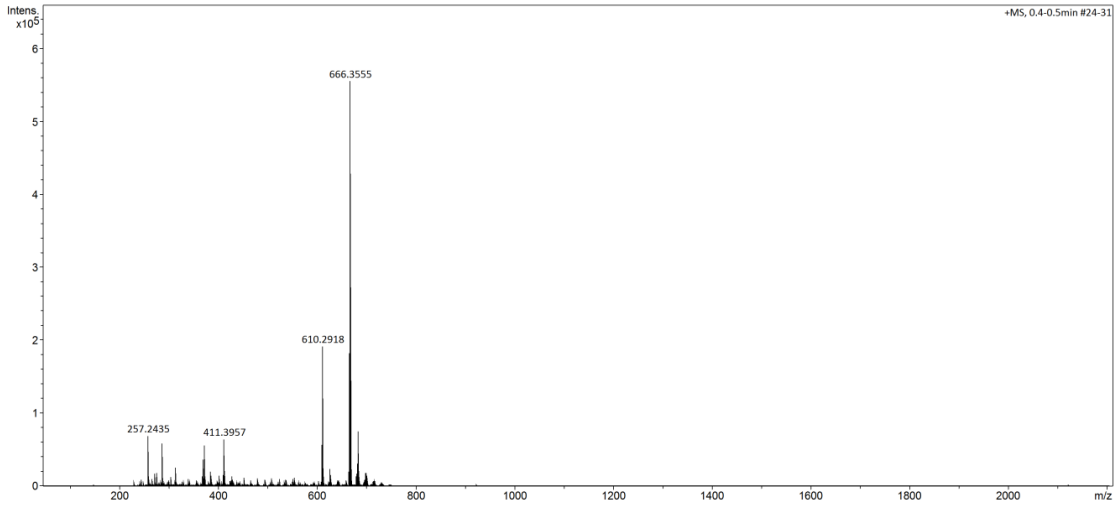

Figure A-13. HRMS of compound **1B-CzCrs**.

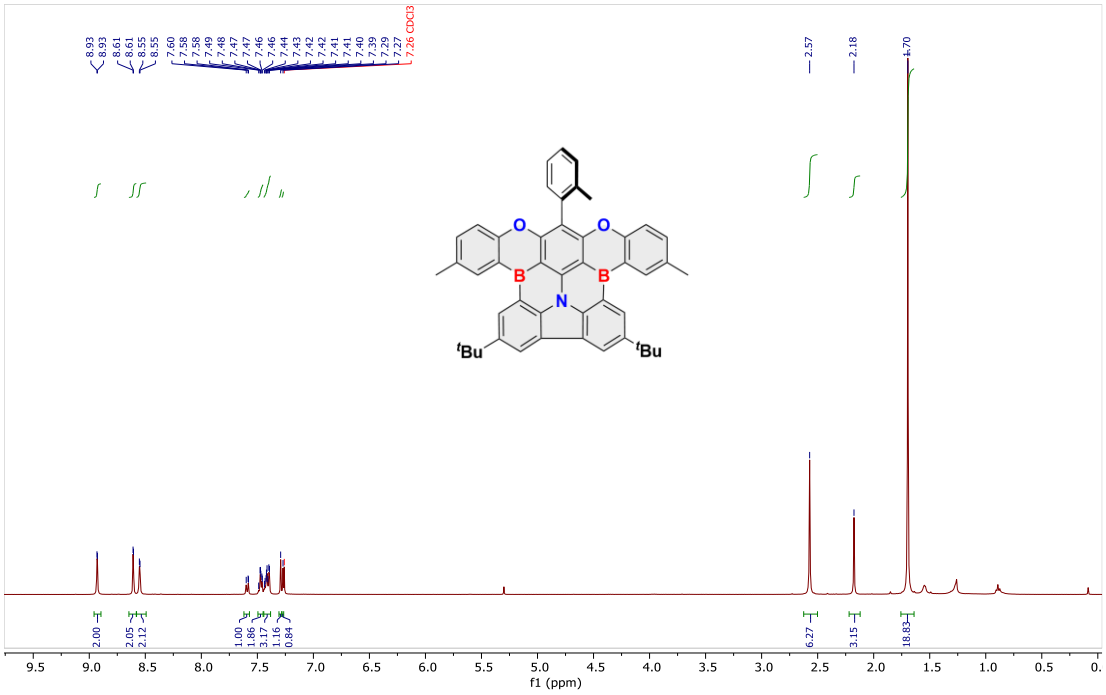

Figure A-14. ^{1}H NMR (400 MHz, $CDCl_3$) spectrum of **2B-CzCrs**.

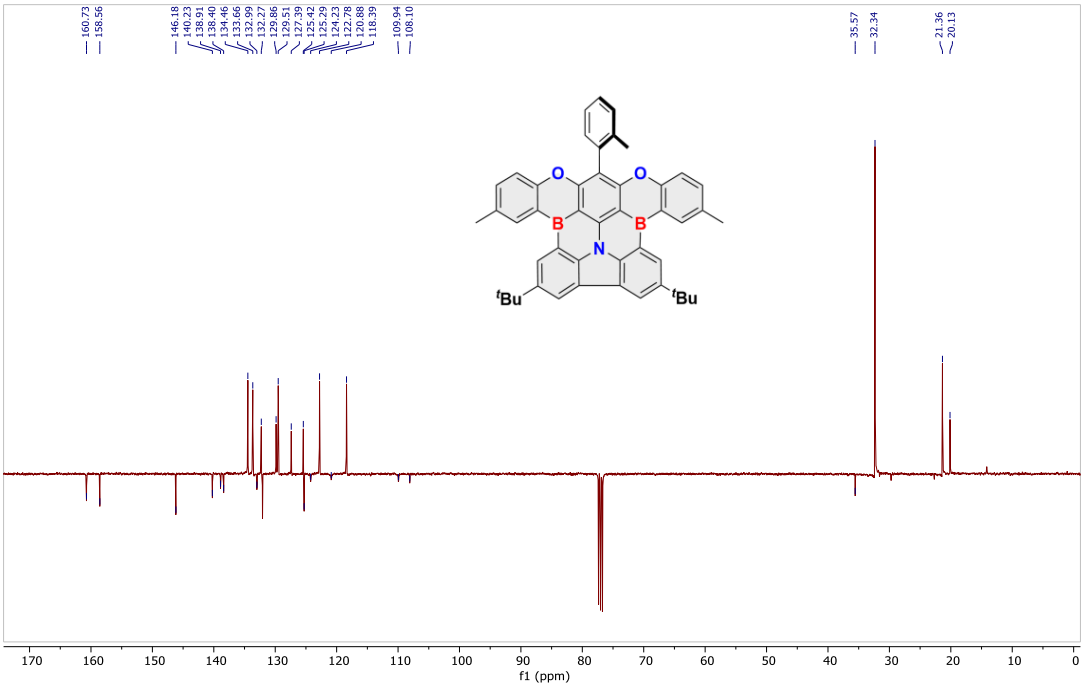

Figure A-15. DEPTq-135 (101 MHz, $CDCl_3$) spectrum of **2B-CzCrs**.

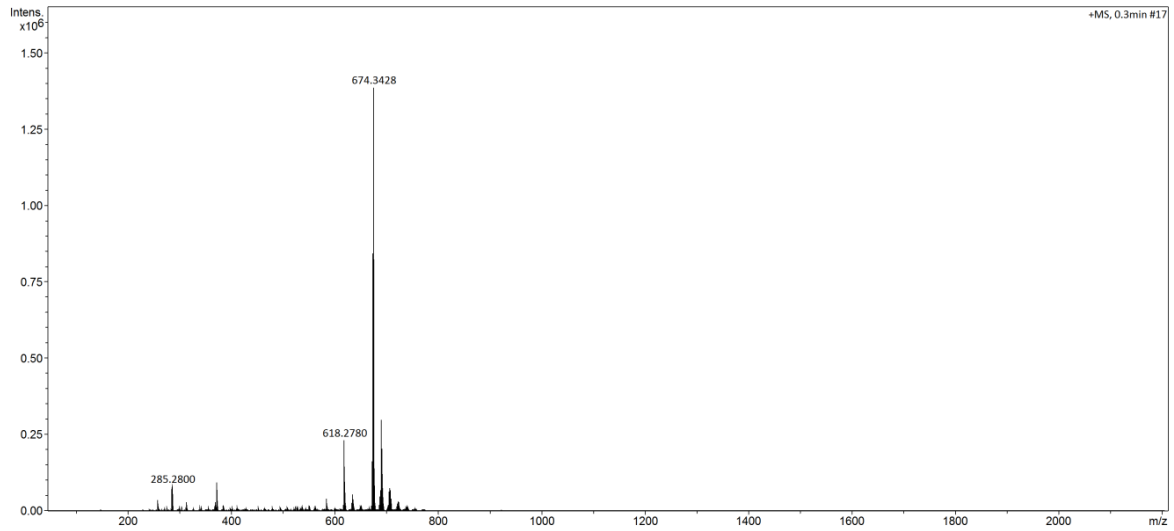

Figure A-16. HRMS of compound **2B-CzCrs**.

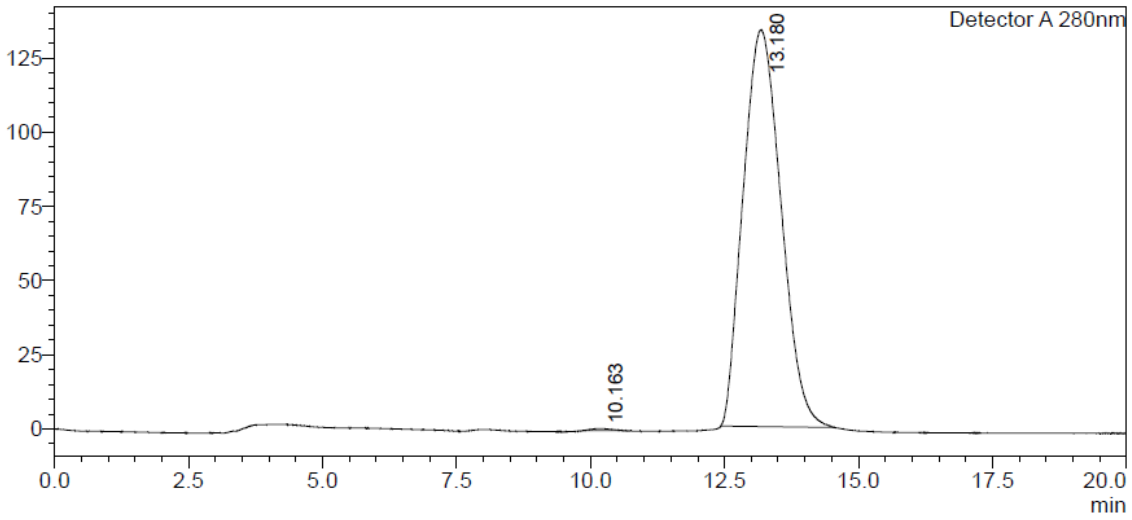

<Peak Table>

Detector A 280nm

Peak#	Ret. Time	Area	Height	Area%	Area/Height	Width at 5% Height
1	10.163	19109	650	0.289	29.389	0.829
2	13.180	6589289	133749	99.711	49.266	1.540
Total		6608399	134400	100.000		

Figure A-17. HPLC trace of **1B-CzCrs**.

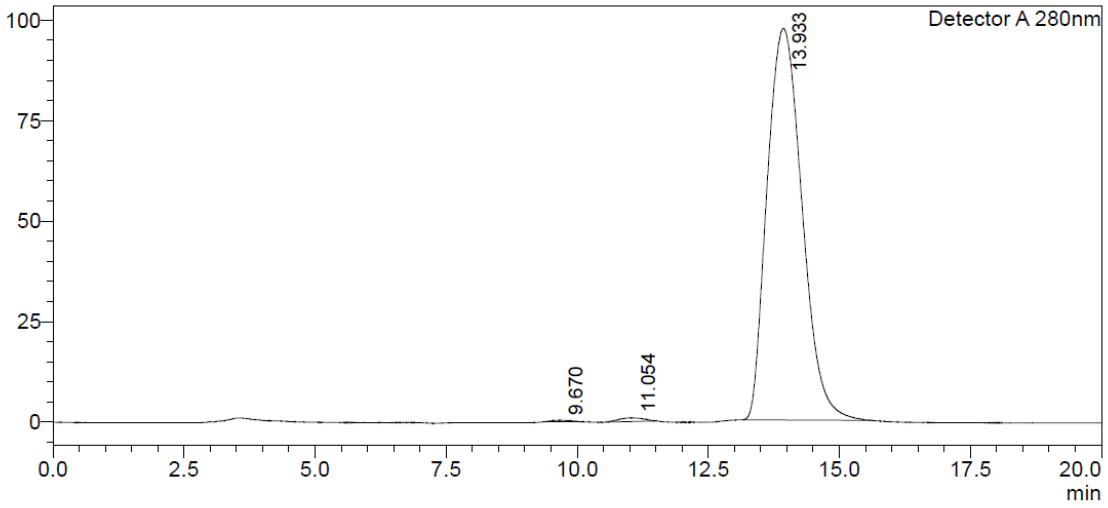

<Peak Table>

Detector A 280nm

Peak#	Ret. Time	Area	Height	Area%	Area/Height	Width at 5% Height
1	9.670	10229	391	0.225	26.153	0.711
2	11.054	29624	897	0.651	33.028	0.894
3	13.933	4512316	97386	99.125	46.334	1.461
Total		4552169	98674	100.000		

Figure A-18. HPLC trace of **2B-CzCRs**.

Electrochemistry

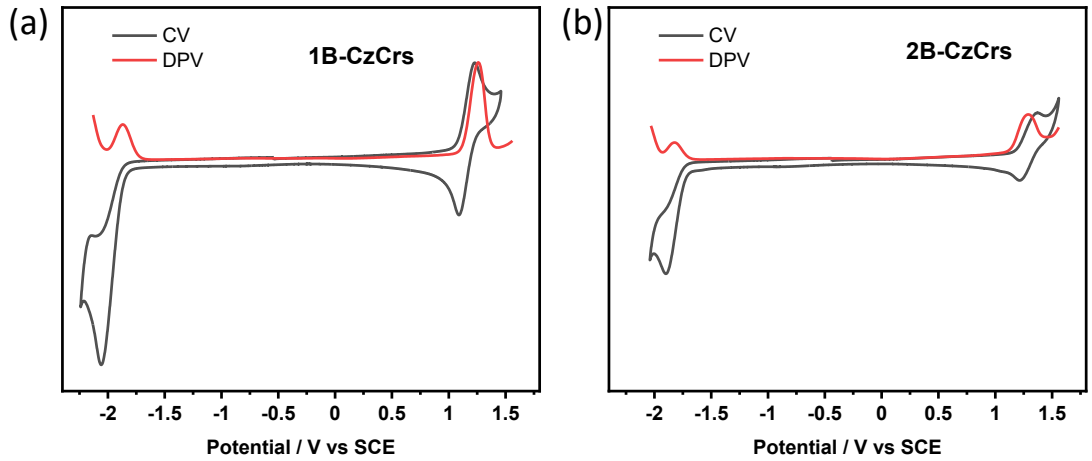

Figure A-19. Cyclic and differential pulse voltammograms (CV and DPV) of (a) **1B-CzCrs** and (b) **2B-CzCrs**, measured in degassed DCM with 0.1 M $^{n}Bu_4NPF_6$ as the supporting electrolyte and Fc/Fc^{+} as the external reference (0.46 V vs SCE); Scan rate = 100 mV s^{-1}.

Table A-1. Electrochemical data of **1B-** and **2B-CzCrs**.

Compound	E_{ox} [a] (V)	E_{red} [a] (V)	HOMO [b] (eV)	LUMO [b] (eV)	$\Delta E_{H\text{-}L}$ [c] (eV)
1B-CzCrs	0.80	−2.33	-5.60	−2.47	3.13
2B-CzCrs	0.82	−2.28	-5.62	−2.52	3.10

[a] Potential values obtained from the DPV peak values, measured in degassed dichloromethane with 0.1 M $^{n}Bu_4NPF_6$ as the supporting electrolyte and referenced with respect to SCE ($Fc/Fc^+ = 0.46$ eV). [b] HOMO and LUMO energy levels determined using the relation $E_{HOMO/LUMO} = -(E_{ox} / E_{red} + 4.6)$ eV (using Fc/Fc^+ as the external reference); [c] $\Delta E_{H\text{-}L} = \left| \text{HOMO} - \text{LUMO} \right|$ eV.

Appendix B

Synthesis and characterization of f-DOABNA

***f*-DOABNA** was synthesized in four easy to access chemical transformations. The outline of the synthesis procedure of ***f*-DOABNA** is illustrated in **Figure B-1. DOBNA** fragments were installed before the final borylation reaction to have multiple types of MR structures in the helicene core. This two-stage borylation approach ensures precise manipulation of borylation sites within the π-extended system, while also effectively reducing the overall molecular weight of the final product by eliminating the necessity for directing groups. Compound **1** was synthesized with an 81% yield utilizing 3,5-dichlorobromobenzene in a Buchwald-Hartwig cross-coupling reaction. Compound **2** was then formed by coupling two equivalents of 3,5-dimethylaniline with Compound **1** under Buchwald-Hartwig conditions, yielding 80%. The crucial intermediate, Compound **3**, was achieved with a 60% yield through coupling two equivalents of the DOBNA-Br fragment with Compound **2**. The desired blue emitter, f-DOABNA, was produced via electrophilic borylation of Compound 3 with BBr_3, yielding 40%.

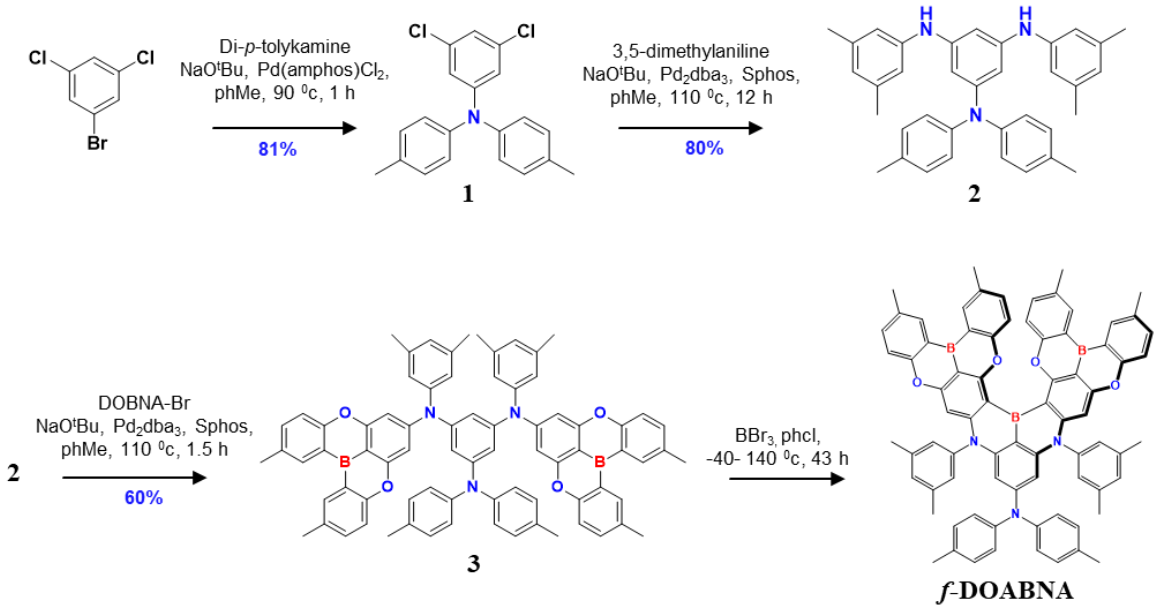

Figure B-1. Synthesis rout of ***f*-DOABNA**.

Chemical characterisation

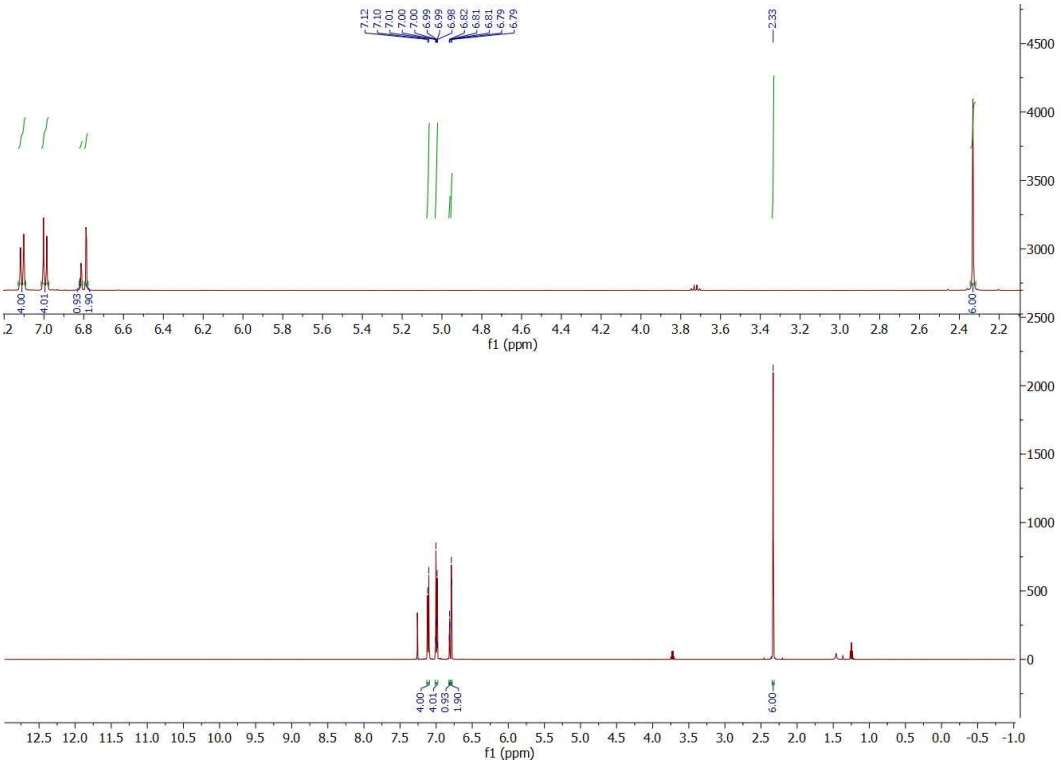

Figure B-1. ^{1}H NMR spectrum of **1** in $CDCl_3$.

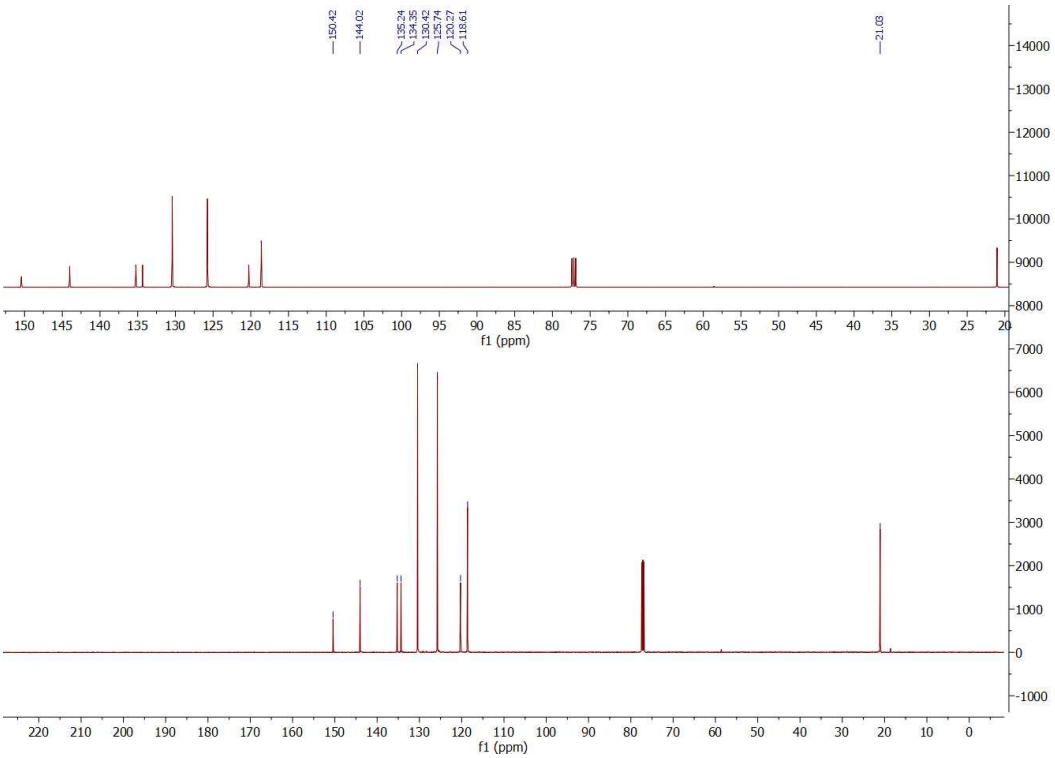

Figure B-2. ^{13}C NMR spectrum of **1** in $CDCl_3$.

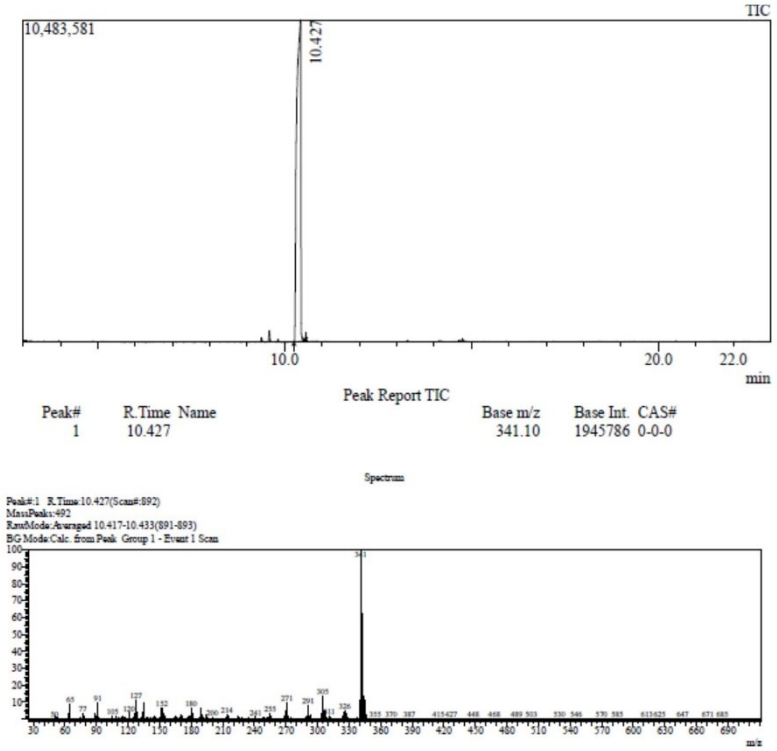

Figure B-3. GCMS of compound **1**.

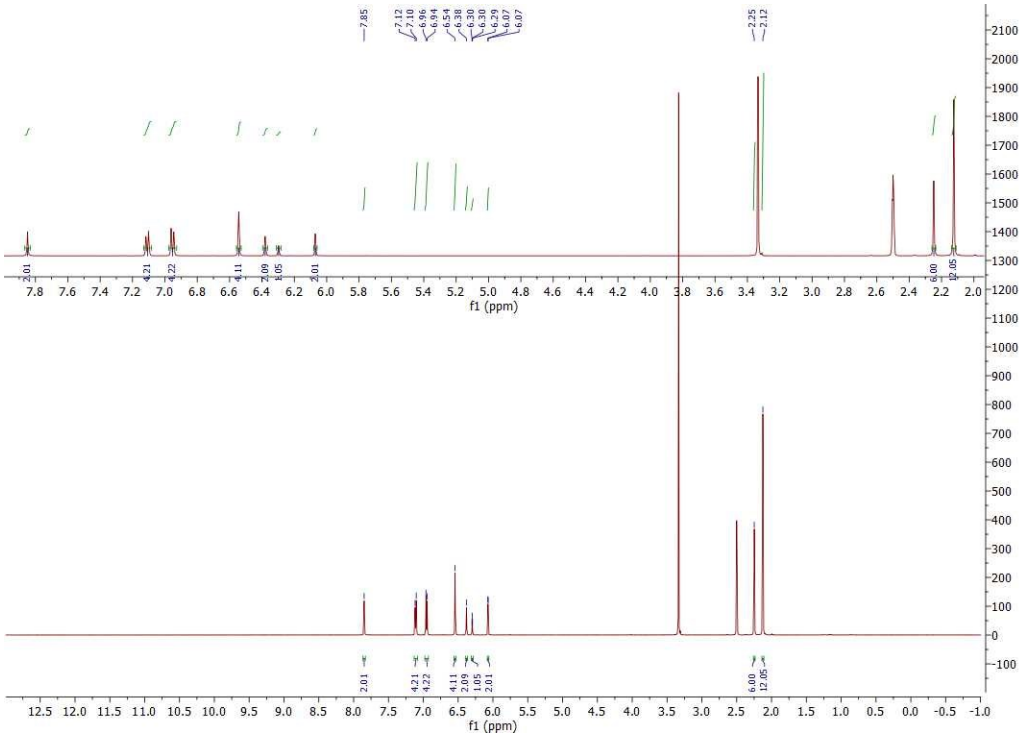

Figure B-4. ^{1}H NMR spectrum of **2** in d_6-DMSO.

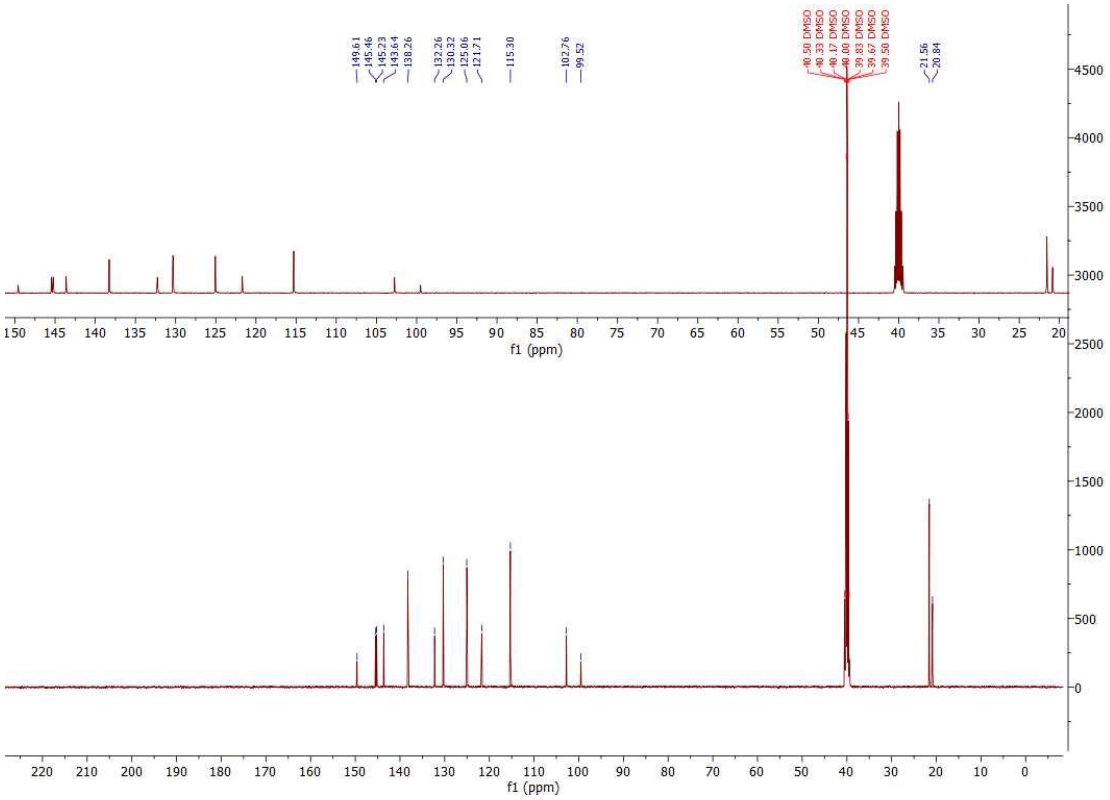

Figure B-5. ^{13}C NMR spectrum of **2** in d_6-DMSO.

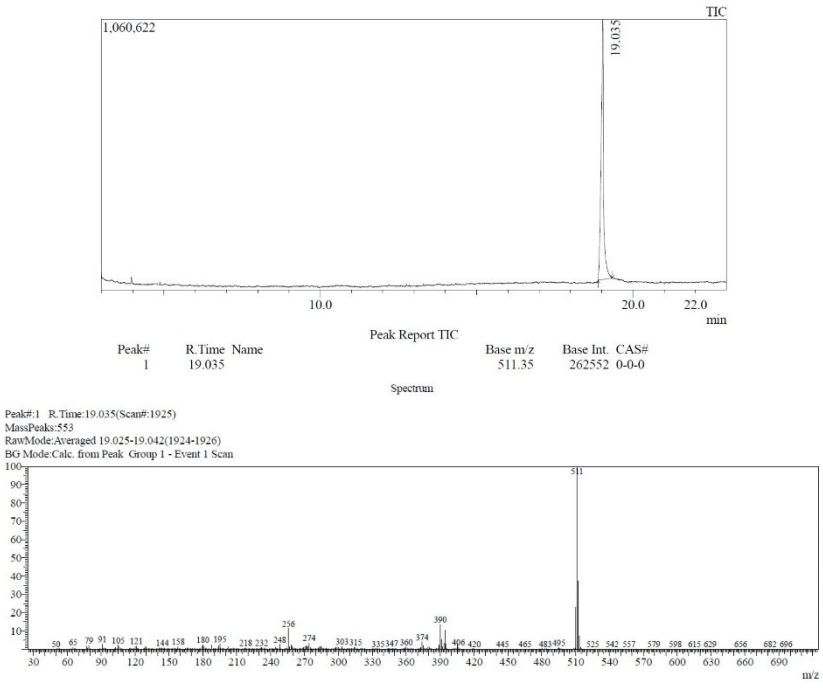

Figure B-6. GCMS of compound **2**.

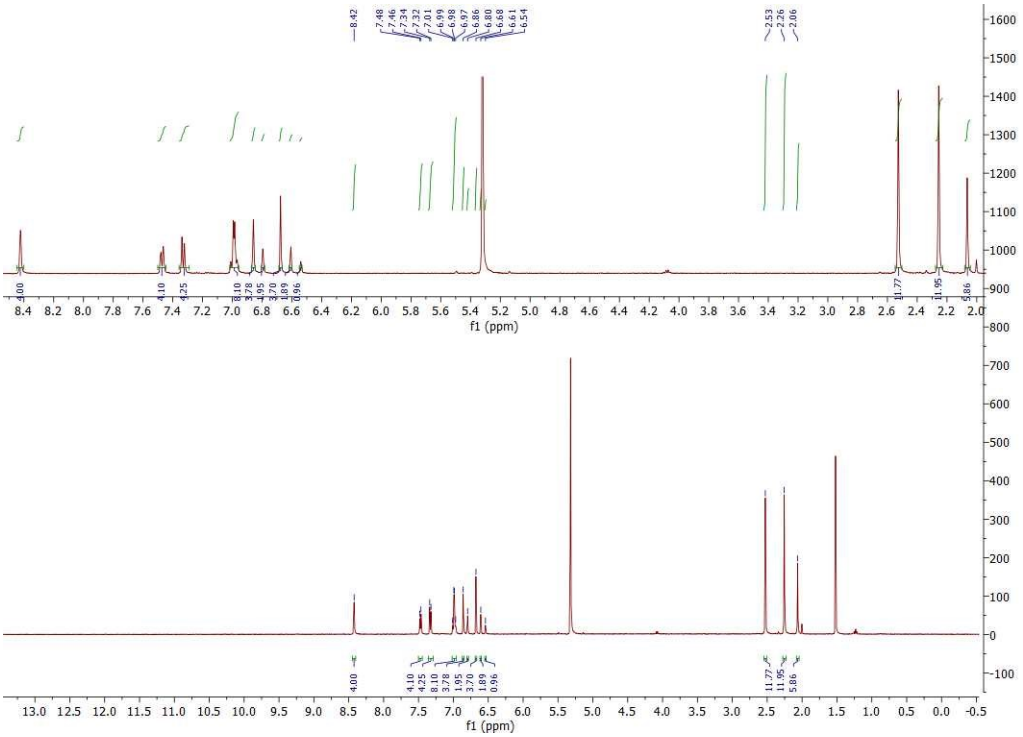

Figure B-7. ^{1}HNMR spectrum of **3** in CD_2Cl_2.

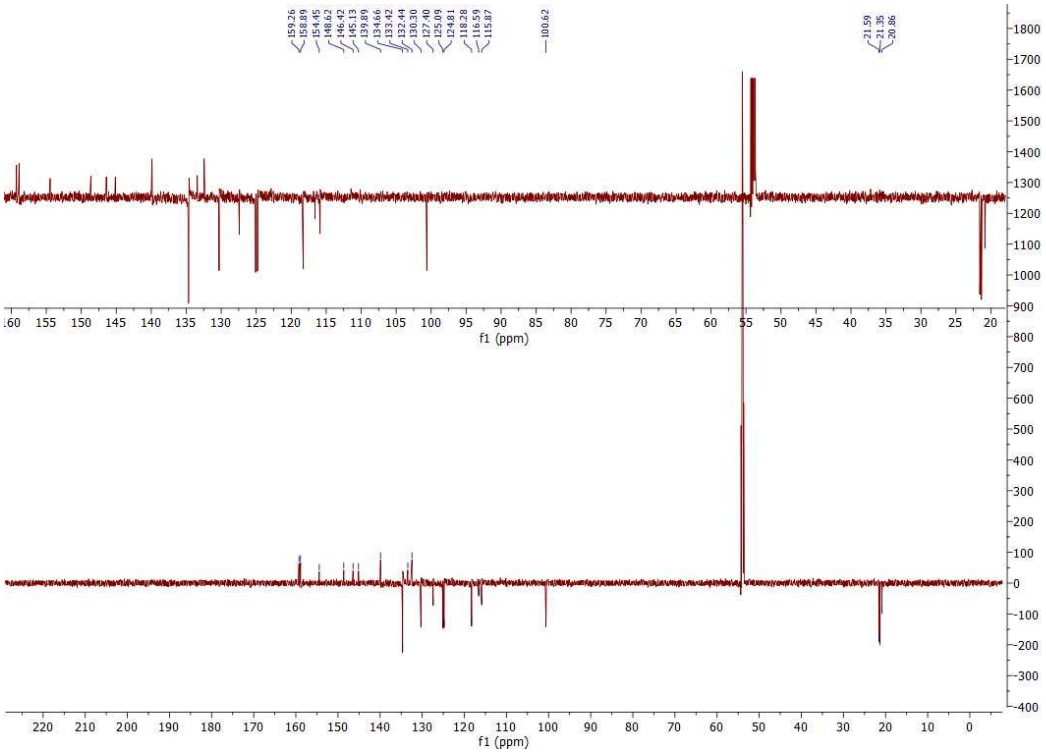

Figure B-8. ^{13}C DEPTq-135 NMR spectrum of compound **3** in CD_2Cl_2.

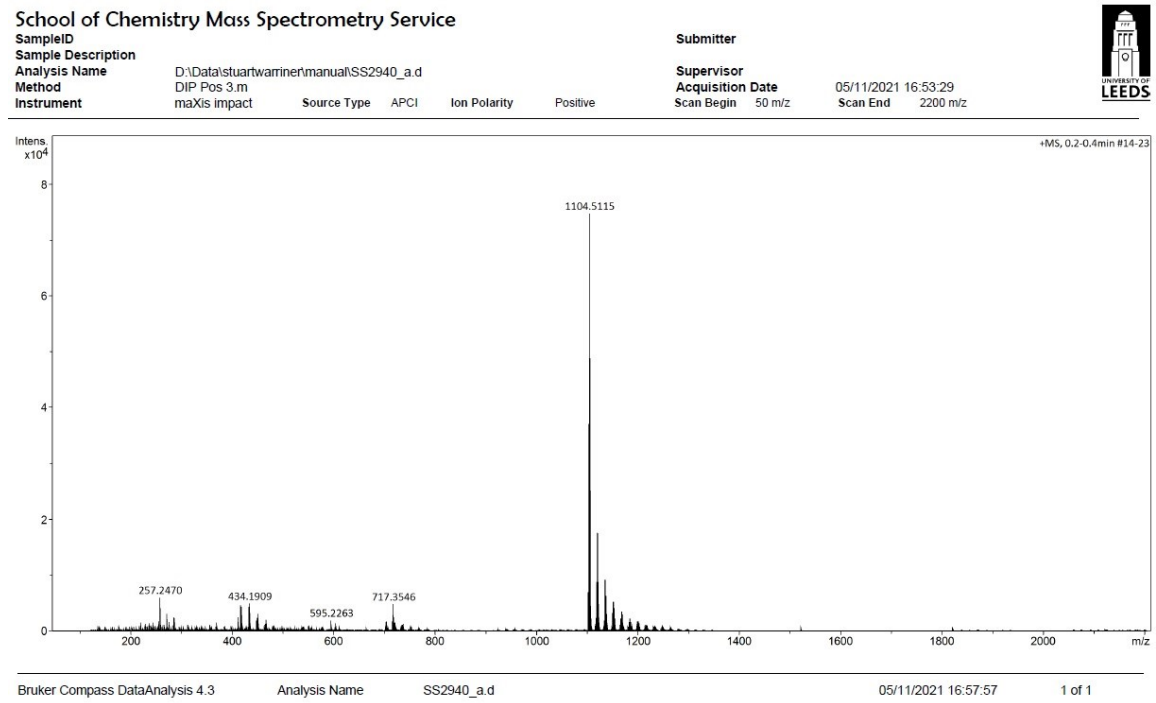

Figure B-9. High resolution mass spectrum of compound **3**.

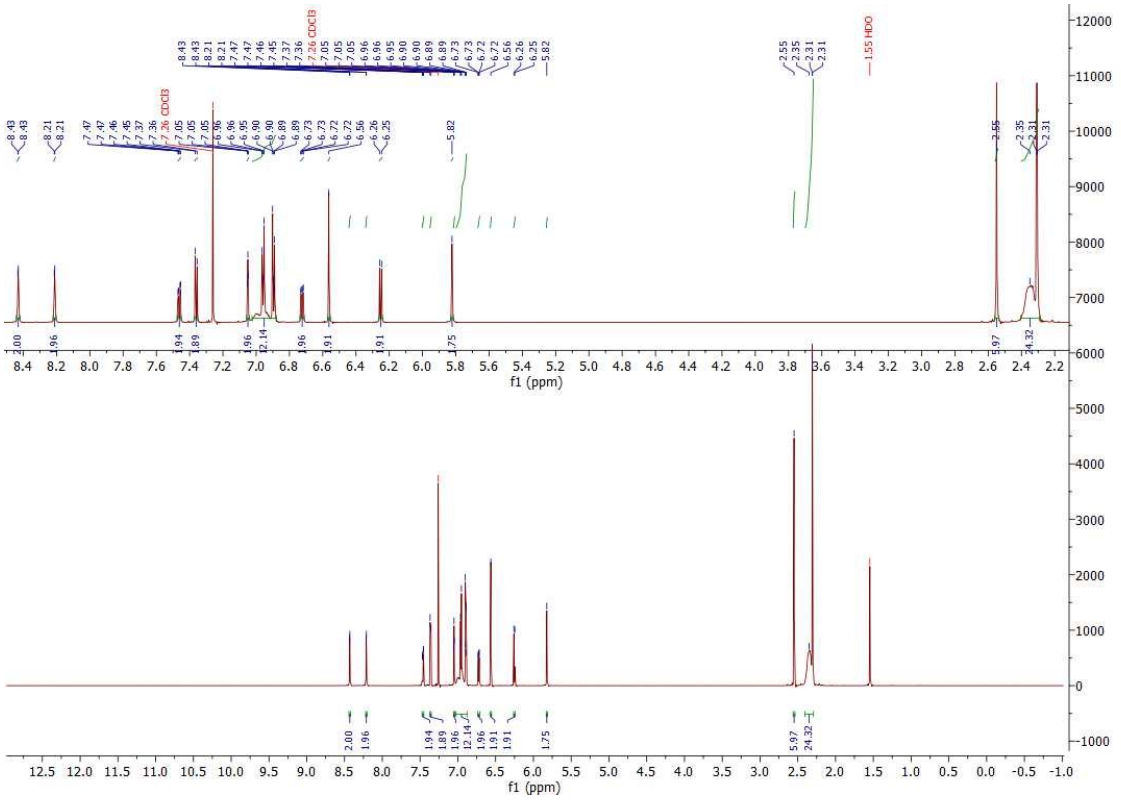

Figure B-10. ^{1}H NMR spectrum of ***f*-DOABNA** in $CDCl_3$.

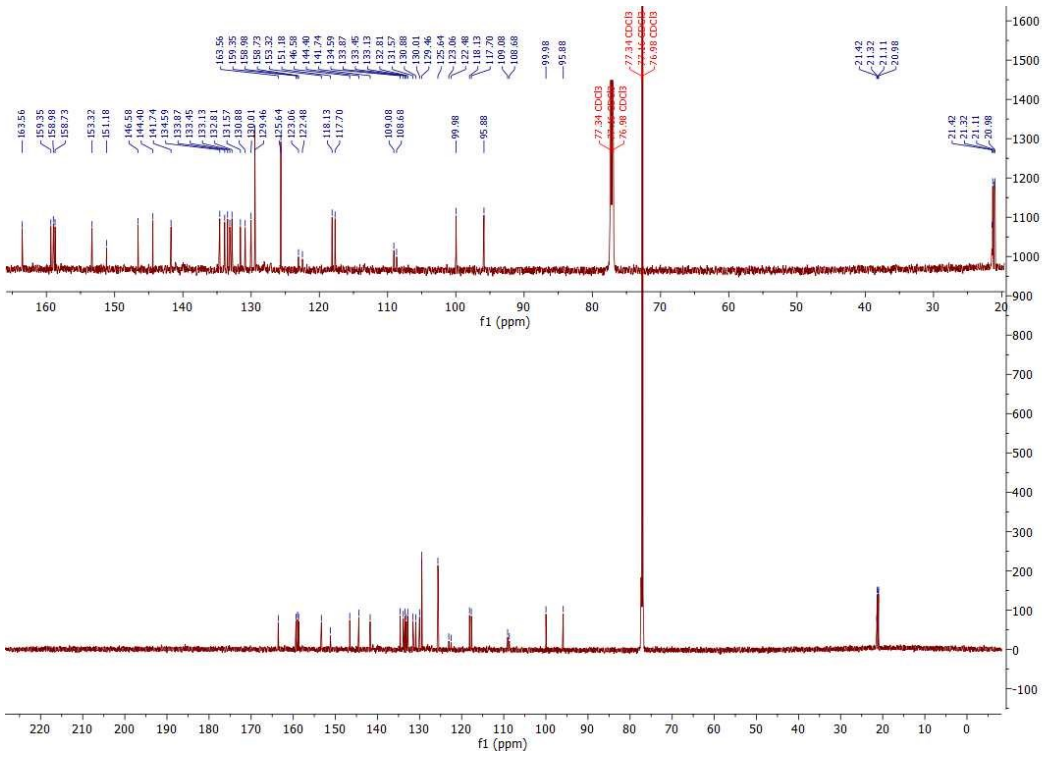

Figure B-11. ^{13}C NMR spectrum of ***f*-DOABNA** in $CDCl_3$.

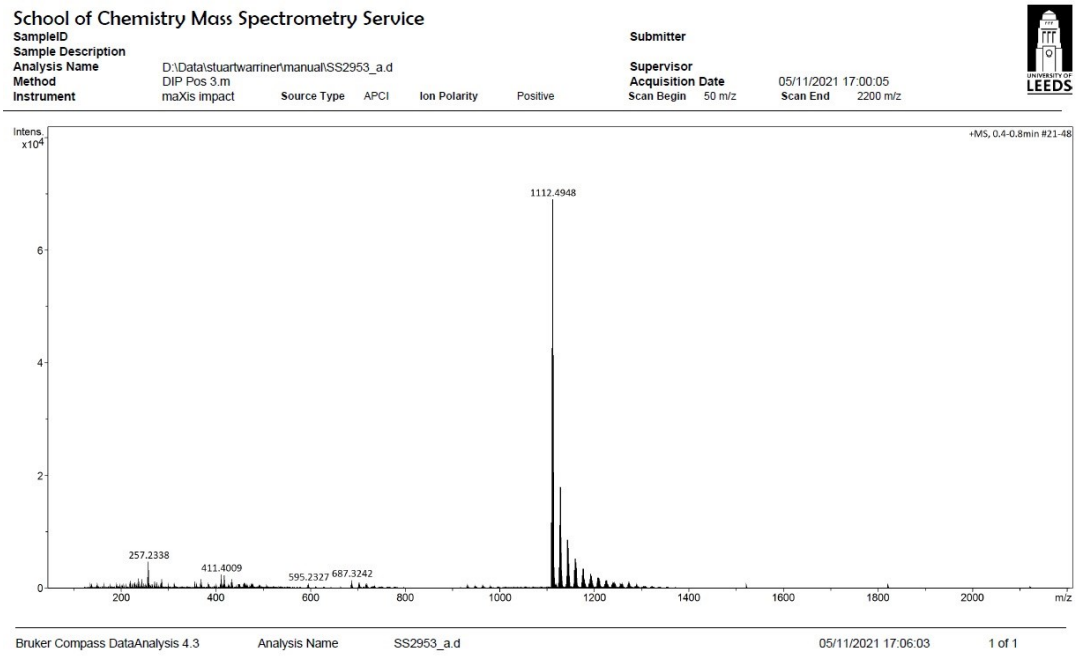

Figure B-12. High resolution mass spectrum of ***f*-DOABNA**.

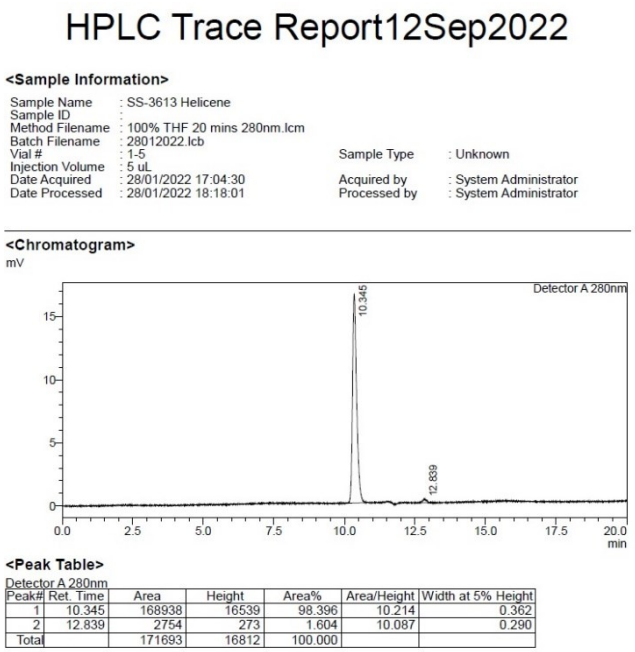

Figure B-13. High performance liquid chromatography gel permeation chromatography trace of ***f*-DOABNA**.

X-Ray structure data

a (Å)	8.69112(13)
b (Å)	18.1518(2)
c (Å)	22.8036(3)
α (°)	72.9316(12)
β (°)	79.7590(13)
γ (°)	87.1952(11)
Volume / $Å^3$	3384.22(8)
Space group	P -1
Hall group	-P 1
Moiety formula	$C_{85}H_{81}B_3N_3O_4$
Mr	1241.02
Dx,g cm^{-3}	1.218
Z	2
Mu (mm^{-1})	0.565
F000	1318.0

h,k,lmax	10,21,27
Nref	12063
Tmin,Tmax	0.756,0.983

Electrochemistry

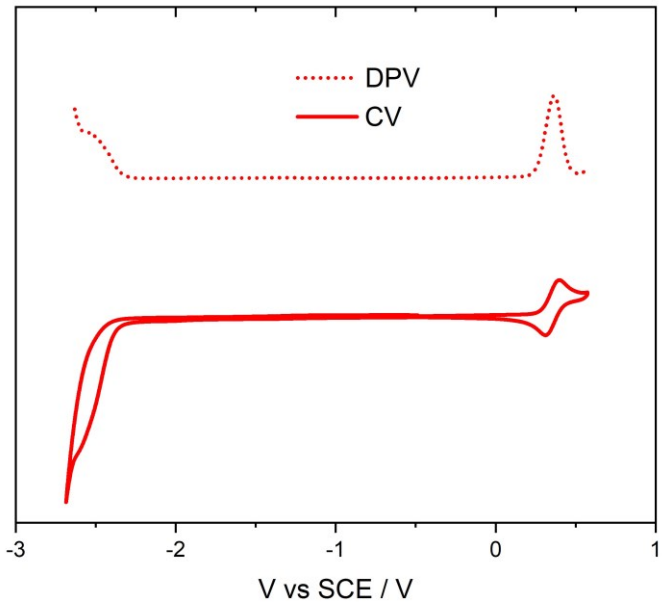

Figure B-14. Cyclic (CV) and differential pulse (DPV) voltammograms measured in degassed DCM with 0.1 M $^{n}Bu_4NPF_6$ as the supporting electrolyte and Fc/Fc^{+} as the external reference (0.46 V vs SCE). Scan rate = 100 mV s^{-1} of ***f*-DOABNA**.

Table B-1. Electrochemical properties of ***f*-DOABNA**.

Compound	E_{ox} [a] **(V)**	E_{red}[a] **(V)**	**HOMO**[b] **(eV)**	**LUMO**[b] **(eV)**	$\Delta E_{H\text{-}L}$[c] **(eV)**
***f*-DOABNA**	0.37	−2.51	−5.17	−2.29	2.88

[a]In degassed DCM with 0.1 M $^{n}Bu_4NPF_6$ as the supporting electrolyte and Fc/Fc^{+} as the external reference (0.46 V vs. SCE). [b]The HOMO and LUMO energies were determined using the relation $E_{HOMO/LUMO} = -(E_{ox} / E_{red} + 4.6)$ eV, where E_{ox} and E_{red} are the anodic and cathodic peak potentials, respectively calculated from DPV related to Fc/Fc^{+}. [c]$\Delta E_{H\text{-}L} = |$HOMO – LUMO$|$ eV.